Investigation of Thermal and Electrical characteristics of crystalline silicon Photovoltaic modules under varying operational conditions

M. Vumbugwa

2022

Investigation of Thermal and Electrical characteristics of crystalline silicon Photovoltaic modules under varying operational conditions

By

Monphias Vumbugwa

Submitted in fulfilment of the requirements for the degree of

Doctor of Philosophy (Physics)

to be awarded at the Nelson Mandela University

December 2022

Supervisor: Prof E. E. van Dyk

Co-Supervisor: Dr F. J. Vorster

Co-Supervisor: Dr J. L. Crozier McCleland

Declaration

I, Monphias Vumbugwa 218207115, hereby declare that the treatise/ dissertation/ thesis for Doctor of Philosophy (Physics) to be awarded is my own work and that it has not previously been submitted for assessment or completion of any postgraduate qualification to another University or for another qualification.

Monphias Vumbugwa

Official use:

In accordance with Rule G5.11.4, I hereby declare that the above-mentioned treatise/ dissertation/ thesis is my own work and that it has not previously been submitted for assessment to another University or for another qualification. However, material from publications by the student may be embodied in a treatise/dissertation/ thesis.

NELSON MANDELA
UNIVERSITY

PERMISSION TO SUBMIT FINAL COPIES

OF TREATISE/DISSERTATION/THESIS TO THE EXAMINATION OFFICE

FACULTY: SCIENCE

DEPARTMENT: PHYSICS

I, van Dyk E. E. and Vorster F. J. and Crozier McCleland J. L. the supervisor and co-supervisors respectively for Vumbugwa M. 218207115 a candidate for the Doctor of Philosophy (Physics) with a treatise/dissertation/thesis entitled: Investigation of Thermal and Electrical characteristics of crystalline silicon Photovoltaic modules under varying operational conditions.

It is hereby certified that the proposed amendments to the treatise/dissertation/thesis have been effected and that **permission is granted to the candidate to submit** the final bound copies of his/her treatise/dissertation/thesis to the examination office.

E.E. van Dyk	12 october 2022
SUPERVISOR	**DATE**
(signature)	12 October 2022
CO-SUPERVISOR	**DATE**
Vorster	12 October 2022
CO-SUPERVISOR	**DATE**

iii

Dedicated to Laphine and Lowell,

In memory of Finiyasi and Laina.

Acknowledgements

My sincere gratitude to:

Abstract

Solar energy has become an attractive and environmentally mindful method in electrical power generation as it contributes significantly to meeting the high demand for the power needed for socio and economic developments. The rise in deployment of Photovoltaic (PV) facilities with large capacity creates the need for accurate and reliable PV inspection techniques for optimum performance, the longevity of PV modules and quick return on PV investment. The performance of PV modules in the field is often monitored through several inspection methods that require a rapid throughput such as Thermal Infrared (TIR) imaging and current-voltage (I-V) measurements. Unmanned Aerial Vehicle (UAV) based TIR imaging is widely applied in large PV plants since it is cost-effective and is usually conducted in-situ while the plant is operating at irradiance levels above 600 $W.m^{-2}$. One of the outcomes of the interpretations of TIR images is an attempt to quantify the energy loss in PV plants associated with the abnormal thermal signatures identified on TIR images. No standard procedure has yet outlined the quantification of energy loss related to TIR images of underperforming modules since the interpretation of TIR images remains a challenge.

PV modules operate under dynamic operating conditions which can influence the results and interpretation of thermal and electrical characterisation measurements. Dynamic operation conditions refer to any disorders in the operation of the modules and cells which cause a change in the current and voltage characteristics of the PV source. These dynamic operation conditions include; changes in load conditions, irradiance, soiling and shading levels. The tests were done under steady state conditions. Although measurements are generally done while the operating conditions are as steady as possible, some changes in conditions have a profound effect on thermal and electrical measurements. In this study, these effects and some of the changes in conditions that cause them were studied.

Thermal and electrical measurements on PV modules and strings offer a guide to the state of a PV plant and its ability to produce electrical power. One of the most important issues that are revealed in these measurements is the level of mismatch between series-connected cells and modules. Current mismatch shows up as abnormally hot cells in TIR images and anomalies such as bumps in the shape of the I-V curves. Current mismatch can generally be classified as belonging to two types; i) Inherent mismatch as a result of cell manufacturing faults, failure

in the field and incorrect batching or ii) external mismatch caused by environmental conditions such as shading or soiling. Any factor that can change the level of current mismatch between cells will cause a change in the TIR image and the I-V curve of a module, thus complicating the interpretation of these measurements. The effect that a change in shading and soiling have on thermal and electrical measurements as well as the effect that a change in the current and voltage operating point of cells and modules have on thermal and electrical measurements have, were studied. The complexity of the interpretation of the results due to these dynamic operating conditions was investigated and discussed in detail.

To understand the behaviour of thermal and I-V characteristics of the crystalline silicon PV modules, TIR images and current and voltage measurements of the modules were recorded under different operational conditions which included; varying irradiance, output power, shading and load conditions. Variable partial shading was used to analyse the electrical and thermal behaviour of operational crystalline silicon (c-Si) modules, substrings and individual cells by recording Thermal Infrared (TIR) images concurrently with electrical measurements of individual cells when shading levels between 0 and 100% were applied on one cell. The study investigated the relative changes in each of the individual cells' operational cell voltage and the current of the substring containing the shaded cell. These changes are significant and gave additional insights into the loss of energy production of a module containing a shaded cell.

The shading level that causes the shaded cell to change from a positive voltage (generating power) to a negative voltage (dissipating power) depends on the module's operational conditions such as irradiance level and load conditions. Significant cell mismatch, that causes abnormal thermal signatures, occurs when the module's operational point is on the horizontal section of the I-V curve, and close to I_{SC} and can be due to operational conditions such as low irradiance, < 400 W.m^{-2}, and small fixed load (resistance) conditions. When the operational point of the module is on the vertical section of the I-V curve, and close to V_{OC}, the mismatch will be minimal to cause abnormal thermal signature and the bad cells operate and appear as good cells on TIR images. When a PV module underperforms, it is beneficial for the operational point to be higher than V_{MP}, since the bad cells will not become abnormally hot to cause detrimental effects such as module back sheet damage, cracks, risk of fire and increased module degradation rate.

The dynamics of the abnormal thermal signatures under different operational conditions such as changing load, irradiance and shading levels, can cause misinterpretation of the results of TIR imaging inspections. This occurs when cells that would normally show up as hot cells become masked by the thermal signatures of shaded cells. TIR imaging should therefore be carried out on unsoiled and unshaded modules. By incorporating additional testing methods such as visual inspections, I-V measurements and Electroluminescence (EL) imaging, a more informed interpretation of the cause of the abnormal hot cells in the TIR image can be made.

In addition to the standard guidelines for capturing TIR images, such as under steady environmental conditions, clear sky with an irradiance of above 600 $W.m^{-2}$, angle of capture, emissivity, etc., it is beneficial to carry out TIR imaging when the operational point of the modules is less than maximum power point (MPP) and closer to I_{SC}. That is when the modules deliver a large current and a significant current mismatch can occur such that most cell anomalies can easily present themselves as abnormal thermal signatures. This option may not be practically achievable since most module strings operate close to their maximum power points. However, it must be recognised that as a result of module mismatch, not all series-connected modules will operate at their maximum power points. Some modules and cells may operate at voltage points lower than their V_{MPP} and thus enhance the observation of mismatched cells in TIR imaging. This study recommends the design of inverters to incorporate a function which allows the operating point to be changed from the maximum power point in order to identify intrinsic abnormal thermal signatures on clean modules. Additionally, when PV modules are mismatched, the overheating of cells may be minimised by operating closer to V_{OC}. Inevitably, this leads to a reduction in power. In this way, the reliability and performance of crystalline PV modules operating in PV plants can be improved.

Keywords: Crystalline silicon modules, operational conditions, thermal signature

Table of Contents

Appendix A: Research outputs associated with this work

List of Figures

List of Tables

Chapter 1

Introduction and objectives of the study

1.1 Photovoltaics status

Electrical energy is key to socio-economic and environmental development; hence distribution of renewable energy technologies is inevitable to meet the high demand for energy. Solar energy is the largest renewable energy source and the global investment in solar energy systems, amounting to USD 148.6 billion in 2020 [1], contributes to the expansion of this energy technology. It is now amongst the most viable and sustainable electrical power generators and is destined to be a widely used global electrical energy source due to, the high demand for electrical energy, the depletion rate of traditional fossil fuel reserves and the international drive towards clean power production.

Technological advances and decreasing capital costs have also contributed to the growth of photovoltaic (PV) systems from small applications to large commercial scale PV plants which can be stand-alone, mini-grids, grid-tied or hybrid systems. To ensure a low levelised cost of electricity (LCOE), PV systems need to operate reliably and efficiently over their expected lifespan. This can only be achieved if a system is regularly monitored to identify performance degrading defects as early as possible. Thermal infrared (TIR) imaging is one such technique that is commonly used. One of the focus points of this study is on the dynamic nature and correct interpretation of TIR imaging for crystalline silicon PV devices. The LCOE of the utility-scale solar PV has reduced in recent years [2][3][4], which is the key that enhances the pace of growth of the PV technology. The global overall growth in PV deployment for residential and commercial applications is shown in Figure 1.1 and the world's total capacity stands at approximately 710 gigawatts (GW) as of 2020. There are still challenges in several countries, mainly in Africa, for solar PV to become a major supply of power due to policy and regulatory instability and financial constraints [5][6].
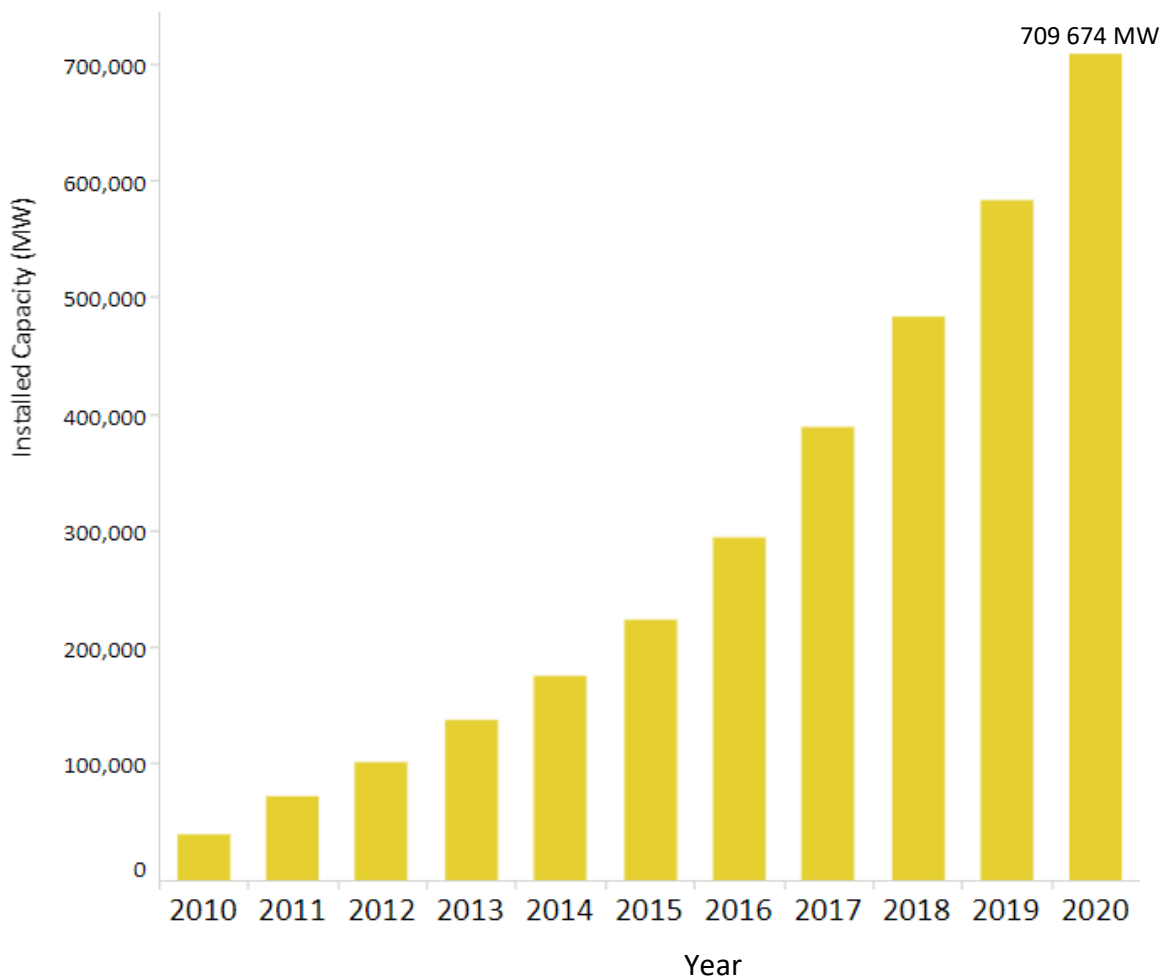
Figure 1.1: Global capacity of solar PV for the years 2009-2019 [5].

Africa has a good climate and potential for solar energy as indicated on the map in Figure 1.2, but several African countries are experiencing electrical energy rationing known as load shedding and not fully utilising the natural solar resource. Countries such as Egypt, South Africa, Kenya, Namibia and Ghana took the lead in PV plants installations to mitigate electrical power challenges. The do-it-yourself (DIY) approach is still carried out, in countries like Zimbabwe [7], by installing small household PV generators to bridge the gap in energy needs despite that the country had the capability (Solarcomm) in 1988 to assemble solar modules from imported PV cells [8]. The country's advancement in inviting investors into the energy sector and the call for tenders to grant power purchase agreements (PPA) will decrease reliance on energy imports and accelerate the nation's economic development.

In terms of operational solar systems, South Africa is the largest in Africa having several PV plants with a total installed PV capacity of 2.5 GW, according to the International Renewable Energy Agency (IRENA) [6]. The growth in PV system deployment and investment

in roof and ground-mounted, stand-alone and grid-tied PV plants is mainly due to the launch and support of the Renewable Energy Independent Power Producer Procurement Programme (REIPPPP) by the government of South Africa [6][9][10]. This rapid growth shows that the PV industry is becoming highly competitive in the overall energy mix in South Africa.
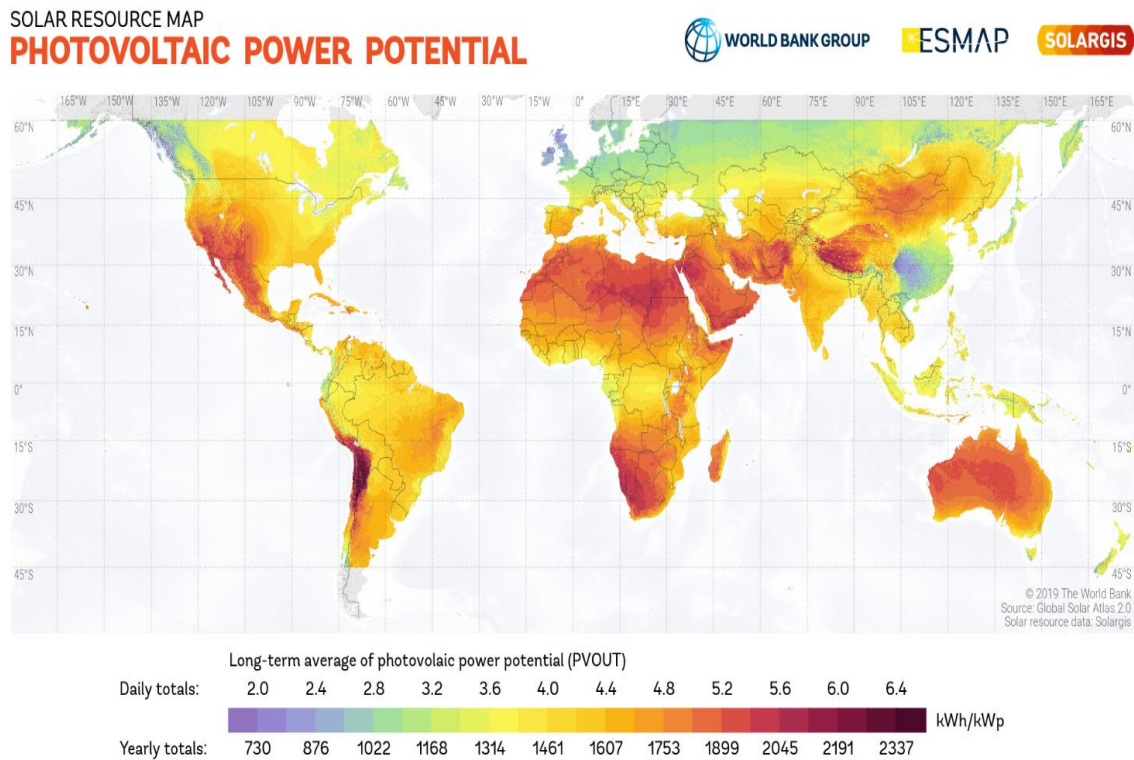
Figure 1.2: Global solar resource map obtained from Solargis [11].

1.2   Background and motivation of the study

This study focuses on Thermal Infrared (TIR) imaging of crystalline silicon PV cells, modules and arrays and is used in conjunction with associated characterization tools to analyse the behaviour of abnormal thermal signatures and I-V characteristics in PV systems. This study also aims to offer better insights into improving the operation of TIR imaging inspection methods for crystalline PV modules. In this study, thermal characteristics of cells refer to the temperature distribution on cells in a module, i.e., special features such as the abnormal thermal signatures. I-V characteristics mean the current and voltage measurements and parameters such as short circuit current, open-circuit voltage, maximum power voltage, maximum power current and the operating current and voltage point of modules and cells.

PV systems range from small, rooftop-mounted systems with capacities from several kilowatts to large utility-scale power stations of hundreds of megawatts. A PV system is

composed of arrays of parallel strings which contain several PV modules connected in series with each module consisting of series connected cells that are arranged in substrings. Different types of technologies of solar cells exist, as highlighted in Section 2.4. Operating silently and without any moving parts or environmental emissions, PV systems have developed from being small niche market applications into a mature technology used for mainstream electricity generation such as grid-tied and off-grid PV systems. Figure *1.3* shows a large PV plant, Solar Capital's De Aar PV Power Plant, in the Nothern Cape of South Africa consisting of hundreds of thousands of PV modules capable of generating 175 MW of electrical power [12][13].

Figure 1.3: Solar Capital's De Aar PV plant, in South Africa, having thousands of crystalline PV modules [13].

When PV modules are deployed in the field, they can generate power for more than 25 years. However, PV modules can degrade prematurely in performance despite the fact there are no moving parts for power generation. PV modules are installed outdoors and operate under changeable environmental conditions, such as varying temperature, wind speed and shading or soiling conditions, which cause irregularities in the operation of PV modules [14]. Crystalline silicon modules consist of cells, with fingers and busbars, which are connected in series in substrings to make up a PV module. PV module construction is described in Section 2.5. The series-connected cells arranged in substrings are meant to deliver an equal

amount of power to contribute to the overall module's power when operating in the field. The operational voltage and current of the series-connected cells are meant to be matched when the cells are subjected to similar operational conditions. However, dynamic environmental conditions can cause a cell-to-cell operational mismatch. Additionally, a mismatch in the operation of the cells can occur due to manufacturing shortcomings, which result in the non-uniform composition of cell-to-cell material. This inherent cell mismatch can also result in the series-connected cells producing and contributing differently to the overall module power. One of the main consequences of mismatch is the inability of cells to produce the same current with the result that underperforming cells are forced to operate at lower voltages, or even negative (reverse bias) voltages, resulting in performance degradation of the PV module [15][16][17].

PV modules can underperform due to cell anomalies such as cracks or shading [18][19]. Cracks can occur during the manufacturing of the PV modules or post-manufacturing stage during transportation, installation, or when carrying out maintenance in the field. Shading on PV modules can be caused by buildings, poles, trees, bird droppings and soiling. Shading due to soiling is dynamic in nature and is unavoidable since PV modules are installed outdoors at an inclination for optimum capture of solar radiation and conversion efficiency. The inclination angle can result in wind-blown dust settling on and shading the cells. Uniform shading minimizes the irradiance incident on the solar cells and in turn reduces the current and power generated by PV modules. Non-uniform shading further causes a mismatch in series-connected cells resulting in reverse biasing of the partially shaded cells [16][18][20]. Thus, influencing the I-V characteristics and temperature distribution in the affected module. Bypass diodes are incorporated in crystalline PV modules to minimise the mismatch effects, however, when the bypass diodes are activated, they cause the affected PV module to present multiple local I-V maxima points, but only one of them relates to the global maximum of the array [21]. Reverse biasing of cells and operation of bypass diodes is described in Section 2.6. PV system inverters ensure a continual supply of optimum power to the load by constantly tracking the maximum power point (MPP) of PV modules under different operational conditions. The inverter constantly tracks the MPP at which the array, as a whole, produces the maximum power current (I_{MP}) at maximum power voltage (V_{MP}) to deliver maximum power (P_{max}) to the load. Different algorithms such as Perturbation and

Observation (P&O), incremental conductance and intelligent MPPT techniques, are applied for MPP tracking inefficient PV systems. In direct coupled stand-alone PV systems the load dictates the operating point and thus the operational power that can be derived from the PV modules [22][23][24]. Understanding the behaviour of crystalline silicon cells under dynamic operational conditions is crucial for informed decisions during maintenance and for developing PV systems. Dynamic operational conditions refer to the change in different operational conditions such as irradiance, load, shading or soiling conditions.

Global research focuses on minimizing and isolating potential sources of any dysfunction, failure or abnormal operation for an optimum payback time of investments and extended operation period of the PV systems. Therefore, the operation and maintenance of PV modules are crucial for the early detection of cell anomalies that impact the optimum performance, return on investment, reliability, and longevity of the modules. PV cell performance and efficiency are fundamental to the overall operation of a PV module, string, array and the whole PV plant. The performance of PV modules has been studied for more than 20 years [25], and the investigation is still of paramount importance to improve the operation and maintenance of PV systems. PV module inspection techniques that are applied to detect cell anomalies include visual inspection, current-voltage (I-V measurements, electroluminescence (EL) and Thermal Infra-Red (TIR) imaging [16][26]. Physical defects can easily be identified through visual inspection while other defects/anomalies require I-V testing, EL and/or TIR imaging to be detected. The testing methods, not including Unmanned Aerial Vehicle (UAV) based TIR imaging that is conducted in situ, require more time to disconnect PV strings and modules, especially in large PV plants consisting of thousands of PV modules. UAV-based TIR imaging is widely applied in the PV industry since it is fast and cost-effective in locating underperforming solar cells [27][28]. TIR and I-V measurements are recorded under standard and steady meteorological conditions, constant temperature, low wind flow and clear sky with the modules receiving irradiance above 600 W.m^{-2} [20][29][30]. However, changes in operational conditions can influence the performance of individual cells in PV modules [31], and the results on TIR images.

There are plenty of research publications reflecting the increasing interest in the application of TIR imaging and the potential for fault diagnosis of PV installations [20][32][33]. Several large and small-scale performance studies provide estimates about performance loss,

including shading losses, in PV systems operating under real field conditions [25][34 - 37]. Correlation between the performance degradation, fault types and abnormal thermal signatures is discussed in published literature, and some explain the typical defects in crystalline silicon PV modules and their influence on the measured I-V curves, such as series and shunt resistances [16][38][39][40]. A direct relation between the performance losses and the thermal differences was observed through experimental work that was carried out by Vodermayer et al. [39], however, the quantification of effective loss with the abnormal thermal signatures is not yet published. Therefore, there is a need for further experimental studies or evaluation to gain additional insights into the performance and TIR imaging of crystalline silicon PV cells for improved operation and maintenance of PV systems. The increase in the number of PV plants and, as the existing field-mounted PV plants age, more faults emerge and there is an increase in scientific research in TIR imaging and maintenance of PV modules in recent years. Being able to detect, identify and quantify the severity of cell anomalies, cost-effectively, on operational PV modules is essential for a reliable, efficient and safe system. Therefore, detailed information regarding the behaviour of individual crystalline silicon PV cells under dynamic operational conditions can be obtained when TIR images of the modules are captured under different operational conditions with a concurrent recording of I-V characteristics.

The effective judgement and interpretation of thermal signatures in PV modules remain a challenge since many factors such as operational conditions, the emissivity of a target object, thermal reflections, capturing angle, etc., can influence TIR images [20][30]. When carrying out TIR imaging on large PV plants an enormous amount of TIR images is generated rapidly that generally require further classification to identify underperforming modules. Research has been carried out to automatically post-process the thermal images, based on the knowledge of PV modules failure patterns [41][42]. An algorithm was developed by Aghaei et al. to perform TIR image analysis to determine the percentage of degradation from specific defects on PV modules [43]. Tsanakas et al. proposed aerial triangulation and terrestrial georeferencing as two techniques for advanced inspection mapping of PV plants, using data recorded on aerial TIR imaging [44]. An approach for automatic detection and analysis of PV modules was proposed by Dotenco et al. by firstly detecting the individual modules in aerial TIR images and then detecting the defective modules using statistical

tests [45]. U. Jahn et al., [20] suggest that, several defects such as short circuits in solar cells, shunts, and inactive cell parts can be identified through TIR imaging, however the method can only identify cell failures causing a significant current mismatch with the good cells. A. Kandela et al [46], reviewed the recent advances in the involvement of TIR imaging in PV systems fault detection and diagnostics and highlighted that this method is a non-destructive PV inspection technique for condition monitoring and fault detection. The degradation or ageing impact on thermal signatures was investigated following real-time exposure to field conditions and by accelerated time ageing in an environmental chamber (e.g thermal cycling) [47][48][49]. Surprisingly, no visual defects were observed on other abnormal thermal signatures and also modules with visible damage showed no abnormal thermal signature. It was then assumed that, for such observations, when cell fracture occurs, the shunt resistance becomes sufficiently low for the temperature of the affected cell to increase significantly.

Tsanakas et al. reviewed the faults in PV modules in relation to the thermal and electrical characteristics and classified the faults according to their abnormal thermal patterns and electrical characteristics [50]. The effects of partial shading and short circuit failure of bypass diodes on thermal and electrical characteristics were analysed [51], by simulation and experimental lab-scale PV array. It was shown that a short circuit failure of a bypass diode reduces the module's open-circuit voltage by one-third with no impact on the module's short circuit current. The researchers, Tsanakas et al. and Geun Lee et al. studied the thermal and electrical characteristics of modules on array and string levels which were taken under typical and recommended testing conditions [50][51], however it is still a challenge to conclusively interpret TIR images. No studies have yet shown the electrical and thermal behaviour of modules, substrings and individual cells under different operational conditions; irradiance, cell shading level and load conditions. This study analyses and discuss the results obtained after experimental runs were conducted on crystalline silicon PV modules operating under real field conditions at the Outdoor Research Facility (ORF) at Nelson Mandela University, Eastern Cape, South Africa (34.0085ºS, 25.6652ºE).

1.3 Research Objectives

The study focuses on the analysis of TIR images and current and voltage measurements to understand the behaviour of thermal and electrical characteristics of crystalline silicon PV cells and modules under dynamic operational conditions to acquire useful information to improve the operation and TIR imaging inspection methods on operational crystalline silicon PV modules.

The main objectives of this study were to:

- investigate the behaviour of thermal and electrical characteristics of crystalline silicon PV modules by carrying out different experimental runs under different operational conditions, and
- analyse the obtained data for advancing the understanding and improved interpretation of thermal and electrical characteristics of the modules.

Several experiments were carried out under different loads, irradiance and cell shading levels while capturing, simultaneously, the thermal characteristics and operational current and voltage of individual cells using a datalogger and a TIR camera, respectively. The measurements were recorded while monitoring the environmental conditions with the weather station at the Outdoor Research Facility (ORF). Other PV module inspection methods such as visual inspection, I-V curve measurements and EL imaging were carried out on the modules to ascertain the observed abnormal thermal signatures. The temperature distribution and I-V curve characteristics of the PV modules were critically analysed, with the aid of FLIR Research Studio (FRS) and PVSim software, respectively, for detailed insights which can improve the operation and TIR imaging of crystalline PV modules.

This study focuses on the analysis of TIR images and current and voltage measurements to understand the behaviour of thermal and electrical characteristics of crystalline silicon PV cells and modules under dynamic operational conditions so as to acquire beneficial information to improve the operation and TIR imaging inspection method on operational crystalline silicon PV modules.

1.4   Thesis outline

This section summarises the contents of the chapters that follow.

Chapter 2: The chapter introduces the physics of semiconductors and gives a brief description of a p-n diode and the properties of solar cells. The characteristics and operation of PV cells and modules are discussed together with cell operation anomalies and PV module inspection techniques.

Chapter 3: This section presents the experimental layout showing how the results were obtained. This includes the equipment used, setups and the steps followed in applying the testing techniques, visual inspection, I-V measurements, TIR and EL imaging, on crystalline silicon PV modules.

Chapter 4: Detailed analysis and discussion of the observed results is presented in this section. The results show and discuss the dynamics of I-V and TIR characteristics of the crystalline modules under different operational conditions.

Chapter 5: The chapter summarises and concludes the research work.

Chapter 2

The Physics and characteristics of PV cells and modules

2.1   Introduction

A photovoltaic (PV) cell is a semiconductor device that is designed and constructed to efficiently absorb and convert solar radiation into electrical energy through the photovoltaic (PV) effect that was discovered by the French Physicist, Edmond Becquerel, in 1839 [52]. The amount of solar energy that is converted into electrical energy is quantified by the efficiency of the PV cell, which in principle, depends on the generation and recombination of the charge carriers when incident photons from the sun are absorbed by the p-n junction [53]. The performance of PV cells varies when exposed to dynamic operational conditions in the field which causes mismatched cells to operate abnormally [14]. Therefore, quality checks of PV modules through visual inspections, current-voltage (I-V) measurements, Electroluminescence (EL) and Thermal Infrared (TIR) imaging are applied for early detection of cell anomalies. This chapter provides an overview of the fundamental operational principles and the physics behind the functioning of the p-n junction to understand the basics for the PV cell operation. The basic principles of carrier generation and recombination mechanisms are discussed as well as semiconductor diode characteristics. The chapter also highlights the performance characteristics of crystalline silicon cells and methods of identifying mismatched cells are highlighted.

2.2   Principles of solar cells

Photovoltaics cells operate by producing direct electric current from photon absorption, based on exploiting electronic properties of a special class of materials called semiconductors. The conversion process is performed by solar or PV cells. Solar cells use the principle of the photovoltaic effect, which is the direct conversion of sunlight energy into electrical energy [15][54]. They are produced from semiconductor materials by doping with electron acceptor elements (group 3 elements on the periodic table) to obtain positive charge carriers called holes, making the semiconductor layer p (positive)-type. Doping the semiconductor with electron donor elements in group 5 on the periodic table creates negative charge carriers and makes the semiconductor layer n (negative)-type. Doping of intrinsic semiconductors

materials, usually silicon, with impurities to have extrinsic semiconductors, improves the electrical properties of semiconductors by changing the electron and hole carrier concentrations [52][55]. The imbalance of electrons and holes also affects the Fermi/energy level by causing it to rise towards the conduction band, in n-doped material, and to drop towards the valence band, in p-doped semiconductor, as indicated in Figure 2.1
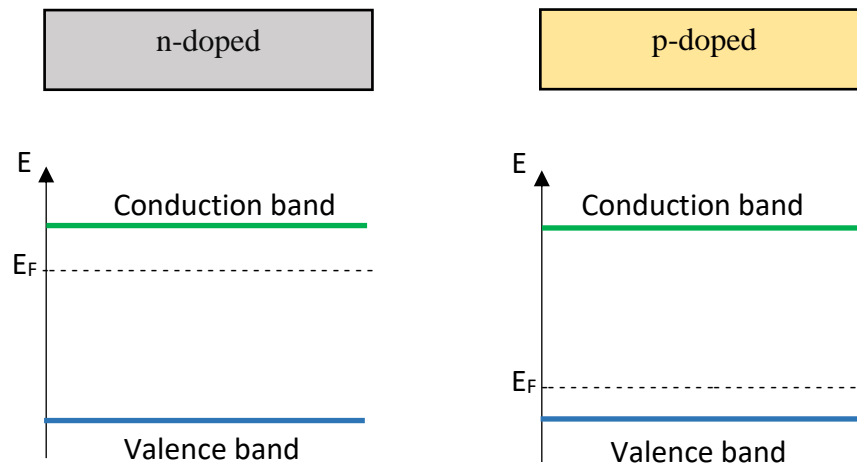
Figure 2.1: Fermi level effect on isolated p and n materials.

The relative shift of the Fermi level allows electrons to reach the conduction band and determines how easily materials conduct electricity. The closer the Fermi level is to the conduction band the easier it will be for the electrons in the valence band to transition into the conduction band. In a p-doped material, a small amount of energy is required for an electron to leave the valence band and occupy the acceptor energy level creating holes in the valence band and drift of charge carriers [55][56].

Figure 2.2 shows electrons in their valence shells which gain thermal energy and get excited to the conduction band. When an electron gains a quantum of energy greater than the energy gap (ΔE_G) it jumps the forbidden zone to the conduction band and constitutes the creation of an electron-hole pair which increases the mobility of charge carriers and electrical properties of the material. If a neighbouring electron fills the hole in the valence band, it will leave a hole adjacent to it [54][55]. This process will continue and create current. Current generation in PV cells is described in Section 2.3.1.
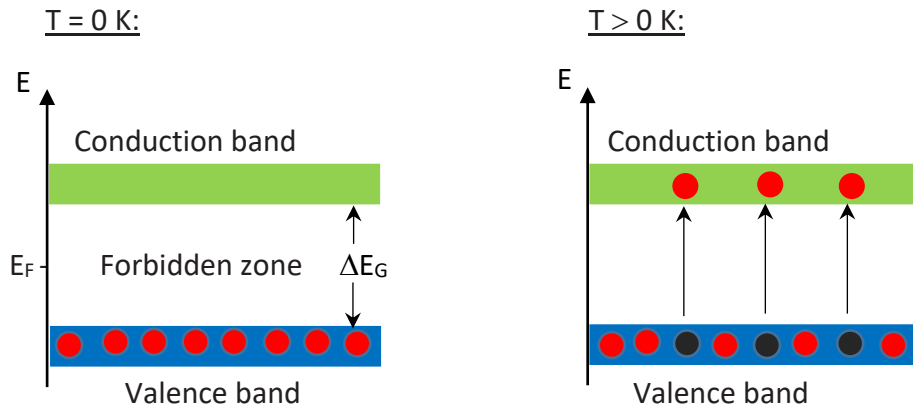
Figure 2.2: Thermally excited valence electrons overcome the band gap to the conduction band (adapted from [6]).

2.3 The p-n junction

When a semiconductor material such as silicon (Si) is doped with boron, positive charge carriers called holes are obtained making the semiconductor layer p (positive) type, and n (negative) type is created by doping with phosphorus. Joining the p-type and n-type semiconductors creates a p-n junction with a built-in electric field set up, in the region of the junction, due to the diffusion of electrons as they try to evenly distribute themselves. A depletion region is created between the p and n-type materials and the charge carriers can drift when the region is exposed to light [53][56].

2.3.1 Current generation in a PV cell

The photoelectric action is when PV cells directly convert sunlight energy into electrical power. The photons that are incident on a PV material are either reflected off the cell, pass through the cell or are absorbed by the semiconductor material. The absorption of the incident photons in the semiconductor material that forms a p-n junction results in the excitation of an electron, as described in Section 2.2, and the generation of charge carriers (electrons and holes). The charge carriers are separated, with the electrons collected in the n-type region and the holes are collected in the p-type region, resulting in a voltage appearing across the device (p-n junction). The separated charge carriers flow through an external load connected to the terminals of the PV cell to generate electrical current. Photons entering the p-n junction having energy less ΔE_G of the cell material, not contributing to the generation of current. Figure 2.3 illustrates this phenomenon of photovoltaic effect. The p-n junction's

electric field provides the voltage for the PV cell which is of the order of 0.6 V for a crystalline silicon PV cell [52][57].
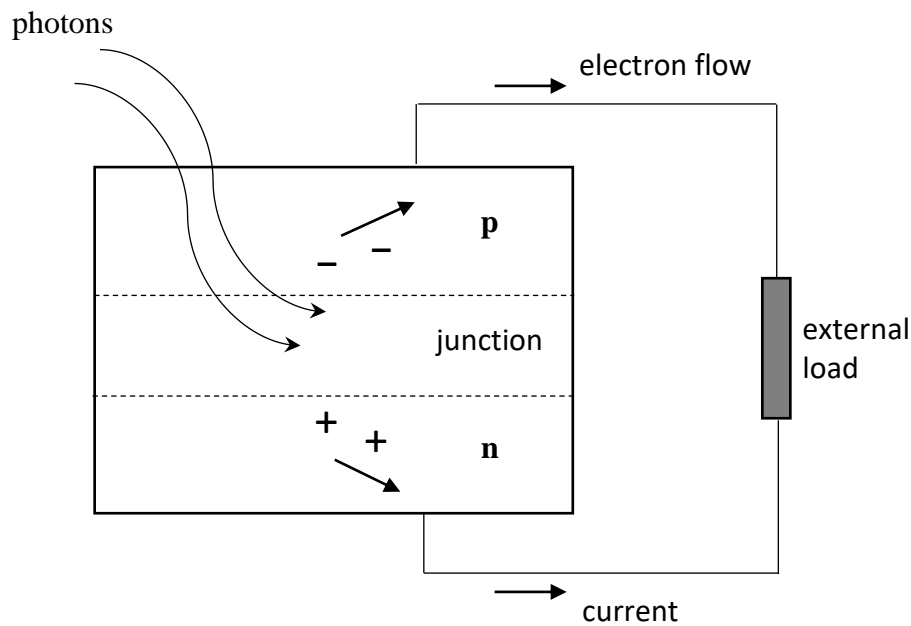
Figure 2.3: The photoelectric effect in a PV cell.

The idealized equivalent circuit of a PV cell is shown in Figure 2.4, and the source current I, which results from the excitation of electrons by the photons, flows to the external load of resistance R_L when the diode voltage is V.
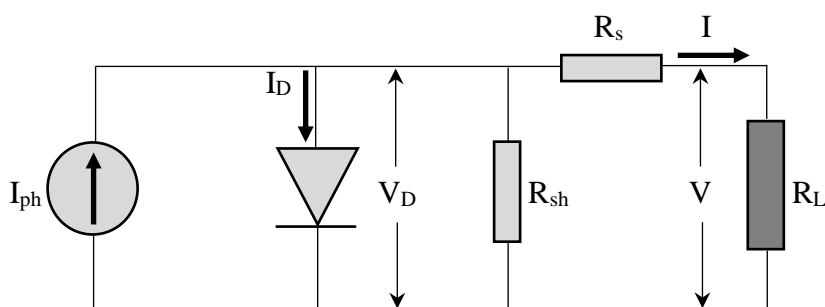
Figure 2.4: Simplified equivalent circuit of a PV cell showing parasitic series and shunt resistances, R_s and R_{sh}, respectively.

A PV cell is a non-linear device that can be represented as a current source (one-diode) model as shown in Figure 2.4. The current source I_{ph} represents the cell photocurrent, I_D is the diode current, R_{sh} and R_s are the intrinsic shunt and series resistance of the cell, respectively. Usually, the value of R_{sh} is very large and that of R_s is very small, such that no current pass through R_{sh}, hence R_{sh} and I_{sh} may be neglected to simplify the analysis. R_s is due to the

resistance of the movement of current through the p-n material of the PV cells, the metal contacts and the busbars and it limits the current (I) generated under light conditions. The voltage (V) across the load is given by equation 2.1, which shows the sum of voltages according to Kirchhoff's voltage law.

$$V = V_D - IR_S \qquad\qquad 2.1$$

The current I, produced by the cell is given by equation 2.2, following Kirchhoff's current law.

$$\mathrm{I} = I_{ph} - I_D \qquad\qquad 2.2$$

I_D is given by equation 2.3 [4], and combining equations 2.1, 2.2 and 2.3 yields equation 2.4 which represents the one-diode model equation.

$$I_D = I_S \left(e^{\frac{qV}{nkT}} - 1 \right) \qquad\qquad 2.3$$

where: I_S = the saturation current of the p-n junction

q = elementary charge

n = ideality factor of the diode

k = Boltzmann's constant

T = absolute temperature

$$I = I_{ph} - I_S \left(e^{\frac{q(V+IR_S)}{nkT}} - 1 \right) - \frac{(V+IR_S)}{R_{sh}} \qquad\qquad 2.4$$

Equation 2.4 describes the electrical behaviour of a PV cell. The electrical characteristics, current, voltage and resistance of the cell are described in Section 2.6. The generated direct current (DC) can lately be converted by inverters in a PV system to obtain an alternating current for suitable usage [58][59][60].

2.4   PV cell technologies

PV cells are made from materials such as silicon (Si), germanium (Ge), cadmium telluride (CdTe), gallium arsenide (GaAs), copper indium diselenide (CIS), etc. Silicon is the most used because of its great abundance in the Earth's crust [52][54]. There are two types of PV cell technologies that dominate in the PV industry namely crystalline silicon and thin-film. Crystalline silicon consists of polycrystalline (multi-crystalline) and mono-crystalline (single

crystalline) PV cells which are known to deliver the highest efficiency [61], under standard test conditions, compared to the polycrystalline and thin-film cells. The average maximum conversion efficiency of PV cells is around 20%. The production of thin-film cells is less complex, although their efficiency is less than that of crystalline silicon cells. Crystalline silicon PV is the most widely used PV technology [16][57][62]. A typical PV cell of polycrystalline silicon technology is shown in Figure 2.5 with cell fingers connected to five busbars.
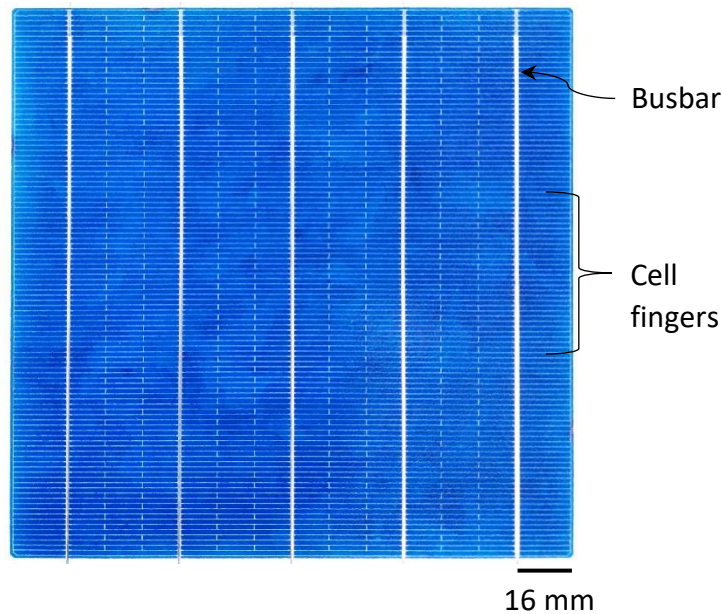
Figure 2.5: A typical polycrystalline silicon PV cell showing fingers and busbars.

2.5 PV module construction

PV cells generate a small amount of power, so they are often assembled and encapsulated to form PV modules that produce higher power at a desired current and voltage. The module structure differs with cell type and module application [16][26][54]. A typical crystalline PV module layout comprises 6 columns X 10 rows (or 6 x 12) of cells. Figure 2.6 shows a configuration of crystalline silicon cells and diodes in a crystalline silicon module. The cells are usually numbered from top left through the substrings SS1, SS2 and SS3 to top right.
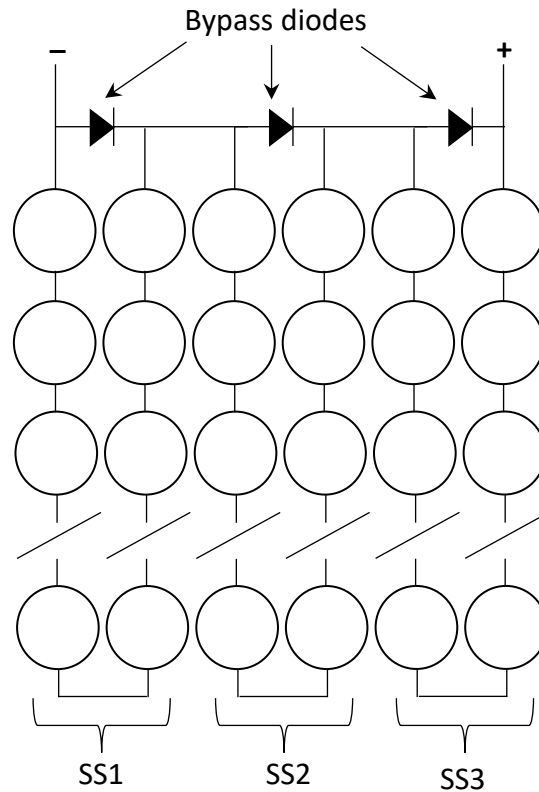
Figure 2.6: Layout of cells and bypass diodes in a crystalline silicon PV module. Each substring (SS1, SS2 and SS3) has a bypass diode in parallel to it.

Figure 2.7 shows the components which make up a PV module of crystalline silicon technology. PV cells are sandwiched between the transparent front glass and a back sheet using an encapsulant, for protection from mechanical damage and moisture ingress. The frame binds the layers to reduce flexibility and is also used for mounting purposes in the field. The junction box is a terminal point for electrical connections and contains bypass diodes.
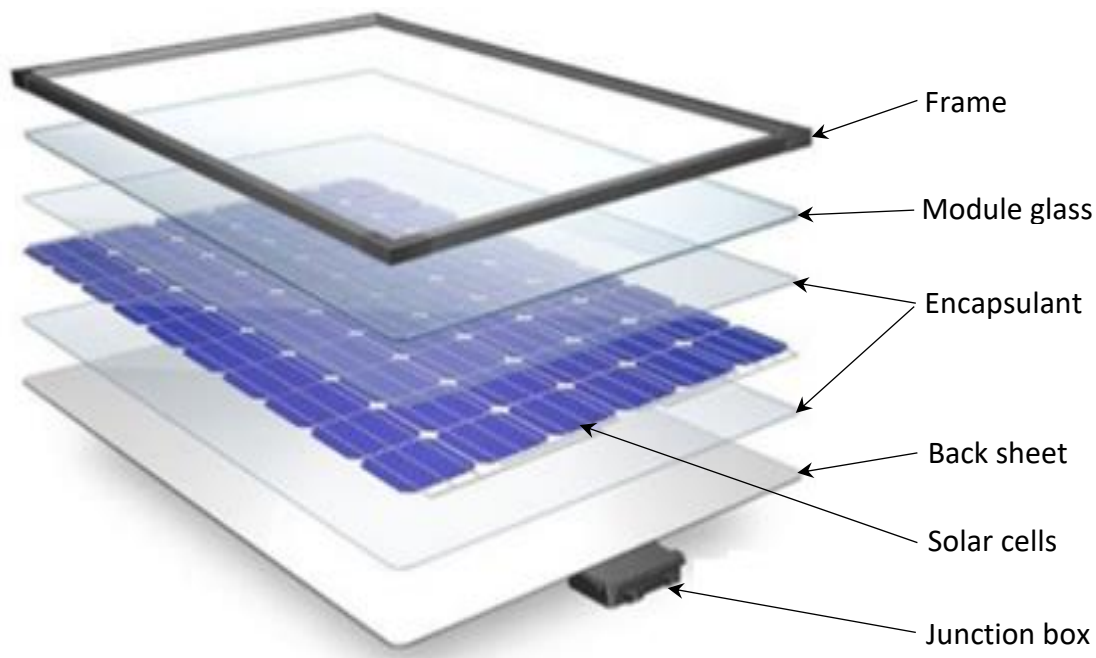
Figure 2.7: Structure of a crystalline silicon PV module [62].

PV modules are interconnected in a series and/or parallel configuration to form PV strings and arrays which can be linked to load through inverters that have MPP tracking systems and ensure conversion of maximum PV power to alternating current (AC) power.

Half-cut solar technology has the standard PV cells split in half to increase the number of cells, module's voltage and maximum output power. Bifacial PV modules have a transparent back sheet, or glass which enables solar energy that reflects from the ground to reach the cells also from the backside. This increase absorption of solar energy by the cells and results in increased power generation from both sides of the PV cells [3][57].

2.6 Characteristics of crystalline silicon PV cells and modules

2.6.1 Electrical parameters of cells and modules

The electrical performance of PV cells and modules is described by their I-V characteristic curves and is determined by several factors including irradiance, temperature, cell type and interconnection of the cells. The performance parameters of a PV source are obtained by measurement of their current-voltage (I-V) values using I-V curve tracer or analyzer. Figure 2.8 shows I-V characteristics, simulated in PVSim [64], of a silicon PV cell, substrings and module. The module's I-V curve is indicating key points (performance parameters) on the curve, open-circuit voltage (V_{OC}), short circuit current (I_{SC}), current and voltage at the

maximum power point, I_{MP} and V_{MP}, and the maximum power (P_{max}). The voltages of the substrings at any current value add up to give the module's voltage at that particular current, e.g., at zero amps, the V_{OC}s of the three substrings, in Figure 2.8, give the V_{OC} of the module when added. The number of cells in each substring can be obtained by comparing the V_{OC}s of the cell and the substring, and in this scenario (Figure 2.8) each substring contains 10 cells.
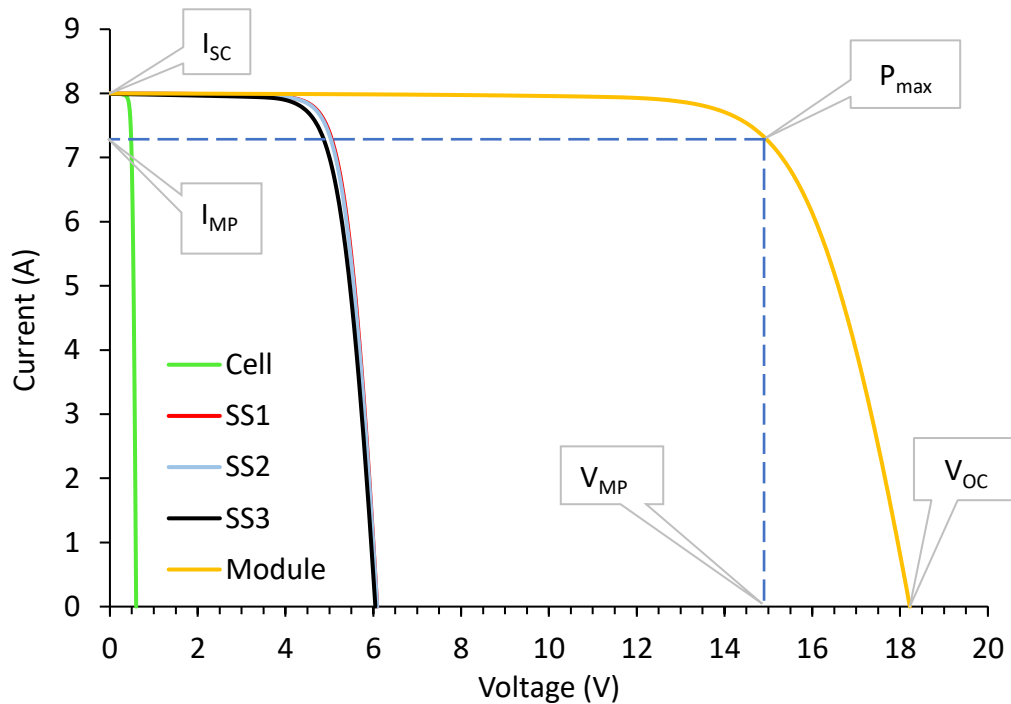
Figure 2.8: I-V curves of a cell, substrings and module simulated under standard test conditions in PVSim. The performance parameters of the module are indicated.

The power at any point along the I-V curve in Figure 2.8 is a product of current and voltage, and the maximum power point (P_{max}) is located around the "knee" of the I-V curve.

Since P = VI, it implies that

$$P_{max} = I_{MP}V_{MP} \qquad\qquad 2.7$$

PV modules are rated at the maximum power under standard test conditions, (STC): 25 ˚C, 1 kW/m², and ASTM air mass of 1.5 according to the standards, American Society for Testing and Materials (ASTM) G173-03 and IEC 60891:2009 [65][66]. However, the output power is influenced by operational conditions in the field. Identifying individual modules having low output power usually involves visual inspection, taking I-V measurements, Electroluminescence (EL) or Thermal Infrared (TIR) imaging. Visual inspection forms part of

19

the maintenance procedures for PV modules in the field and can easily locate failures and defects in PV modules [60]. However, some defects are not visually detectable, hence the importance of other inspection methods.

2.6.2 Current mismatch in crystalline silicon PV cells

PV modules consist of several cells that are connected in series, as described in Section 2.5, which should ideally be electrically matched. However, cells can contribute differently to the overall module power when they are mismatched and operating at current and voltage different from their MPPs.

When a PV module is illuminated, all cells contained in the PV module must generate equal current. Figure 2.9 illustrate this phenomenon diagrammatically when the cells (cell 1 to cell n) receive equal irradiance and generate equal current (I_1). The I-V curves in Figure 2.9 show that the operating points (OP) of the cells are matched and the cells are generating current (I_1) at their maximum power point (MPP).
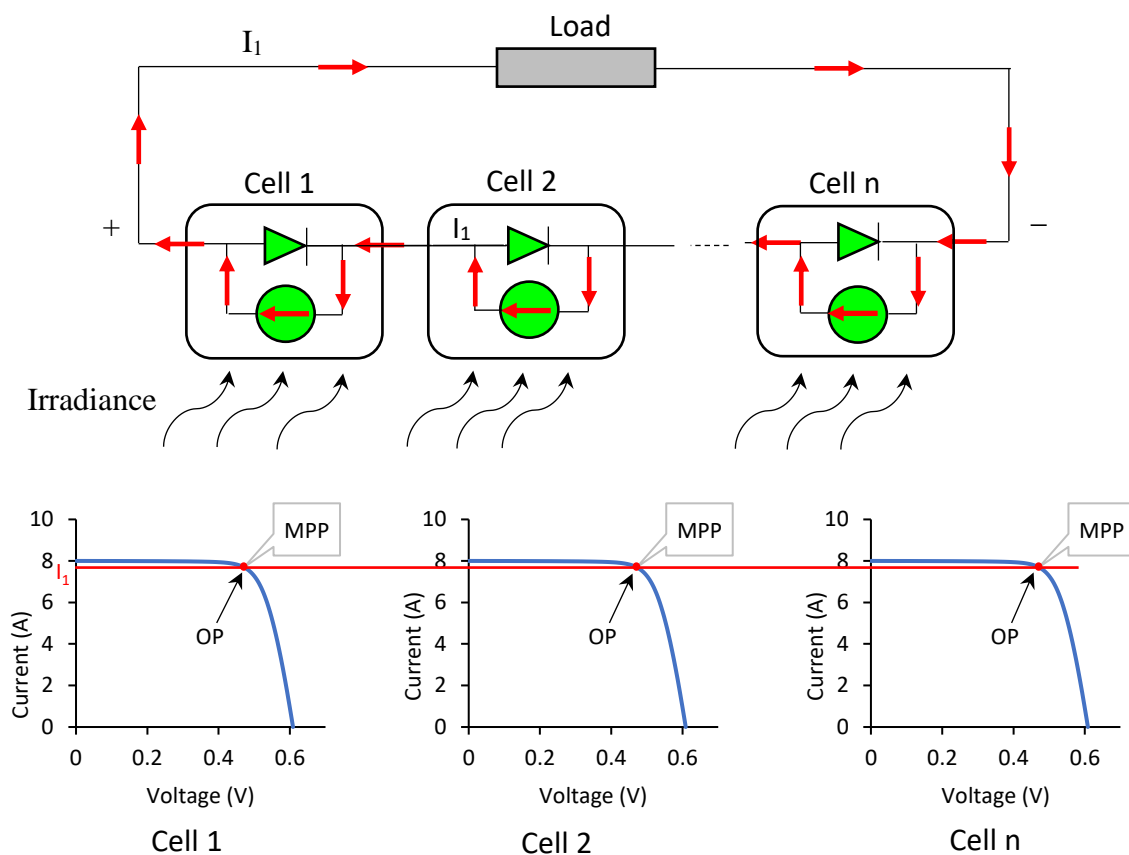
Figure 2.9: PV cells connected in series and producing equal current. The cells operate at their maximum power points (MPPs).

When a cell in a series connection underperforms, it produces less current than the good cells such that the overall current of the substring is reduced. This occurs when the cell is totally or partially shaded, cracked or electrically mismatched. Figure 2.10 shows a shaded cell 2, receiving less solar energy than other cells (cell 1 to cell n, excluding cell 2) and generating less current, I_2, thus $I_2 < I_1$. The I-V curves of the individual cells, generated in PVSim [64], are also shown in Figure 2.10 and indicate the operational point (OP) of each cell shifted from the expected maximum power point (MPP) due to partial shading.
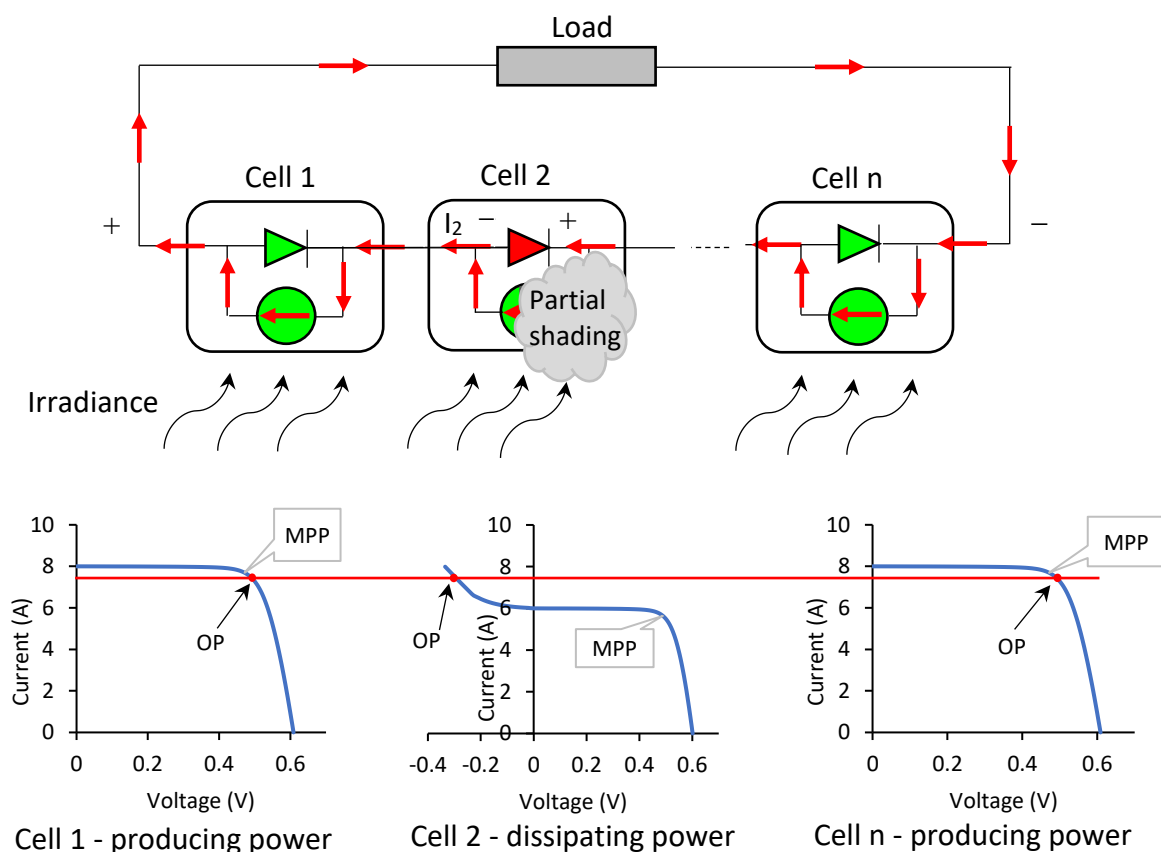
Figure 2.10: Current mismatch in substring cells due to partial shading. The I-V curves show the operating points (OPs) of the cells differ from the maximum power points (MPPs).

The mismatch forces the shaded cell to pass current higher than its generation capabilities and become reverse biased, and can even enter the breakdown state [67], which results in the cell dissipating power instead of generating it, thus affecting the operational temperature of the cell. The electrical energy lost is related to the operational electrical parameters of the reverse-biased cell [68][69]. The cell operating temperature is affected by the cell's localised conditions mainly (i) external; direct heating by the sun and/or cooling from air movement,

and (ii) internal; energy absorbed or dissipated by the cell. A hot cell could thus result from direct heating from the sun or resistive dissipative heating from reverse bias mismatch. A cell that is not operating at its maximum power point (MPP) may be hotter since the sun's incident energy may not be generating maximum electric energy. Section 2.6.5 describes how hot cells can be identified on operational modules using TIR imaging. If the mismatch is severe enough to cause reverse bias, then resistive heating (power loss) from the cell occurs. Any factor that impedes a cell's ability to produce the same current at a matching voltage to the other cells in the substring causes mismatch.

2.6.3 Operation of Bypass diodes on mismatched cells

In general, a bypass diode allows current to pass through it when in forward bias. This phenomenon is applied in crystalline PV modules to reduce the destructive effects on mismatched cells connected in series. Ideally, there should be one bypass diode parallel connected on each cell, however this will be costly. Therefore, bypass diodes are connected in antiparallel, with reverse polarity between substrings of cells, [70][71], as shown in Figure 2.12. Usually, the maximum number of crystalline silicon cells in a substring is 24, so as not to reach the junction breakdown voltage, which is about -15 V, when a cell is reverse biased [71][72]. A poor performing cell in a substring causes the affected substring to generate less power, as it delivers voltage and current different from its V_{MP} and I_{MP} values. When the cell is severely mismatched with good cells, it causes the substring's voltage to be negative which in turn creates a forward bias potential difference on the respective bypass diode and activates the bypass diode. Without a bypass diode the reverse bias voltage of the underperforming cell can reach junction breakdown voltage and can cause localised excessive heating, damage to the module and risk of fire. The onset point for activation of the bypass diode changes with types of bypass diodes [73]. For conventional Schottky bypass diode, the forward bias voltage for activation is low and ~0.35 V [72]. Any further increase in the forward bias voltage, from the onset voltage, will result in more current passing through the bypass diode until all the maximum possible module current pass through the bypass diode, thus protecting the poor performing cell from reaching the reverse breakdown voltage.

The bypass diodes incorporated in the junction box of crystalline silicon modules function to divert some current around a substring containing underperforming mismatched cells, as shown in Figure 2.12, thus minimizing their detrimental effect and optimizing the overall module current and power output. Figure 2.12 shows two mismatched cells in substring SS1, which resulted in the module current I_M not passing through substring SS1, but through the bypass diode parallel to substring SS1 and substrings SS2 and SS2 containing no mismatched cells. Substring SS1 generates current (I_S) which is less than I_M. Figure 2.11 shows the I-V curves of two substrings, SS1 and SS2, that were generated in PVSim [64]. An I-V curve 1, in the figure, shows a combination of the two substrings when SS2 is matched and operating as SS1. I-V curve 2 is a combination of the substrings when the substrings are mismatched, with their short circuit currents assumed to be 8 A and 7 A, respectively. The I-V curve 2 shows a bump which indicates that the bypass diode on SS2 is active, thus allowing current to pass through it, due to the forward bias voltage created across it when there is significant current mismatch between the substrings.

Starting at V_{OC}, the point where the substring's bypass diode starts to affect the normal I-V curve of the module occurs at the inflection point on the I-V curve. However, the onset activation voltage of the bypass diode is defined as indicated on the I-V curve 2, in Figure 2.11, and occurs when a significant or measurable current flows through the bypass diode on SS2. The current passing through the bypass diode will increase to a maximum value which is less than I_{SC} with an increase in current mismatch between SS1 and SS2, resulting in all the module's current passing through the bypass diode on SS2. The bypass diode conducts current in trying to lessen the mismatch effects but cause no significant change on the open circuit voltage V_{OC}s of SS2 and I-V curve 2 as indicated on the figure. When the bypass diode is fully activated, most of the module's current is diverted around substring SS2. The bypass diode on SS2 will ensure that the power generated by SS1 is still available. The effects of bypass diodes on the I-V characteristics are also highlighted in Section 2.6.4.
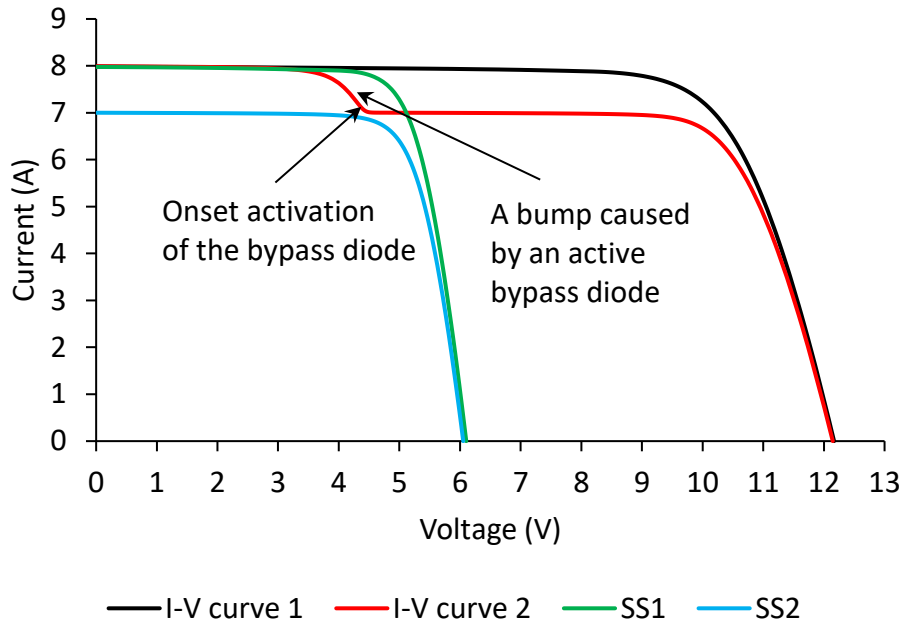
Figure 2.11: SS1 and SS2 show individual I-V characteristics of mismatched substrings, which when combined yield I-V curve 2 with a bump indicating an active bypass diode. I-V curve 1 is a combination of the substrings when they are matched, with SS2 operating normally as SS1.

Bypass diodes can fail in two modes: short circuit mode or open circuit mode. The short circuit mode results in the module's power cut by one-third while the open circuit mode can force the underperforming cell into extreme reverse bias, causing cell breakdown, overheating and in the worst-case scenario a fire hazard [16][74]. The effect of partial shading and the effect that the bypass diodes have on the shape of I-V curves is shown in Figure 2.13 and also discussed in literature [75][76][77].
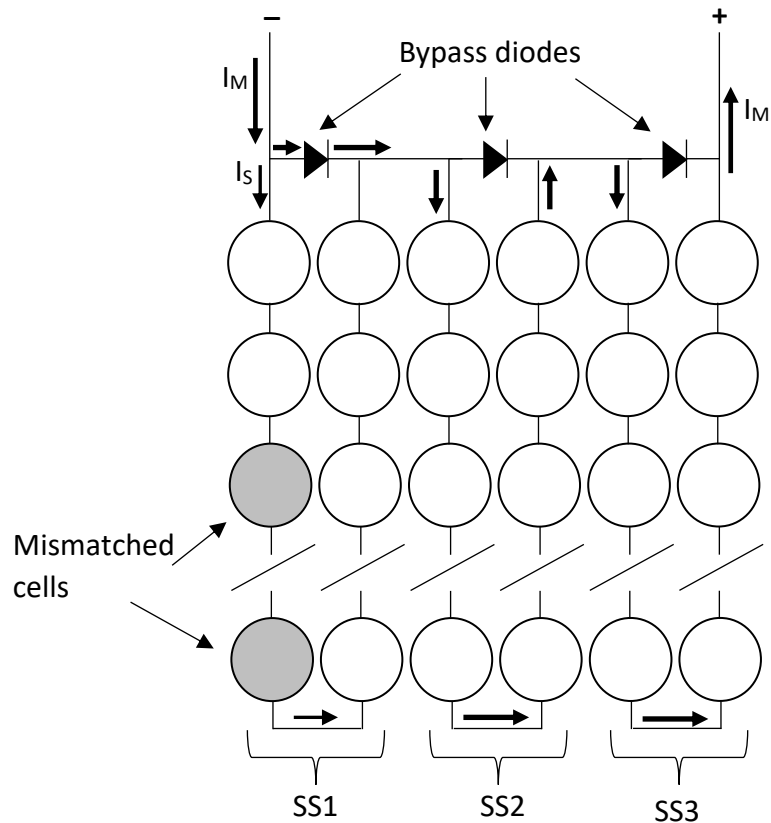
Figure 2.12: Three substrings, SS1, SS2 and SS3, containing series-connected cells and illustrating mismatch which result in the module's current (I_M) passing through the bypass diode paralleled to SS1. The substring current (I_S) is less than the module current (I_M).

2.6.4 I-V characteristics

PV analysers such as Solmetric and Photovoltaic Engineering (PVE) I-V curve tracers are used for taking I-V characteristics or power measurements of PV modules in the field. An I-V curve tracer works by sweeping a load across the operating range of a PV source. It simultaneously measures the output current and voltage at different operating points between I_{SC} and V_{OC}. The I-V measurements taken using I-V curve tracer are usually translated to STC for comparison [66][78]. When measured I-V characteristics deviate substantially from the expected, then the changes in the shape of the I-V curve can highlight possible clues regarding the probable failure mode. The deviations typically fall into one of the categories:

i. Different in I_{SC}

ii. Different in V_{OC}

iii. The slope near I_{SC} differs

iv.   The slope near V_{OC} differs

v.   Bumps on the I-V curve

vi.   Rounder or inner "knee"

Any cell anomaly or impairment that mismatches the key points of the measured parameters from the expected values reduces the output power of the PV source [79][80]. Figure 2.13 shows the effects of different forms of performance-limiting anomalies on I-V curves of a PV module. The I-V characteristics were simulated in PVSim [64], and changes in I_{SC}, V_{OC}, series and shunt resistances and mismatch are seen on the I-V curves.
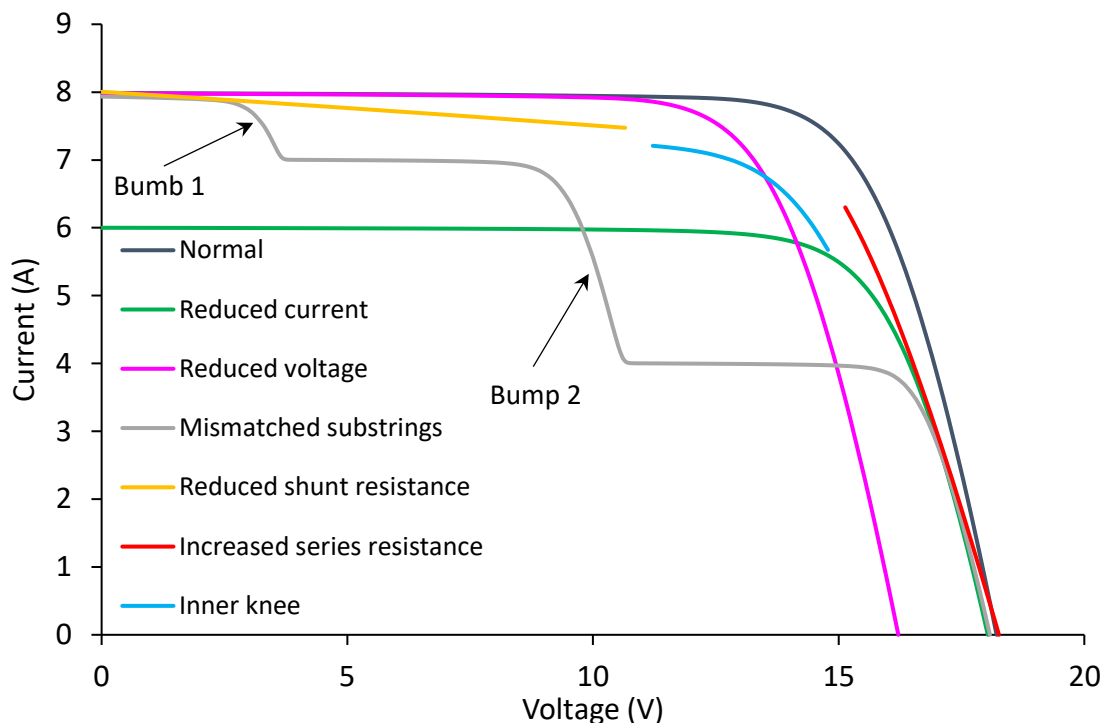
Figure 2.13: I-V curves deviate from the normal. The I-V characteristics of the PV module were simulated in PVSim and reflect the impact of different anomalies on the I-V curves.

The I-V curve having **reduced current** from the expected (**normal** I-V curve) is shown in Figure 2.13. When uniformly reduced irradiance is incident upon PV cells, the current generated is lower than at higher irradiance. The overall shape of the I-V curve is normal, but with a reduced current at each voltage. Shading on PV modules can be caused by buildings, poles, clouds, bird droppings and soiling. PV modules are prone to soiling just like any outdoor surface. Wind-blown dust can settle on PV modules resulting in (i) uniform or (ii) partial

shading on PV cells as shown in Figure 2.14 (a) and (b), respectively. Figure 2.14 (c) shows partial shading due to trees.

| Uniform soiling | Soiling on bottom row cells | Shading due to trees |
| a | b | c |
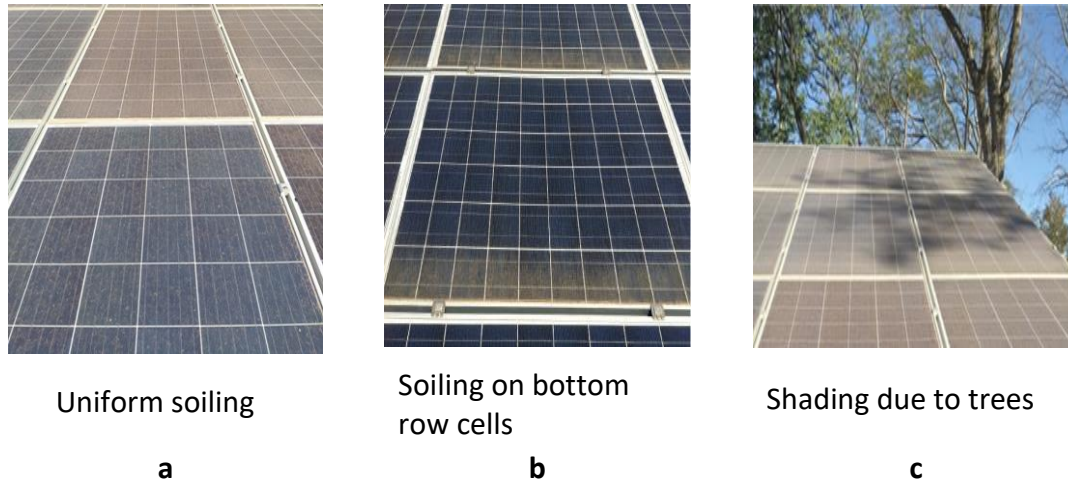
Figure 2.14: Shading on crystalline silicon PV modules.

Partial shading creates a mismatch in electrical characteristics of PV cells [18], as explained in Section 2.6.2, and further causes non-uniform temperature distribution in the affected module when the partially shaded cells operate at elevated temperatures. The localised heating can be minimised when bypass diodes, incorporated in crystalline, are activated [81]. However, when the bypass diodes conduct current, as described in Section 2.6.3, they cause bumps in I-V curves of the crystalline PV modules, as seen on the I-V curve of **mismatched substrings** in Figure 2.13 and affect performance. The bumps reflect the level of mismatch in the affected substrings [18], thus bumps 1 and 2, on the I-V curve of mismatched substrings in Figure 2.13, revealing light and heavy mismatch, respectively. The bypass diodes can create multiple local MPPs, which can be difficult for the maximum power point tracking (MPPT) to find the global MPP of an array [82].

Cell defects, such as cracks, can lower shunt resistance and/or increase series resistance in affected PV modules and result in a change in slope of the I-V curve near V_{OC} and I_{SC}, respectively [83]. Shunt losses occur when the generated current passes in a path that is not intended and is revealed by a sloped I-V curve for voltages just above 0 V and is revealed by the I-V curve of **reduced shunt resistance** in Figure 2.13. This occurs when there is low shunt resistance and can degrade the efficiency of the cells [16][79]. The generated current has to flow with no/low series resistance, however, defective cells can have fingers disconnected

from busbars and result in series resistance losses and steepness of the slope of the I-V curve near V_{OC}. The I-V curve revealing **increased series resistance** is shown in Figure 2.13. Severely damaged cells can cause the "knee" of the I-V curve to shift inwards and a reduction in V_{OC}, thus affecting the Fill Factor and performance of the affected PV source [79]. The I-V curves having **inner knee** and **reduced V_{OC}** are shown in Figure 2.13.

2.6.5 EL characteristics

Performance limiting defects on PV modules, such as cracked cells, are usually not observable on visual inspection but can be detected when the cells are forward biased when the module is in the dark to produce light in a non-destructive reverse photovoltaic process called Electroluminescence (EL) imaging. EL imaging has developed into a very successful defect identification and module characterising technique and nowadays can be performed not only in the Laboratory but also on-site using special tripods or drones [84]. There are two main sensors that commonly used for EL imaging: the Charge Coupled Device (CCD) and the Complementary Metal Oxide Semiconductor (CMOS) which differ in resolution, sensitivity, spectral response and cost. The main key specification for EL camera systems is derived from the need for the camera to be sensitive to the emission spectra of the material being tested. For a crystalline silicon solar module the emission spectra has a peak at 1150 nm [85]. The CCD sensor is very popular and much used due to their relatively low cost and high resolution. The high pixel count of the silicon CCD combined with good optics helps enable a finer spatial resolution in the EL image as compared to CMOS sensors which are more susceptible to noise although they are faster than CCD counterparts [85][86][87][88].

EL occurs in a PV cell when it is forward biased, receiving an electrical input and outputs an electromagnetic emission spectrum. An electric current of approximately equal to I_{SC} is delivered to the cells then radiative recombination of carriers causes light emission. The emitted EL intensity is related to the cell defects since a non-defective cell has homogeneous bright light distribution while the defective cell or cell part appears dark [20][89]. Other cell defects that are identifiable on EL imaging include shunted cells, disconnected cell interconnects, cells affected by PID and shunted bypass diodes [16][26]. Figure 2.15 shows a damaged cell having cracks that caused electrical isolation of cell parts. The maximum image resolution and illumination level is obtained when the optical axis of the EL camera is placed perpendicular and as close as possible to the string, module or cell under test.

28
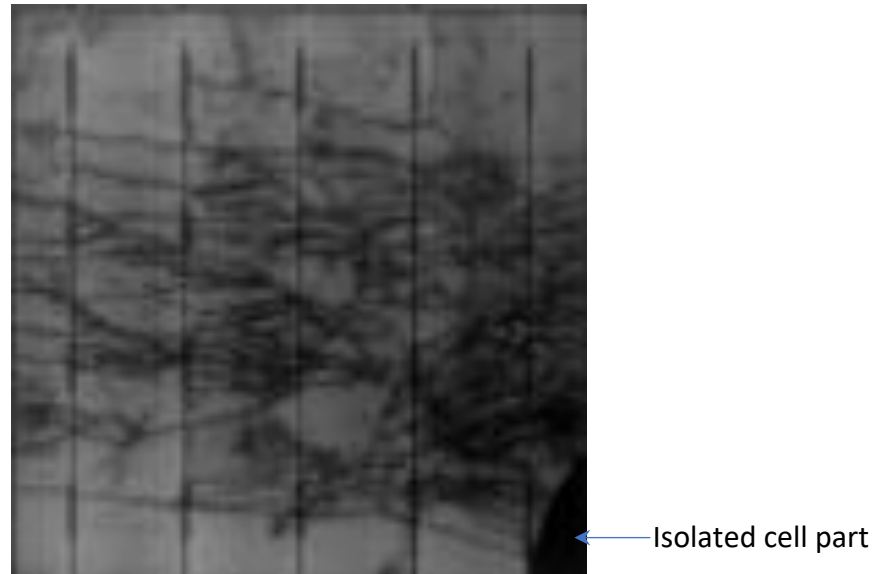
Isolated cell part

Figure 2.15: EL image of a PV cell showing isolated (dark) parts due to cracks.

Cracks that run along the busbars may not disconnect the fingers from the busbars and cannot impact on the performance of the cracked cell. However, other cracks can completely disconnect the fingers and busbars, resulting in the isolation of cell parts and creating a significant mismatch which can affect the normal operation of the cell [90][91][92].

It is beneficial to take EL images at high current, ~I_{SC} (High EL image), and as well as at low current, 10% of I_{SC}, (Low EL image) since some cell anomalies such as Potential Induced Degradation (PID) are detectable on low EL images. PID can cause shunting on p-n junction of crystalline PV cells and affects the fill-factor and power generation on the PID affected cells [16][20][93].

2.6.6 Thermal characteristics

2.6.6.1 Thermal Infrared imaging of PV modules

When PV cells underperform, they can operate under reverse bias conditions and dissipate electrical power produced by other cells in the form of heat, leading to localized heating and is detectable as a hot cell on TIR imaging. All matter with non-zero temperature has their particles in kinetic interaction which result in a charge, (protons and electrons) acceleration and dipole oscillation resulting in an electromagnetic generation [57][94]. The characteristics of thermal radiation depend on properties of the surface/material it is emanating from, emissivity and temperature which are related by Kirchhoff's law of radiation: at thermal equilibrium the emissivity and absorptivity of a surface at a given temperature and

29

wavelength are equal. Additionally, according to Planck's law, the radiated energy increases with the temperature of an object. This enables the temperature of objects to be known through TIR imaging [95]. TIR cameras make use of this property to measure the infrared radiation, characterised by infrared electromagnetic radiation in the wavelength range of 8 − 12µm, emitted from a targeted object. The observed infrared radiation is used to calculate the temperature of an object using the Stefan-Boltzmann equation given by

$$Q = \varepsilon \sigma T^4 \hspace{4cm} 2.8$$

where Q is the radiation heat of an object, ε is the emissivity of the surface, σ is the Stefan-Boltzmann constant (5.67×10^{-8} W.m^{-2}K^{-4}) and T is the surface temperature in Kelvin. The emissivity of a surface is defined as the ability to emit energy in the form of radiation under fixed thermal conditions [96].

For in-Lab dark TIR imaging, the images are taken when the PV module under test is under forward bias conditions by using an external power supply. Several TIR images are taken from the back sheet side at predefined time intervals. When operating in the field under sun illumination, then Unmanned Aerial Vehicle (UAV) based or on-ground based TIR imaging is conducted under steady state conditions. TIR imaging is an extensively used technique applied to identify modules having thermal abnormalities in PV plants. Other auxiliary information, which is helpful in image analysis, can be obtained when TIR imaging is combined with geo-referencing technique. TIR imaging is ideally conducted on operational PV modules under steady ambient conditions, by qualified personnel. However, PV modules operate under dynamic climatic conditions which influence the overall operation of the cells and modules [20][44].

TIR cameras acquire infrared radiation from a target object and transform it into an electric signal which can be imaged from the camera. The TIR camera also receives reflected radiation from the surroundings, therefore parameters such as emissivity, which is typically > 0.85), atmospheric temperature and humidity should be entered into the software of the camera. The TIR cameras that are commonly used for PV applications are the micro-bolometer which have uncooled sensors and can work at ambient temperatures. The cameras with micro-bolometer are affordable and uncomplicated to work with. The cameras with cooled sensors

have high sensitivity, however they are not used in PV applications since they are costly and complex in their cooling system [20][97].

TIR imaging of operational PV modules is generally misinterpreted because of the dynamic nature of some types of anomalies and the dynamic nature of the current-voltage (I-V) operating point of the strings, modules, substrings and individual cells. Unmanned Aerial Vehicle (UAV) based TIR imaging is a method that is often used to conduct rapid in-situ PV plant inspections to locate underperforming hot cells. TIR imaging is cost-effective and non-destructive method carried out on large PV plants [16][98], unlike other testing methods. I-V measurements and EL testing methods are costly as they disrupt the production of electrical energy when being conducted. These techniques are carried out when the PV source under test is disconnected from the system circuit. This requires more time in disconnecting modules off the string and inverter, unlike TIR imaging which is conducted in situ. High-quality TIR images are captured under typical test conditions: a clear sky, calm airflow, with irradiance above 600 W.m^{-2} and the TIR camera positioned almost perpendicular to the module plane to avoid reflections [30][99]. Figure 2.16 shows the acceptable angles (green) for setting the TIR camera and the angles (red) which should be avoided, as recommended in the FLIR Systems Thermal Imaging guidebook [100] and also advised by Buerhop et al. [101].
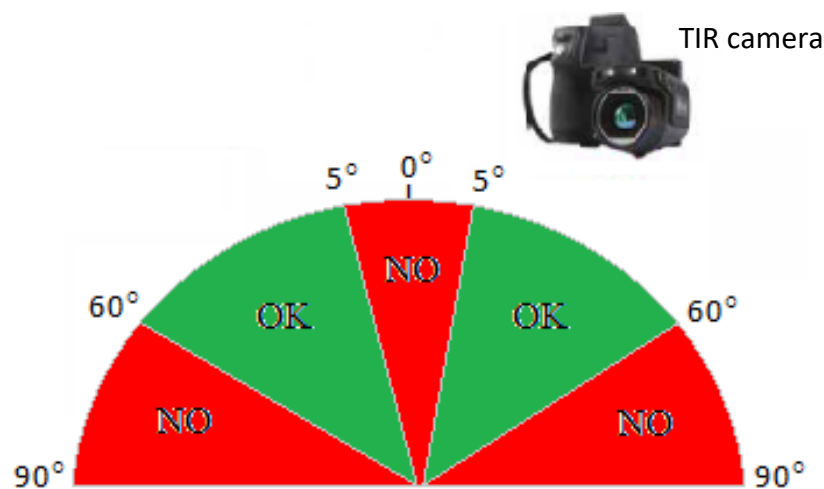
Figure 2.16: Recommended positioning of a TIR camera on capturing thermal images of PV modules (adapted from [100]).

31

One important parameter which can be derived from TIR images is the inhomogeneity in temperature between different parts of the module or between modules and/or strings of modules. Inactive areas of a module or string usually appear hotter than surrounding active areas because some of the radiation that is incident onto the operating PV module is converted to DC power, which flows to the loads. When a PV module or string is not functioning, this energy is not converted to DC power and therefore remains as excess heat, which raises the temperature of the module or string. Change in operational conditions can destabilise the temperature distribution in an operational PV module, therefore, thermal equilibrium should be considered in targeted PV modules since it can take up to 15 minutes for a typical PV module to thermally stabilize when there is a significant change in meteorological conditions [20].

Other important properties to take into account when carrying out TIR imaging of PV modules, apart from the angle of view which is illustrated in Figure 2.16 include sensor resolution, camera distance from a PV module. A camera with higher resolution allows the images to be captured at a further distance and thus capturing larger scale or greater number of modules on one image. To detect faults in an individual PV cell, the cell area in an image should be at least 3 to 5 times larger than an individual pixel. Thermal cameras can be radiometric, which means that each pixel has a temperature value. Without radiometric function, a thermal camera only shows the relative differences in temperature, and accurate measurement of temperature is not possible [102]. TIR cameras have a resolution limit that depends on the camera lens and distance of the target. In principle, TIR images taken at long distance involve unwanted variations of the atmospheric transmission and directional emissivity [103]. High resolution is important as it allows identification of smaller image detail, hence more accuracy. More pixels and data points per target area give high-resolution TIR images which are more accurate in thermal interpretation [20][98]. Detailed guidelines on the requirements for TIR cameras used for inspecting PV plants and the conditions for taking TIR images are highlighted in the technical specification IEC/TS 62446-3 [104].

Figure 2.17 shows non-uniform temperature distribution on TIR images due to shading caused by (a) neighbouring modules, (b) tall grass and (c) bird droppings.

	TIR image	Visual image
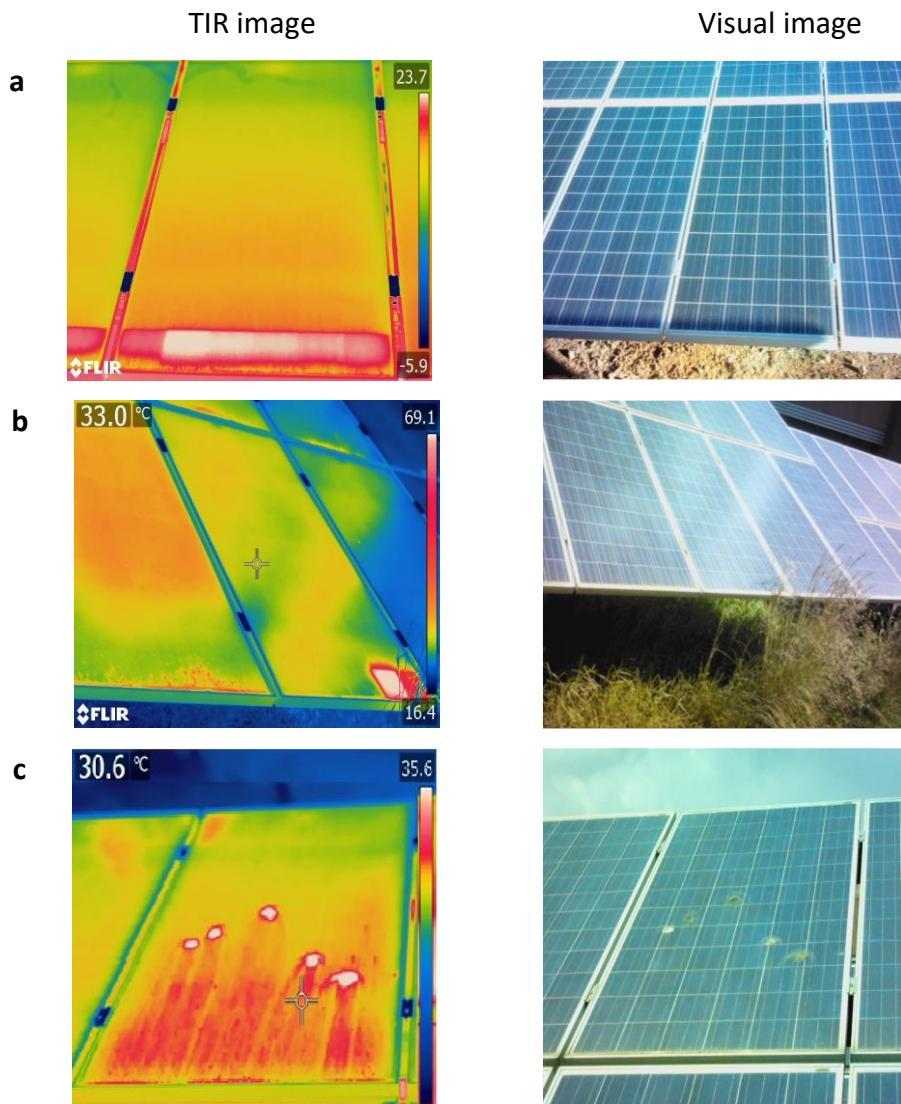
Figure 2.17: TIR and visual images of polycrystalline PV modules having non-uniform temperature distribution due to partial shading caused by (a) neighbouring modules, (b) grass and (c) bird droppings.

A significant area of a cell has to be shaded for the whole cell to appear hot, otherwise small hot spots appear due to different thermal emissivity [20][101]. The bird droppings in Figure 2.17 (c) are covering a small area and emit more radiation than the module glass, hence are seen as hot-spots on the TIR image. TIR images indicating patterns of thermal signatures on crystalline PV modules are classified in Section 2.6.5.2.

Hot cells can cause secondary abnormalities such as module glass cracks, back sheet damage and risk of fire. Figure 2.18 shows a TIR image of a crystalline silicon PV module operating in a string and having several hot cells. The substring, in the middle, is operating at elevated

temperature since a bypass diode paralleled to it is active and minimizing the current that passes through the substring, thus avoiding excessive heating on cell X. Some of the solar energy incidents on the substring is not converted to power but heats the cells.

Cell X heats up due to resistive heating caused by broken busbars and fingers.

Bypassed substring appears warmer than other substrings.
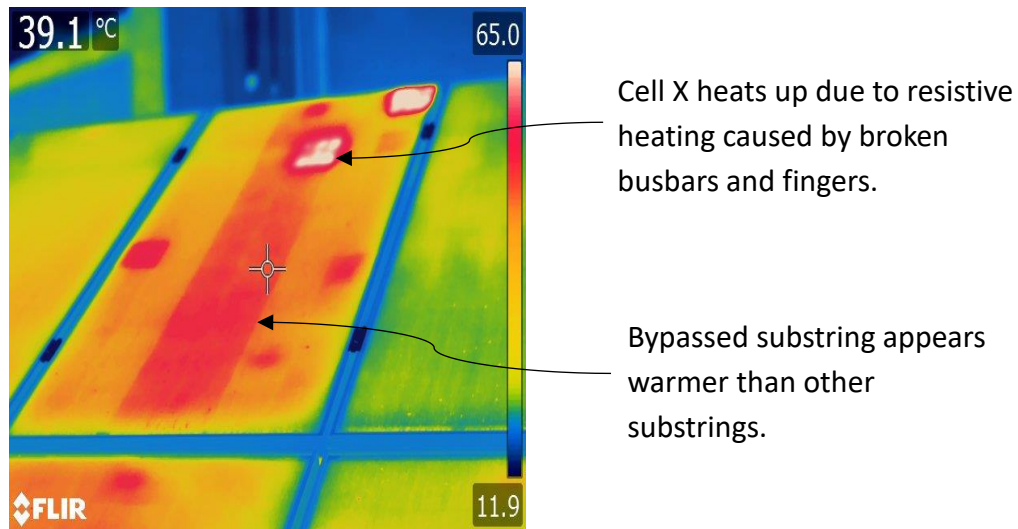
Figure 2.18: TIR image of a crystalline PV module with abnormally hot cell and substring.

If the module is not replaced, then the bypass diode paralleled to the affected substring will continue to conduct the string's current and will eventually get damaged. This scenario poses the risk of fire since a high potential difference (PD) can be created on cell X as the cell handles the huge electrical power of the string. If cell X has broken busbars, then the high PD created can cause arcs which can result in fire. According to A. Pandian et al [105], a defective cell can have an operational temperature of more than 300 °C, in the absence of bypass diodes, which can cause smouldering fire [20]. Figure 2.19 shows burnt marks due to overheated cells which resulted in (a) module glass cracks and discoloration on a cell and (b) back sheet damage along the busbars. Figure 2.19 (c) shows a damaged junction box due to excessive heating of the bypass diodes. Therefore, early detection of cell anomalies is crucial to avoid such defects which deteriorate power generation and are hazardous to PV facilities.

Module glass cracks and cell discolouration	back sheet damage	defective junction box
a	**b**	**c**

Figure 2.19: Visual images showing burnt marks due to excessive heating.

2.6.6.2 TIR image classification

TIR images can be classified into different categories depending on cell anomalies causing abnormal thermal signatures. When PV modules operate in the field, they are meant to receive equal solar energy to generate electrical energy at uniform temperatures. However, anomalies can occur in PV module operation which causes non-uniform temperature distribution in the module when series-connected cells are mismatched, as highlighted in Section 2.6.6.1. The temperature colour pattern of a PV module operating abnormally differs significantly from that of a good module and this forms the basis of the classification of different types of anomalies in this section. Table 2.1 describes different types of anomalies shown on TIR images and represented schematically.

Table 2.1: Classification of TIR images of crystalline PV modules, adapted from [16].

Class	Schematic Pattern	TIR image	Description	Possible anomaly
A			All cells at uniform normal temperature. Good module.	None.
B			Single cell at elevated abnormal operational temperature.	The cell is defective, shaded, soiled, PID affected, or of poor quality.
C			Cells at elevated temperature in one substring	Mismatched cells in a substring.
D			Cells at an elevated abnormal temperature in a patchwork pattern across all substrings.	Shattered module.
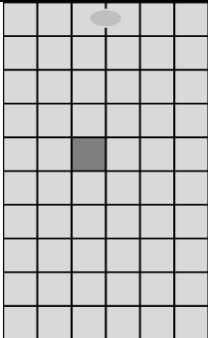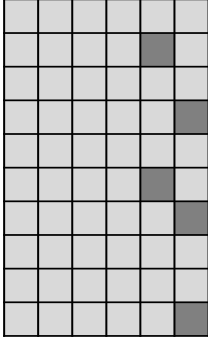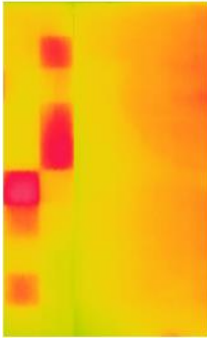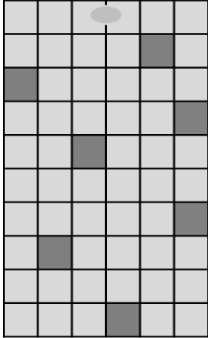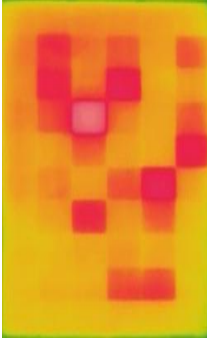
Table 2.1 (continued): Classification of TIR images of crystalline PV modules.

Class	Schematic Pattern	TIR image	Description	Possible anomaly
E			Cell point or part at elevated abnormal temperature.	Small defective cell parts or contaminants (soil, bird droppings).
F			Hot junction box.	Faulty connection in junction box. Overheated bypass diode/s.
G			Substring or block of cells at elevated abnormal temperature.	Mismatched substring. Bypassed substring.
H			Module at elevated abnormal temperature compared to rest of string.	Disconnected module (Module at open circuit conditions).
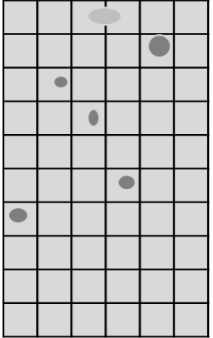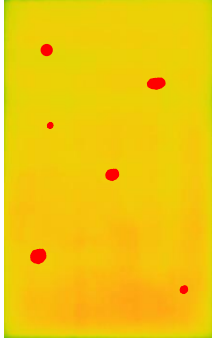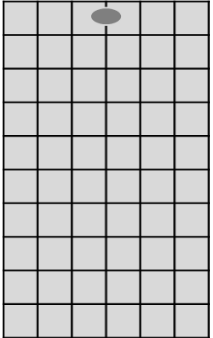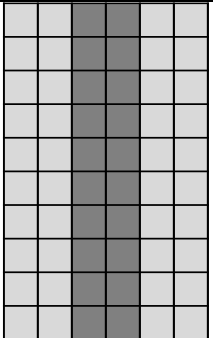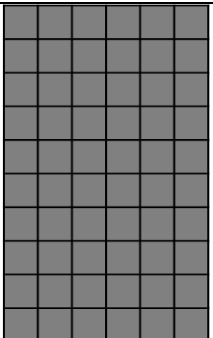
Usually, a defect-free module (A) has a uniform normal temperature distributed across its cells. Single-cell anomalies (B) are identifiable as a small rectangular structure exhibiting a thermal signature, covering the whole cell, that is significantly hotter than the rest of the module. Abnormally hot cells in a patchwork pattern can be viewed as an extension of single-cell defects as patchwork defects are given by multiple single-cell defects scattered randomly in a single substring (C) or all the substrings (D). Point cell defects (E) can occur when cell parts are disconnected from busbars and appear hotter than the rest of the cell. Thermal abnormalities on PV cells can occur externally due to several factors including sediment from the environment as well as bird excrement (E). When bypass diodes are active (F) for long, they appear hotter on TIR images. Substring defects (G) occur as multiple single-cell defects aligned along the substring and usually causes the substring to be hotter than normal substrings when the bypass diode paralleled to the affected substring is active. The whole module can be hotter (H) than the good ones when all the substrings in the module are abnormal. Additionally, the whole module can be abnormally hot when it is under open-circuit conditions and not delivering power as expected. The pattern of the thermal signatures on TIR images can reveal the possible anomaly on the PV module, however, so far, no international standard exists for the quantitative, but only qualitative, interpretation caused by the abnormal thermal signatures. Additionally, thermal patterns on the TIR images can be influenced under dynamic operational conditions, hence the need to investigate the behaviour of thermal and electrical characteristics of the modules, substrings and individual cells.

2.7 Summary

The doping of semiconductor materials improves their electrical properties. The PV action which occurs when photons fall on p-n junction and generate electrical power was discussed. Crystalline silicon PV cells are mostly used and instead of working individually, several cells are electrically linked in series to increase the output power, of a PV module, at the desired voltage. It was shown that the electrical characteristics of PV cells can be affected by several cell anomalies caused by the operational conditions. The anomalies can cause a mismatch in the operation of the cells which can influence the I-V parameters and homogeneous temperature distribution in a PV module. The bypass diodes are incorporated in crystalline PV modules to lessen the mismatch effects when they allow the module current to pass after

a forward bias voltage of about 0.35 V, for Scottky bypass diodes, is created on them. Cell anomalies can be identified through visual inspection and by taking I-V, EL and/or TIR characteristics of the PV source. UAV based TIR imaging is a quick method to locating underperforming cells in an operational PV plant. The TIR images can be classified according to anomalies causing the abnormal thermal signatures on crystalline PV modules.

Chapter 3

Experimental Details

3.1 Experimental facility, equipment and PV modules

The experimental data was acquired by carrying out TIR imaging on crystalline (mono and poly) silicon PV modules under different operational conditions and conducting other inspection methods such as visual inspection, EL imaging and I-V measurements, to ascertain any anomalies causing the observed abnormal thermal signatures. This was done to understand the behaviour of the thermal characteristics under dynamic operational conditions. Several experiments were conducted at the Outdoor Research Facility (ORF) that is situated at Nelson Mandela University (NMU), Eastern Cape Province, South Africa (34.0085°S, 25.6652°E). The experiments were conducted on arrays and individual PV modules which were ground-mounted and north-facing at the ORF. Some experiments involved the simultaneous recording of I-V and thermal characteristics, to have in-depth knowledge of the behaviour of cells under different operational conditions.

TIR images were captured using a TIR camera (FLIR-T620) while the I-V measurements of the operational modules were recorded using a data-logger, Agilent 34972A, that precisely monitors and records data through input channels [106]. The data-logger can be configured to directly measure DC voltage and current, among other quantities, at a specified interval time by channel scanning. Figure 3.1 shows the Agilent 34972A that was used for taking current and voltage measurements. The front side shows the controls and display for monitoring the measurements, while on the back of the logger are the connections for linking the channels to the PV module.

Figure 3.1: Agilent 3472A data logger.

The TIR camera (FLIR-T620) is a professional thermal imager that has Multi-Spectral Dynamic (MSX) imaging capabilities with high resolution and sensitivity for accurate temperature measurements [107]. The typical test conditions, such as angle of capture, calm environmental conditions, and emissivity settings, on the TIR camera, as highlighted in Section 2.6.6.1 were followed when TIR imaging was carried out on modules. Figure 3.2 shows (a) the FLIR-T620 TIR camera and (b) when the camera is mounted in position for imaging PV modules at the ORF.

a

FLIR-T620 TIR camera positioned for thermal imaging

Array of polycrystalline silicon modules

Laptop with FLIR tools and program connected to FLIR-T620 camera

b

Figure 3.2: (a) FLIR-T620 TIR camera used for taking TIR images. (b) Thermal imaging equipment set up for PV module inspection at the Outdoor Research Facility at Nelson Mandela University.

A Photovoltaic Engineering (PVE) I-V curve analyser was used for taking I-V curve characteristics of the modules and strings. Figure 3.3 shows the PVE PVPM1000X equipment set up for I-V measurements at the ORF. When taking measurements, the I-V trace points are obtained by sweeping the load, in the PVE analyser unit, on a PV source (module or array) over a range of currents and voltages. The PVE curve tracer accomplish this by loading the module or array, under test, at different points across its operating range between 0 V and

V_{OC}. At each point, the output current and voltage are measured simultaneously and displayed and stored to be exported for analysis [108].
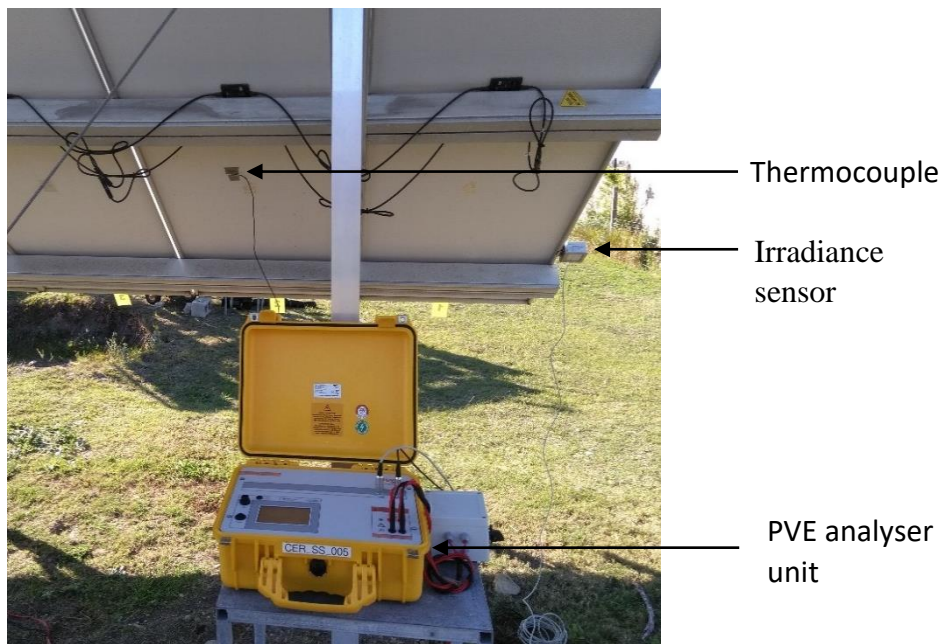
Figure 3.3: I-V curve tracer, PVE PVPM1000X, set up at ORF.

EL imaging for single modules was carried out using a third-generation Mobile Testing Laboratory, MBJ mobile-Lab 3.0, which uses a high-resolution electroluminescence test system to check for defects in solar cells. String EL images were recorded on-site, during the night using a Greateyes LumiSolar Outdoor EL system. Figure 3.4 shows (a) MBJ mobile-Lab 3.0 and (b) the Greateyes LumiSolar camera (GE 1024 1024 BI) which uses the Charge Coupled Device (CCD) sensors were used for EL measurements following the guidelines described in Section 2.6.5.

A PV module on a sliding door of the MBJ mobile Lab

a

EL Camera

Power unit

b

Figure 3.4: (a) MBJ mobile Lab and (b) Greateyes Lumisolar camera and power unit used for taking EL measurements.

Different PV modules, with and without major cell defects, were under investigation to study the dynamics of I-V operational points and abnormal thermal signatures in individual mono- and poly-crystalline modules and in arrays under different operational conditions. Table 3.1 lists the types of the PV modules used in this study and the specifications; short circuit current (I_{SC}), open-circuit voltage (V_{OC}) and rated current (I_{MP}), voltage (V_{MP}) and maximum power (P_{max}). Experimental procedures are described in the following sections of this chapter. TIR images of interest were analysed in FLIR Research Studio (FRS) and were correlated to EL

and I-V characteristics to understand the behaviour of the thermal signatures that were observed under different operational conditions. The FRS software is for research and science applications that allows displaying, recording and enhancing the TIR image in detail for easy analysis of the thermal data, including a profile plot of Region of Interest (ROI) [109].

Table 3.1: Performance parameters of the Photovoltaic modules under study.

Module	Module type	I_{SC} (A)	V_{OC} (V)	I_{MP} (A)	V_{MP} (V)	P_{max} (W)
A	SOLARWORLD SW-175 mono	5.3	44.4	4.9	35.8	175
B	ASTROPOWER AP-6105 mono	3.8	20.5	3.4	16.4	55
C	YINGLI-SOLAR YL250P-29b poly	8.92	37.6	8.39	29.8	250
D	SOLARWORLD SW 240 poly	8.44	37.2	7.96	30.2	240

3.2 TIR imaging of monocrystalline silicon PV modules under varying irradiance and output power

TIR imaging was carried out on a 1.6 kW monocrystalline silicon array containing nine PV modules (SW-175 mono), in-situ, at the ORF to understand the dynamics of thermal signatures under varying irradiance and output power. The 1.6 kW array under test consisted of three strings ST1, ST2 and ST3 in parallel, with each string containing three modules M1, M2 and M3 connected in series. Each module contains 72 cells in three substrings, SS1, SS2 and SS3, which are in a series connection and each substring has a bypass diode in parallel to it in the junction box. The layout of the array having nine monocrystalline silicon PV modules under study is shown in Figure 3.5.

45

Figure 3.5: Visual image of the monocrystalline silicon PV array at the Outdoor Research Facility (ORF).

To study the effect of mismatched cells on the temperature of modules during power curtailment and different irradiance, TIR images were captured when the array was producing power of 1100 W, 900 W, and 600 W. The varied output power was achieved by varying the load connected to the array and thus causing the array to operate at current and voltage operational points that are different to the maximum power point. The plane of array irradiance was closely monitored by the weather station at the ORF, NMU facility and was always above 600 W.m^{-2}. The I-V curve characteristics of the array, strings and individual modules were measured and corrected to standard testing conditions (STC), 1000 W.m^{-2} and 25 °C [66]. The air mass (AM), which depends mainly on environmental conditions such as temperature, humidity, dust and air pollution, is expected to be AM1.5 when taking the measurements [110][111]. The air mass was assumed to be constant, at AM1.5, since the measurements were taken under almost the same stable environmental conditions. EL images were taken after sunset, while each string was forward biased by a power source of the Greateyes LumiSolar system, which supplied voltage and current of 130 V and 5.8 A to the modules. The results that were obtained after the experimental procedure outlined in this section are discussed in Section 4.3.1.

3.3 TIR imaging of crystalline PV modules under partial soiling conditions

Figure 3.6 shows a 250 W polycrystalline silicon PV module (YL250P-29b poly, Module C), containing sixty series-connected cells in three substrings. The module was inclined on a support for TIR imaging and I-V measurements while receiving an irradiance of approximately 1000 W.m^{-2}. The effects of dynamic soiling, as experienced in the field, were simulated by partial (<10%) shading one cell in each substring sequentially while taking TIR images and I-V measurements of the module. This was done to see the effects of soiled substrings on the observed hot cells and I-V parameters.

Partially soiled cells
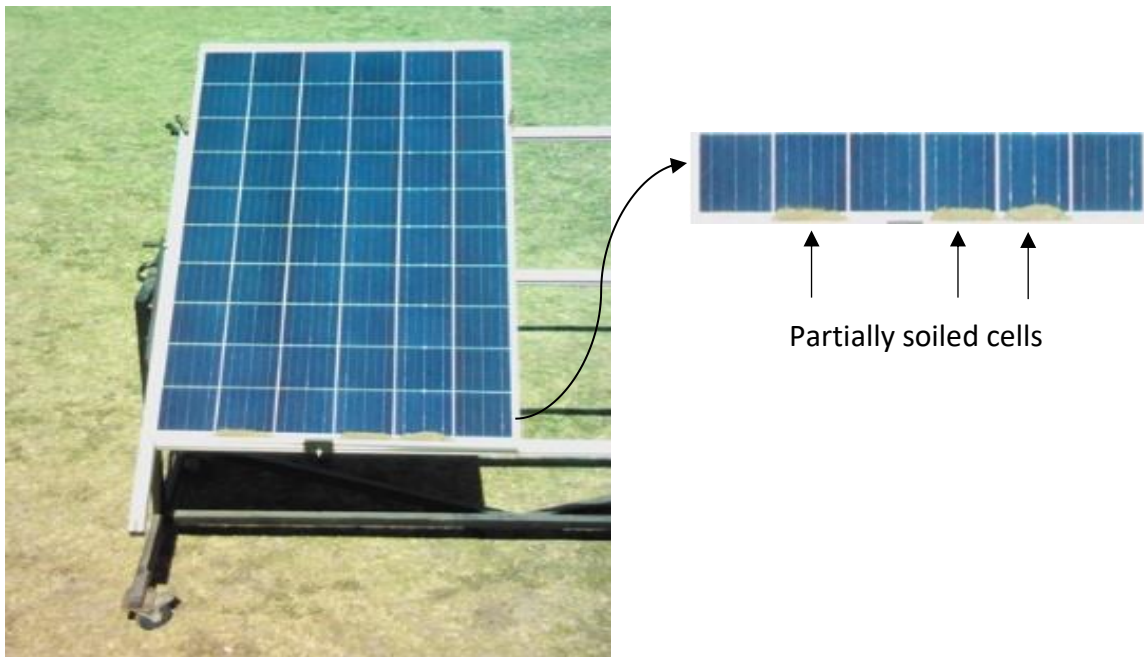
Figure 3.6: Soiled polycrystalline silicon PV module inclined for TIR and I-V curve measurements.

After soiling each cell, a thermal equilibrium period of about 15 minutes [20] was considered before capturing the TIR images using the TIR camera (FLIR-T620) that was positioned at about 4 metres above the short-circuited module. The capturing angle was approximately normal to the targeted module's front surface as generally recommended [16][100]. The I-V measurements were taken using the PVE I-V analyser and were corrected to STC, irradiance and temperature of 1000 W.m^{-2} and 25 °C, respectively. EL imaging was conducted using the MBJ mobile-Lab 3.0 to further inspect for cell damages that could not be visually detected. The obtained TIR images were analysed using the FLIR Research Studio (FRS) and correlated to the I-V measurements and EL images of the module. Artificial partial soiling was also

applied on a large scale of the 1.6 kW array containing nine monocrystalline silicon modules shown in Figure 3.5 to simulate the effect of partial soiling on the hot cells observed in one of the modules. The results on partial soiling of the module and array are discussed in Sections 4.2.1 and 4.3.2, respectively.

3.4 TIR imaging of a monocrystalline PV module under varying load

TIR imaging was conducted on a monocrystalline silicon PV module (AP-6105 mono, Module B) containing 36 series-connected cells in two substrings. The module was inclined on a support and received irradiance of approximately 1000 W.m^{-2}. The setup is shown in Figure 3.7.
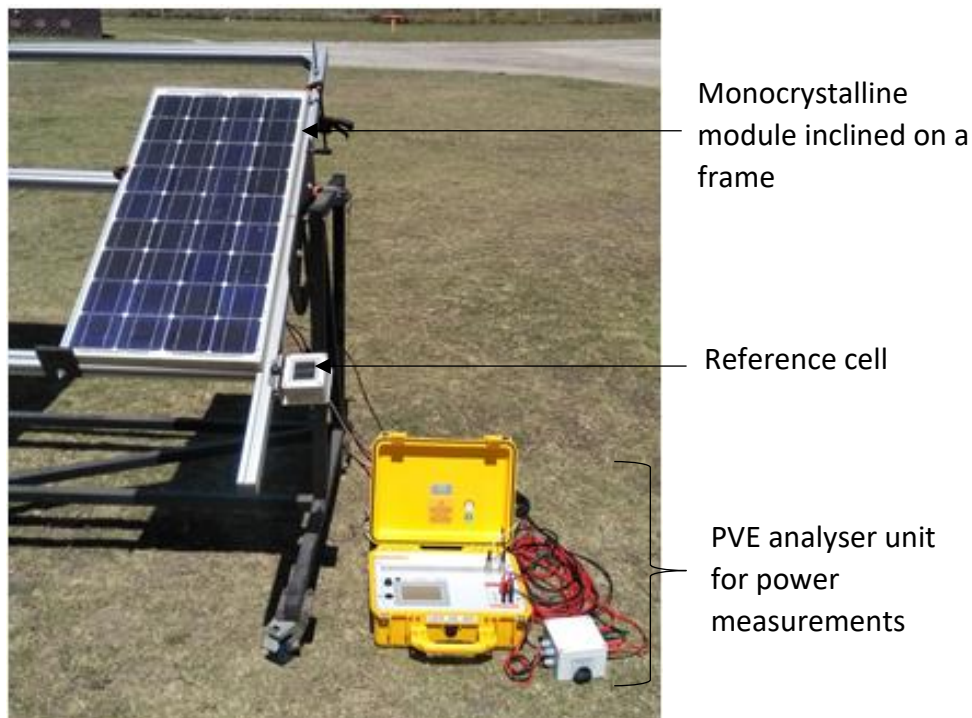
Figure 3.7: Monocrystalline silicon PV module set up for power and TIR measurements on varying load.

The TIR camera (FLIR-T620) was positioned at approximately 4 metres above the module's front surface with the capturing angle approximately 10° to the plane's normal [30]. TIR images were captured when the module was generating current equivalent to I_{SC}, 40%, 50%, 70%, 85% of the I_{SC} and under open circuit conditions to observe the behaviour of thermal signatures on varying I-V operational points. Different module generated currents were achieved by changing the operational load conditions of the fixed resistor, viz. 0.0%, 33.3%,

66.7%, 83.3% and 100.0%. A period of about 15 minutes was allowed for the modules to reach thermal equilibrium before the TIR images were captured as recommended by Jahn U. et al [20]. The generated current and voltage of the PV module were measured for each load. To have a better understanding of the dynamics of abnormal thermal signatures in the module, inspection techniques such as visual inspection, I–V measurements (of the module and two substrings), and EL imaging were applied to the PV module. The I-V curve characteristics of the module were measured using the PVE I-V curve tracer and EL imaging was conducted when the module was in the dark, using the MBJ mobile-Lab 3.0 to locate cell damage and micro-cracks which could not be visually identified. The results are presented in Section 4.3.3.

3.5 Performance monitoring of individual cells under dynamic operational conditions

To have in-depth knowledge on the behaviour of series-connected cells in substrings, thermal and voltage characteristics of individual cells were monitored when a polycrystalline silicon PV module (SW 240 poly, Module D) was operating under varying load, irradiance and shading conditions. The current of the module and one substring (SS3) were concurrently measured, while recording the thermal images, and a 0.01 ohm (Ω) resistor was used as a current transducer. Figure 3.8 shows the experimental set-up for measuring the operational electrical and thermal characteristics of individual cells in the polycrystalline silicon PV module. The figure shows the backside of the module with the electrical connections on each of the 60 cells and linked to the data logger (Agilent 34972A) that has a measurement sensitivity of approximately 1 μV [106]. The data logger was programmed to continuously measure the actual operational current and voltage values of the cells at intervals of 5 seconds (s) when the module was delivering electrical power to the load. The I-V measurements of individual cells were recorded concurrently with TIR images of the module under changing shading and varying load conditions. Different sizes of the opaque shading material were accurately cut and placed, one at a time, on the front side of the cell to shade a definite area, 4 to 100%, of the cell while recording the measurements.
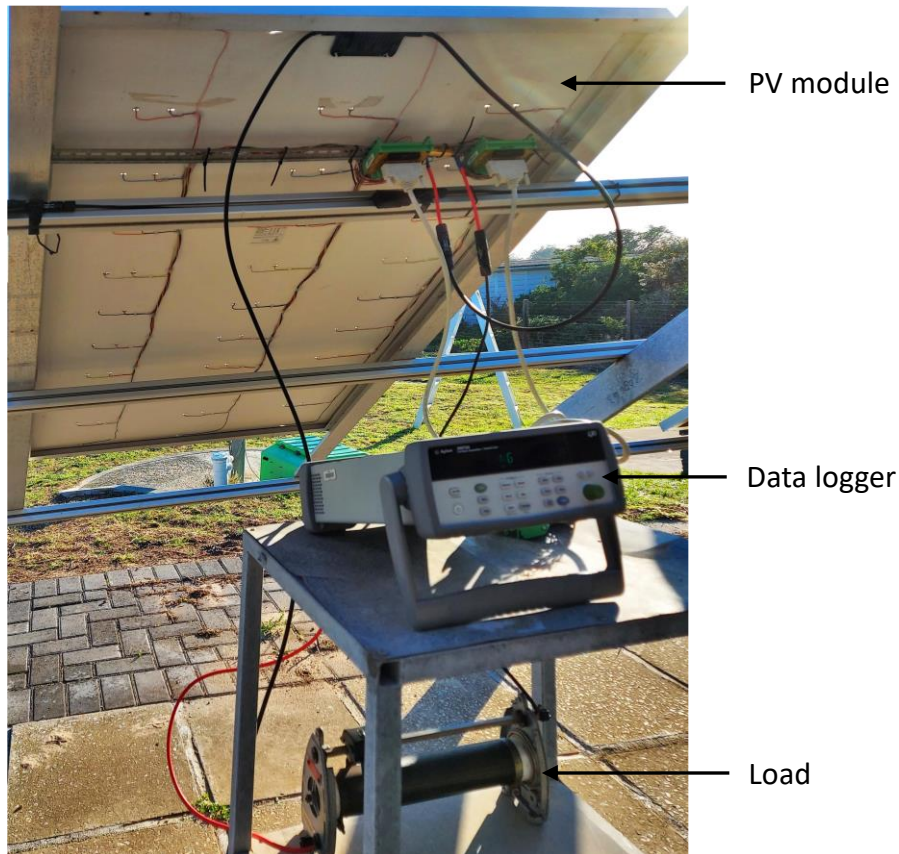
Figure 3.8: Experimental set-up for monitoring I-V and Thermal characteristics of individual cells in a polycrystalline PV module.

The measurements were recorded when shading was varied from 0 to 100% on one cell (cell 51) while the module was receiving an irradiance of > 700 W.m^{-2} and applying a voltage of 28 V, to the load. TIR images of the module were simultaneously recorded, with the electrical characteristics, to observe the operational temperature to the current and voltage values of the cells under different shading levels. The TIR camera (FLIR-T620) was positioned following the guidelines for capturing TIR images as highlighted in the International Energy Agency report [20] and the FLIR user's manual [100]. Figure 3.9 shows a visual image of the p-Si PV module with the cells numbered sequentially through the substrings, SS1, SS2 and SS3, from top left to top right. The figure shows a shading level of 60% on cell 51 in substring SS3. The I-V curve characteristics of the module were measured to observe the effect of the shading levels, 0 to 100%, on the representative I-V parameters of the module. EL images of the module were taken, before and after connecting the cells to the logger, to check for any pre-existing cell anomalies causing an inherent cell mismatch. A High current EL (high EL) image was obtained when a current of 8.44 A (I$_{SC}$) was applied to the module, while a low

current EL (low EL) image was recorded when the module was forward biased with a current of 10% of I_{SC}. The electrical connections at the back side of the module did not cause cracks on the cells, since the EL images that were taken before and after making the electrical connections looked the same. The EL image of the module is shown in Figure 4.8. The results that were obtained following this experimental procedure are discussed in Section 4.2.3.
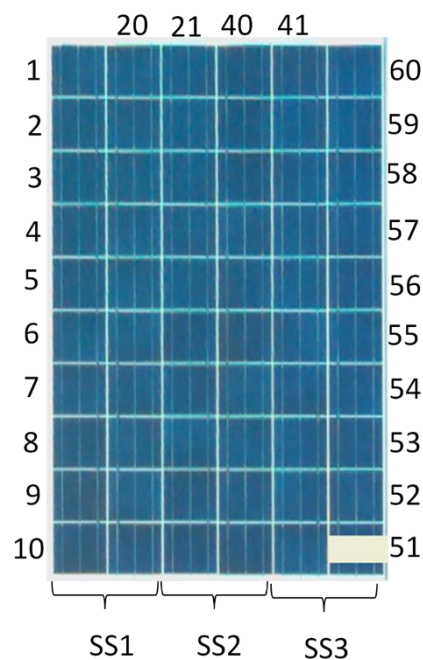
Figure 3.9: Visual image of a polycrystalline PV module with cells numbered from top left to top right and having 60% shading applied on cell 51.

The current and voltage and thermal characteristics were also measured when the module was generating power at different operational voltages, 0 V through V_{MPP} to V_{OC}, which were achieved by adjusting the load and the results are presented in Section 4.3.4.

The TIR imaging test was repeated under a constant load (fixed resistor) while operating throughout the day under varying irradiance levels with and without partial shading on one of the cells, and the results are discussed in Section 4.3.2. Figure 3.10 shows the front surface of the module with partial shading of ~5% that was applied on cell 10 in substring SS1 when TIR images were recorded. Partial shading is when a portion area of the cell is blocked from the incident sunlight. The shading level on the cell was achieved by placing an opaque shading material, cardboard, that was accurately cut to shade the required cell area. Thus a 5% shading level will only shade 5% of the cell area.
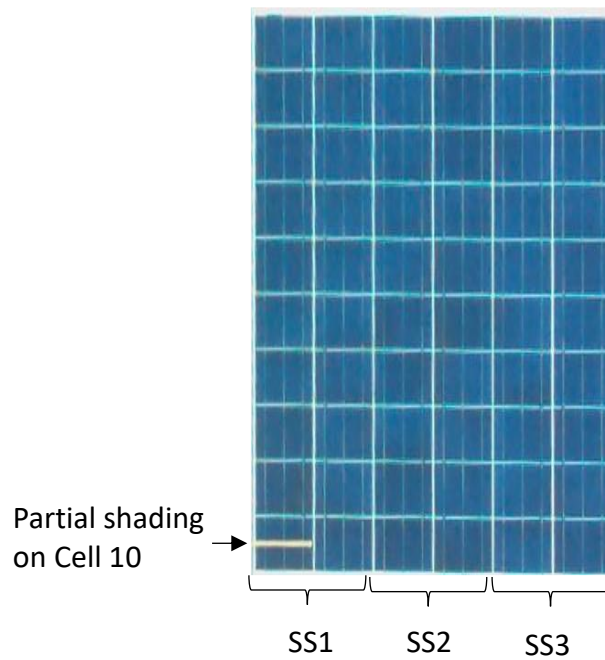
Figure 3.10: Polycrystalline silicon PV module with partial shading (~5%) on cell 10.

The data acquired were analysed to understand the behaviour of cells and modules under dynamic operational conditions. The temperature profiles of cells of interest on selected TIR images were analysed in FLIR Research Studio (FRS) to see the dynamic operational temperature of the cells under different conditions.

3.6 Summary

The equipment and the experimental procedures for the study were presented in this Chapter. TIR imaging was conducted on a 1.6 kW array containing nine monocrystalline silicon PV modules which were operating under varying irradiance and output power and on individual crystalline (mono and poly) PV modules that were delivering electrical power under varying load and changing soiling conditions, respectively. The operational current of the module and substring, and voltage measurements of individual cells of polycrystalline silicon PV modules were recorded simultaneously with TIR images when one cell was under different shading levels of 0 to 100%. TIR images of the polycrystalline silicon PV module were also recorded under constant load resistor and changing irradiance, morning, afternoon and evening, with a shading level of ~5% on one cell. EL imaging was carried out to check for cell defects that could not be visually identified. FLIR Research Studio was used to analyse the TIR images. The data obtained using the experimental procedures are discussed in Chapter 4.

Chapter 4

Results and Discussions

4.1 Introduction

This Chapter discusses the results obtained following the experimental procedures outlined in Chapter 3. Sections 4.2 and 4.3 discuss the dynamics of abnormal thermal signatures due to a change in operational conditions of the crystalline (mono and poly) PV modules. The effects of changing load and shading conditions, that are representative of real-world conditions and was described in Chapters 2 and 3, as well as varying irradiance and output power on the operational behaviour of PV cells, substrings and modules are being discussed.

4.2 Effects of partial cell shading on operational I-V and thermal characteristics of crystalline PV modules

4.2.1 Effects of partial soiling on I-V parameters and TIR images of a polycrystalline PV module.

This section presents and discusses the dynamics of I-V and thermal characteristics of a polycrystalline silicon Module C (YL250P-29b poly) under different soiling conditions, after carrying out the experiment described in Section 3.3. The specifications of Module C are shown in Table 3.1 in Section 3.1.

Figure 4.1 shows TIR images captured when the polycrystalline silicon PV module (YL250P-29b poly) was operating under short circuit conditions with unsoiled cells, Figure 4.1(a), and with partially soiled cells, Figure 4.1(b) – (d), in different substrings. The figure also shows visual images of only the bottom rows of cells of the module, which are enlarged so that small partial soiling on the cells can be seen. The TIR images are: (a) unsoiled cells, (b) one soiled cell, (c) two soiled cells, and (d) three soiled cells. Also shown in the figure are line scans through regions of interest (ROIs) for temperature line profile analysis
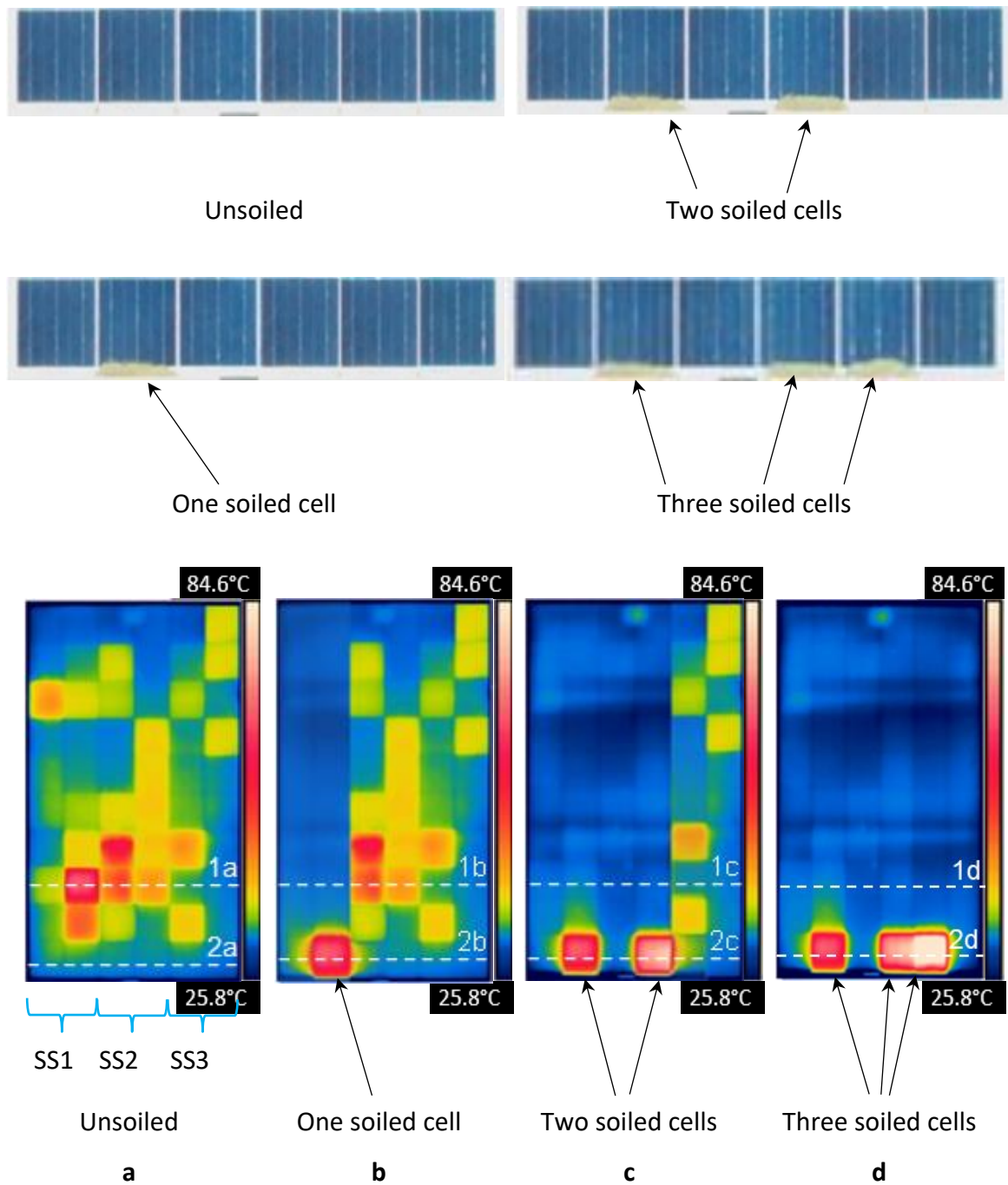
Figure 4.1: Thermal images of the p-Si PV module captured in a short-circuit condition with different soiling conditions with the module having (a) unsoiled cells, (b) one soiled cell, (c) two soiled cells, (d) three soiled cells. ROIs, 1a - d and 2a - d, are shown on the TIR images for temperature line profile analysis. The enlarged visual images show the soiling conditions on the cells.

Figure 4.1, (a) shows the non-uniform temperature distribution in the module causing several abnormally hot cells in a patchwork pattern in substrings SS1, SS2 and SS3. The non-uniform temperature distribution in the module is due to a current mismatch between good and bad

cells in the module. The bad cells are operating in reverse bias and heat up as they dissipate electrical energy generated by good cells.

When a good cell at the bottom row of the module in substring SS1 is shaded by partially (≤ 10%) soiling, it heats up and operates at an abnormal temperature while the rest of the substring operates at a uniform temperature, as shown in Figure 4.1(b). The hot cells in substring SS2 and SS3 are still visible in the TIR image but the TIR signature of the bad cells in substring SS1 disappears. When one good cell in substring SS2 is similarly shaded in the bottom row, the TIR image in Figure 4.1(c) shows that the cell is reverse biased and heats up, and the hot cells previously seen in the substring disappear and only the hot cells in the unsoiled substring SS3 remain visible. When three good cells at the bottom of each substring are shaded, as indicated in the TIR image Figure 4.1(d), these cells appear hot and all the other cells in the module appear to have a uniform temperature despite the anomalies highlighted on the TIR image in Figure 4.1(a). Partial soiling caused non-uniform illumination on the soiled cells and resulted in the soiled cells operating in reverse bias and dissipating electrical energy generated by good cells as heat. Thus, minimising the current generated by the crystalline cells in the substrings and resulting in the operational temperature of the cells being affected. In a real PV plant situation, the TIR image shown in Figure 4.1(d) will only lead to a decision of cleaning the soiled module since other anomalies are not revealed.

The effect of partial soiling on the operational temperature of the cells is revealed by line profile analysis of the regions of interest (ROIs) 1a – d and 2a - d on TIR images in Figure 4.1. The line profiles which were generated in FLIR Research Studio (FRS) are plotted in Figure 4.2. Figure 4.2(a) and (b) show the temperature distribution across the length of each ROI, in pixel scale, 1a – d and 2a – d, respectively. Line profile LP 1a reflects temperature fluctuation on thermal signatures across bad cells on ROI 1a while LP 2a represents homogeneous temperature distribution of ROI 2a with good cells. The effect of dynamic partial soiling on the operational temperature of the cells on the ROIs 1b – d and 2b – d is shown by line profiles LP 1b – d and 2b – d, respectively. The soiled cells operated at around 60 °C with the soiled cell in substring SS3 having the highest operating temperature of about 64 °C probably due to a slightly more shaded part than the soiled cells in substrings SS1 and SS2.
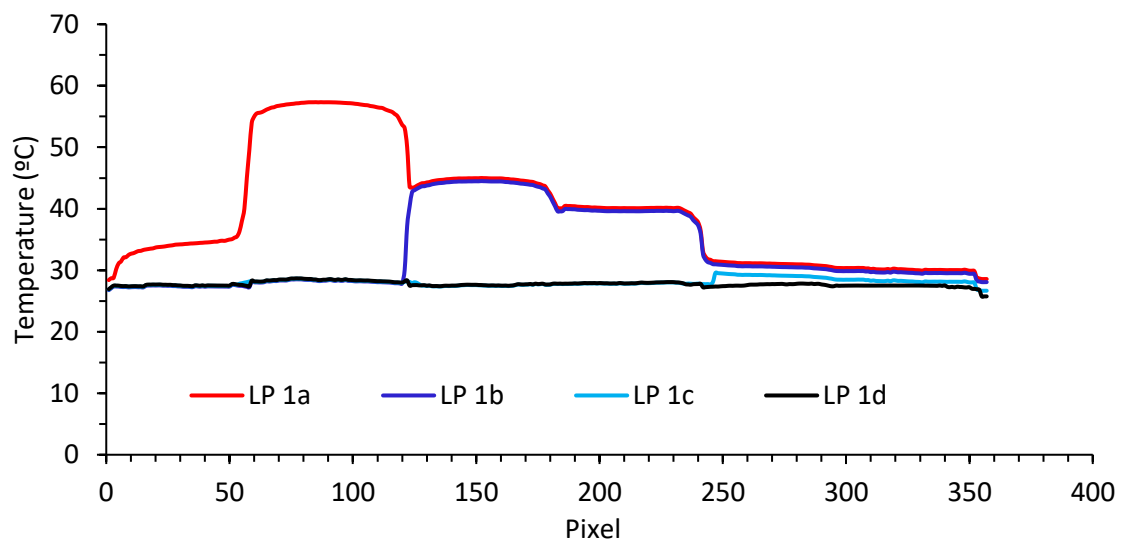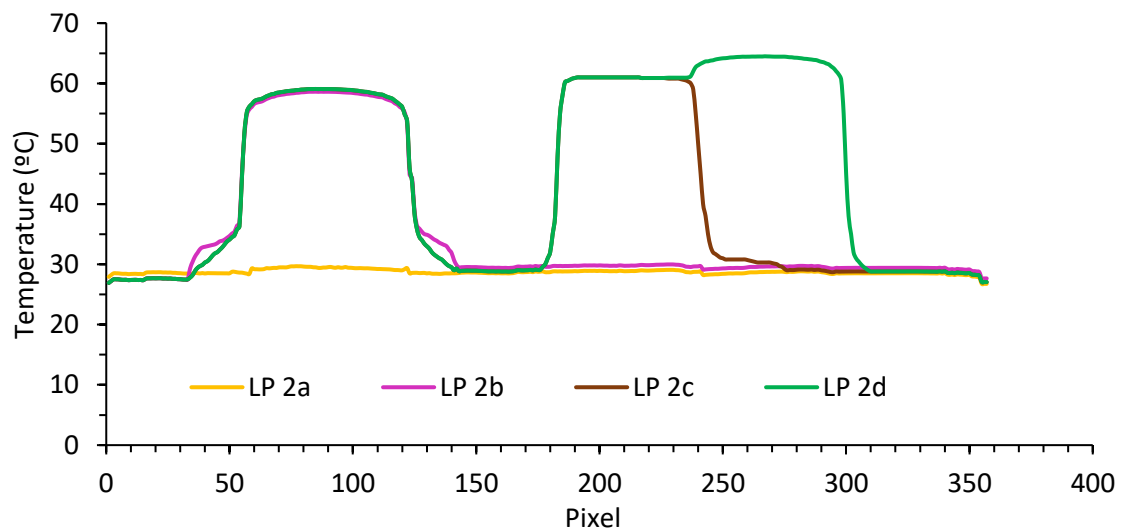
Figure 4.2: Line profiles of Regions of Interests (ROIs), (a) 1a – d and (b) 2a – d, showing dynamics of the operational temperature of bad and good cells when partial soiling was applied on three cells.

Figure 4.3 shows the effect of partially soiled cells on the I-V curves of the p-Si PV module. The I-V curve of the unsoiled module deviated from the expected (reference) I-V curve which was generated in PVSim [64], and shows no clear activated bypass diode steps due to an insignificant current mismatch between the substrings. The steps in the I-V curves when one and two cells were soiled reveal active bypass diodes across the affected substrings. The bypass diodes conduct current and bypass substrings SS1 and SS2 to lessen the heating effect

on the soiled cells in these substrings. However, when three cells, one in each substring, were partially soiled, the substrings become matched and generated equal currents of ~8.1 A. This resulted in a drop of 0.7 A in the module's I_{SC} (~8.8 A) with no bypass diode active, but while soiled cells remained abnormally hot.
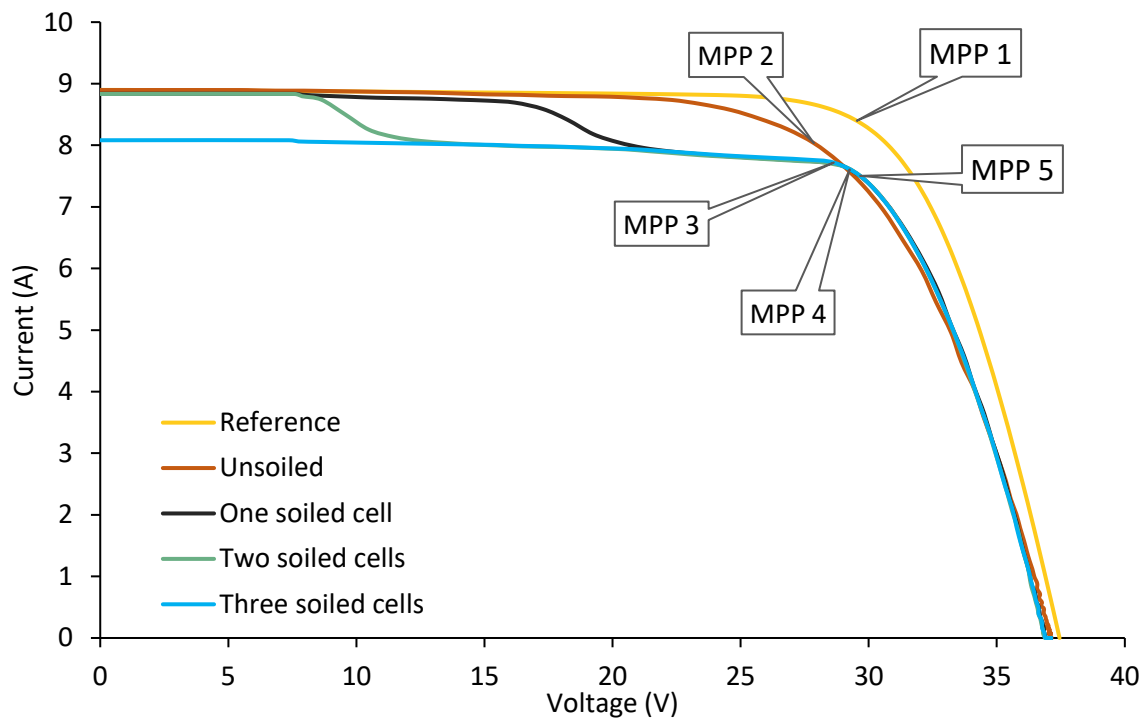
Figure 4.3: I-V characteristics of the polycrystalline silicon module under different soiling conditions. The reference I-V curve created in PVSIM is shown.

The cell anomalies and partial soiling forced the maximum power point (MPP) to be at a different operational voltage, as shown by MPPs 1 – 5 in Figure 4.3 and resulted in the reduction of the module's generated power as shown in Table 4.1. Considering the power uncertainty in Table 4.1, there is a significant difference between the P_{MPP} of the reference (original specifications) and the unsoiled I-V curves due to the bad cells that are shown on EL image in Figure 4.5(b). An additional, but insignificant drop in power, is realised with one, two and three soiled cells. The partial soiling on the cells mainly affected the module's MPP.

Table 4.1: Performance parameters of the module.

I-V curve	MPP number	V_{MPP} (V) ±0.9%	I_{MPP} (A) ±2.8%	P_{MPP} (W) ±4.8%
Reference	1	29.3	8.4	246
Unsoiled	2	27.9	8.1	226
One soiled cell	3	28.8	7.8	225
Two soiled cells	4	29.0	7.7	223
Three soiled cells	5	29.5	7.5	221

The I-V parameters of the module were modelled in PVSim when the module was assumed to operate under unsoiled conditions, and when the substrings were generating less current due to the underperforming cells. Figure 4.4 shows the I-V curves obtained after the simulations. The I-V curves of the normal module, one, two and three underperforming substrings in Figure 4.4 are similar to the I-V curves unsoiled, one soiled cell, two soiled cells and three soiled cells, respectively which are shown in Figure 4.3. Thus, the soiling scenarios which influence the MPP and shift the bump towards I_{SC}, due to the number of activated bypass diodes, can be modelled in PVSim. Similar results were also discussed in other publications [18][112].
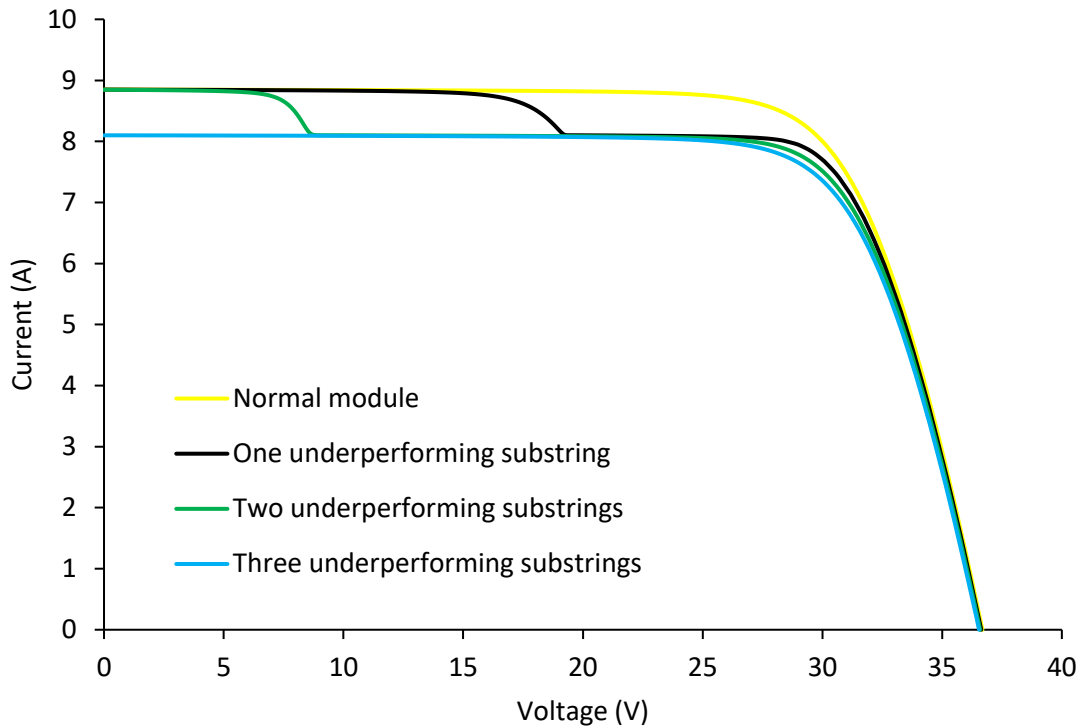
Figure 4.4: I-V curves modelled in PVSim and simulating different soiling scenarios on the polycrystalline module.

In a real PV power plant situation, the shift in the MPP of a module string can impact the efficiency of the PV system as the MPP trackers in inverters continuously track the MPP for optimum delivery of electrical energy to the load. Although the I-V parameters and TIR imaging can reveal some information regarding the operation and performance of the cells and modules, the actual cause of the thermal signatures in Figure 4.1(a) was only revealed through EL imaging and is shown in Figure 4.5.

The EL image of the module, Figure 4.5(b), shows that some hot cells in Figure 4.5(a) correspond to damaged cells in substrings SS1 and SS2 and other hot cells (uncracked cells) were possibly due to PID affected or poor-quality cells. The affected cells are coded according to the type of anomaly in Figure 4.5(c). These defects could not be identified in a visual inspection. The affected cells operated normally when the module was soiled, therefore in-depth knowledge on the state of the cells can be obtained by incorporating EL imaging.
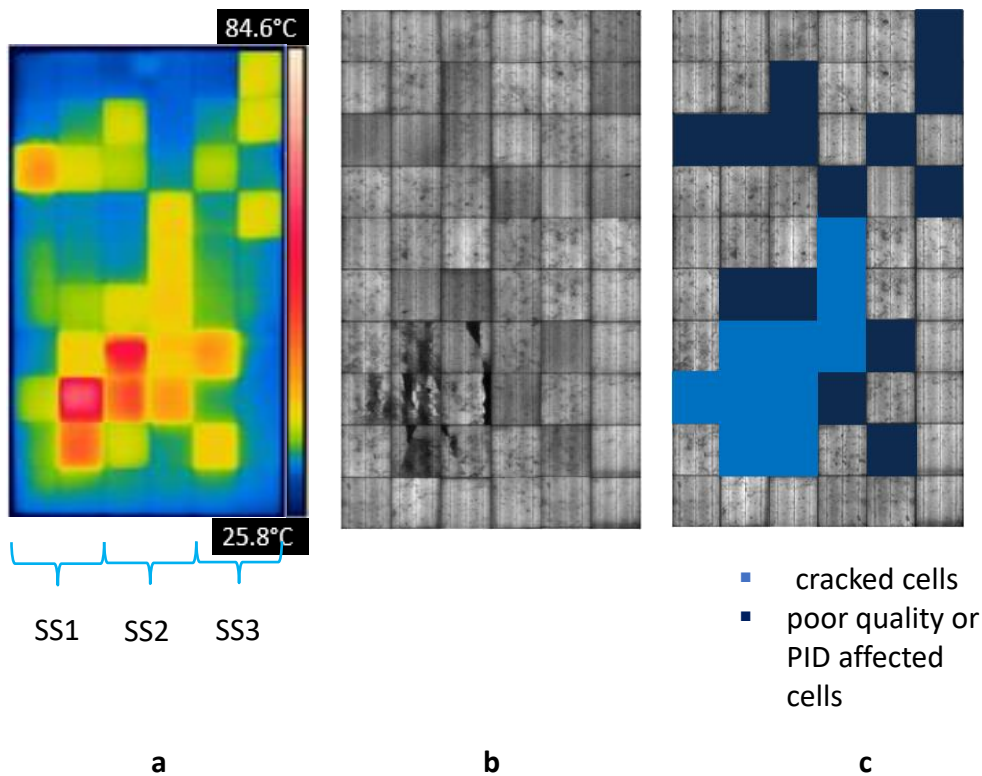
Figure 4.5: (a) TIR and (b) EL images of the polycrystalline silicon PV module. (c) EL image of the module with classified cell anomalies.

Abnormalities in crystalline solar cells which cause reverse biasing when operating in a series connected string can result in significant current mismatch and resistive heating. Incorporation of other testing techniques such as EL imaging, I-V measurements and visual inspection may give additional information on the state and performance of the PV modules so that informed decisions can be made during PV module inspections to avoid poor performance, accelerated module degradation and safety hazards.

4.2.2 Dynamics of hot cells on a large scale (array) due to partial soiling on a cell

The dynamics of thermal signatures due to partial shading, as observed in Section 4.3.1, can be seen on one of the nine monocrystalline modules in the 1.6 kW array (discussed in Section 4.3.1) was partially soiled. The results in this section were obtained following an experiment that is described in the last part of Section 3.3. The specifications of the modules (SW-175 mono, Module A) are given in Table 3.1 (Section 3.1). Figure 4.6 shows the effect of partial soiling on the thermal signatures in substring ST3-M2-SS3, which were detected when the array was unsoiled, Figure 4.6(a). The TIR image in Figure 4.6(b) was taken when the plane

of the array was receiving high irradiance of 1 sun (1000 W.m^{-2}) and with one good cell in the substring, ST3-M2-SS3, partially soiled (≤ 10%).
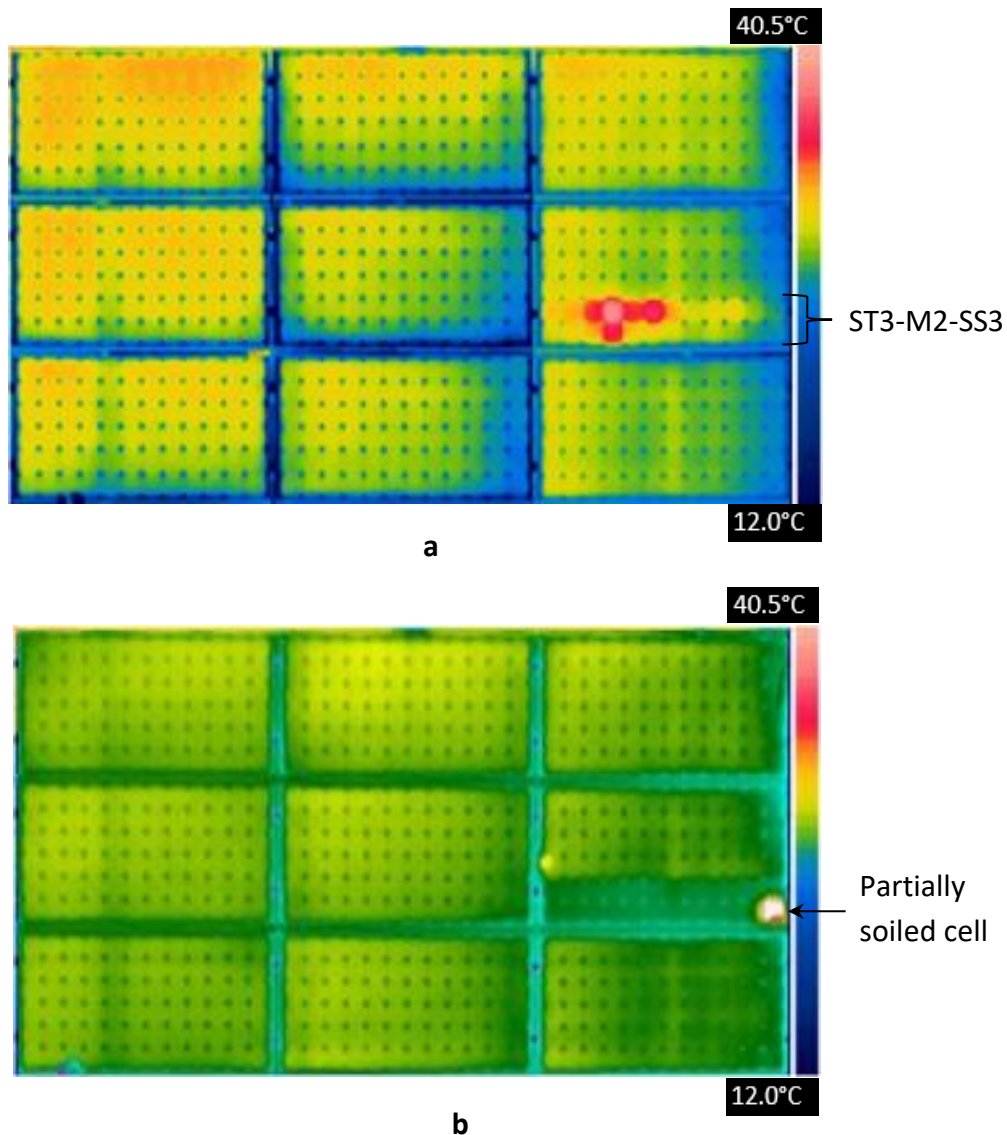
Figure 4.6: Thermal images of the 1.6 kW array under 1 sun and output power of 1100 W, (a) unsoiled and (b) with a partially soiled cell.

The soiled cell heats up and operates at an abnormal temperature while the rest of the cells in the substring, ST3-M2-SS3, operate at a uniform temperature. The whole-cell is abnormally hot mainly due to current mismatch and resistive heating when the cell was partially shaded and operating in reverse bias. It is unlikely that the heating is caused by the different thermal emissivity of the module glass and soiling. Differences in thermal emissivity of the module glass and soiling can cause only the contaminated part of the cell to be at an elevated temperature as the unsoiled part [113]. The scenario where only the shading material gets

61

abnormally hot, is discussed in Sections 4.2.3 and 4.3.2. Partial soiling caused non-uniform illumination on the soiled cell which forced the soiled cell to operate in reverse bias and dissipate the substring's electrical energy as heat, thus minimising the current generated by the substring. This lower current reduced the level of current mismatch in the bad cells and resulted in the cells not showing their abnormal thermal signature as seen in the original TIR image Figure 4.6(a). A smaller current mismatch causes the operational temperature of bad cells to be low enough such that they appear as good cells on TIR images. Partial soiling, therefore, influences the tolerable current mismatch in operational crystalline modules and thus affects the results on TIR images. A TIR image that indicates only soiling mismatch can thus be misinterpreted since other anomalies are hidden. Mismatch caused by soiling or shading can be a dynamic phenomenon thus, causing TIR images to show features that are dynamic in nature. This array is discussed further in Section 4.3.1 where the effects of the defects associated with the substring ST3-M2-SS3 on I-V characteristics and EL image of the string containing the module are investigated.

Other studies on this topic, [114-118] confirmed that shading on PV modules can cause abnormal thermal signatures which impact on performance. However, this study further shows that partial soiling affects the non-uniform temperature distribution in the soiled module, such that the bad or cracked cells cannot show their abnormal signature on TIR images. Therefore, not only cleaning the modules will help for effective judgement of the TIR images, but also incorporating other inspection methods such as EL imaging. It is also important to note the conditions under which the TIR images are taken since different operational conditions such as change in irradiance and load conditions influence the TIR images, as discussed in the following Sections.

4.2.3 Effects of partial cell shading on electrical and thermal characteristics of polycrystalline silicon cells, substrings and module and associated power

To acquire an in-depth knowledge on the behaviour of cells under partial shading, the performance characteristics of the polycrystalline silicon PV module (SW 240 poly) and individual cells were monitored and recorded under different levels of cell shading following the experimental description in Section 3.5. The manufacturer's performance parameters of the module (SW 240 poly, Module D) are indicated in Table 3.1 in Section 3.1. Thermal images of the cells were recorded concurrently with voltage and current measurements of the cells,

substring and the module as described in Section 3.5. The numbering of the cells in the module is indicated in Figure 3.5. The current generated by the module and a substring, SS3, and voltages of the individual cells were recorded when the module was unshaded and connected to a constant resistive load. Figure 4.7 shows the current and voltage measurements when the module was operating under steady environmental conditions: low wind velocity, constant ambient temperature and clear sky with an irradiance of > 700 W.m^{-2} incidents on the cells. The graphs show that the generated currents and the individual cell voltages varied with prevailing meteorological conditions. The differences in the generated currents, of the module and substring, SS3, and individual cell voltages show evidence of mismatch and variations in the power generated by each cell. The module's current is 0.1 A (1.5%) more than the substring's generated current. The voltage difference between the highest and lowest cell voltages, cells 58 and 21 respectively, is almost 0.024 V, thus a ~4% difference in cell-cell voltage. Figure 4.7 also shows that none of the cells is operating in reverse bias.
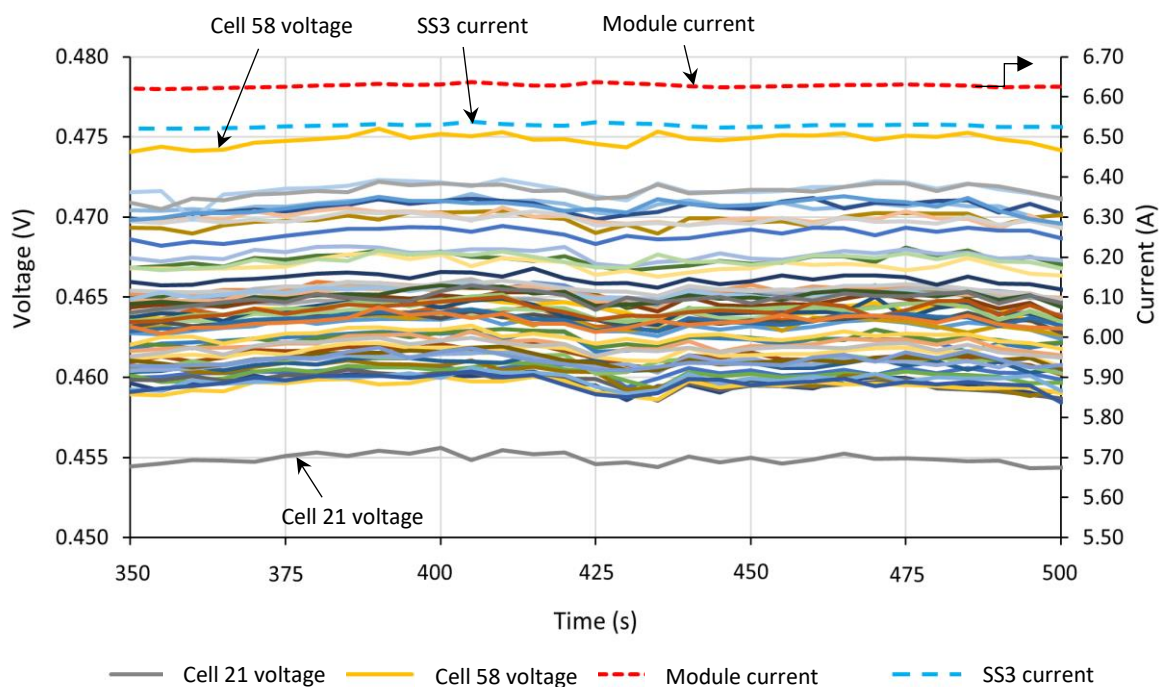
Figure 4.7: Mismatch in cell voltages recorded under steady conditions. The solid lines show the voltages of the cells. The red and blue broken lines represent currents produced by the module and substring 3 (SS3), respectively.

To investigate if any pre-existing cracks or Potential Induced Degradation (PID) are present in the cells that may impact the overall performance of the module, Electroluminescence (EL) imaging of the module was performed. A module having PID stressed cells will show a checkerboard pattern of black/dark and white cells. The black or dark cells can be observed mostly on EL images taken at a current corresponding to 10% of I_{SC} and can appear on the edge regions close to the module frame [16][20][119]. Figure 4.8 shows EL images of the module taken at (a) 110% (High current EL image) and (b) 10% (Low current EL image) of the I_{SC}. There are minor cracks on the highlighted cells, 1, 20, 47 and 52 which run diagonally across the cell but did not impact the performance of the module since all the fingers are connected to the busbars, thus no cell part is isolated as none of the cells appear dark. Cells 1, 20, 47 and 52 are enlarged in Figure 4.8(c), (d), (e) and (f) respectively so that the cracks in the cells can be noticeable. Cell 21 delivered the lowest voltage, yet it is not cracked, thus the minor cracks on cells 1, 20, 47 and 52 did not affect the individual voltages of the cells. There are no dark cells on the Low EL image, hence no shunt paths or PID are present on the cells. It is beneficial that EL imaging can detect minor cracks as they can develop into critical defects due to harsh environmental conditions which can be experienced when the module operates in the field and can affect the performance and longevity of the module.
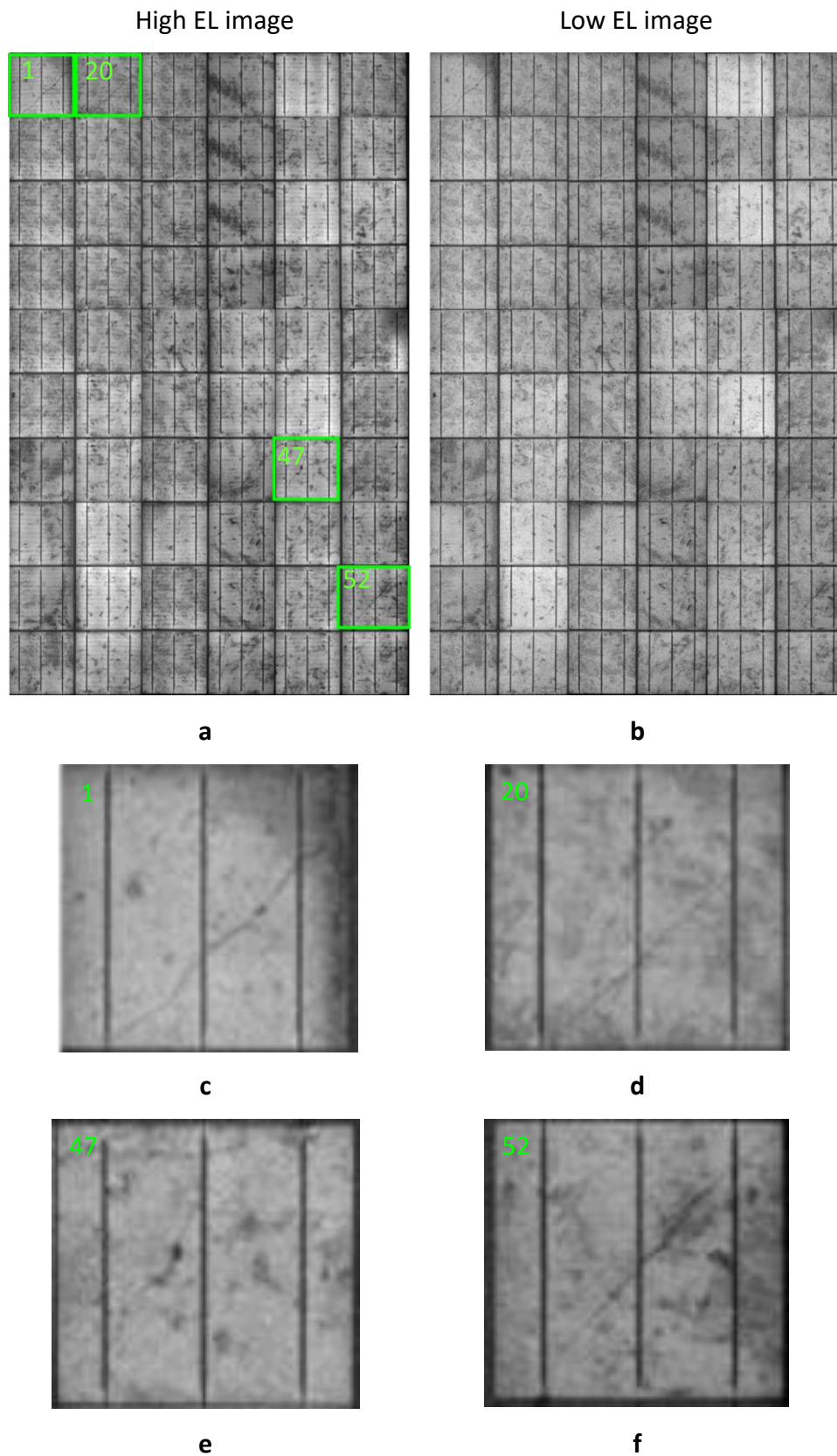
Figure 4.8: (a) High and (b) low current EL images of the multi-crystalline silicon photovoltaic module recorded at (a) 110% and (b) 10% of the I_{SC}. Cells 1, 20, 47 and 52 are enlarged in (c), (d), (e) and (f) respectively.

Figure 4.9 shows the current and voltage measurements as well as thermal characteristics of the individual cells that were recorded simultaneously while shading cell 51 between 0 to 100%. The graphs show the change in the currents generated by the substring, SS3, and module, and operational voltages of the 60 cells in the module when cell 51 was shaded. All the cells operate normally as shown in the figure when the module was unshaded (0%), however, when cell 51 is shaded 4%, its operational voltage is reduced to 0.31 V signifying the expected mismatch while the voltages of unshaded cells and currents of the substring, SS3, and the module are marginally affected. The operational temperature of the whole-cell 51 is not influenced by the small 4% shading, but a hot strip is seen on cell 51, on the respective TIR image, due to the difference in emissivity of the module glass (0.92) and the shading material (paper: cardboard 0.81) [120]. The shading material radiates higher thermal energy than the module glass and hence appears hotter on the TIR image. When the shading area is increased (8 to 100%) on cell 51, it significantly affects the generated currents and marginally affects the operational voltages of the unshaded cells. At an 8% shading level, the voltage of cell 51 becomes negative (reverse bias) and the cell starts dissipating the module's generated electrical energy. When the cell becomes reverse biased, the temperature of the whole-cell 51 increases. The temperature increases up to a shading level of 40%. As the shading level increases to 40%, the currents of the module and substring, SS3, and voltage of the shaded cell 51 reduces significantly while the voltages of unshaded cells rise slightly.
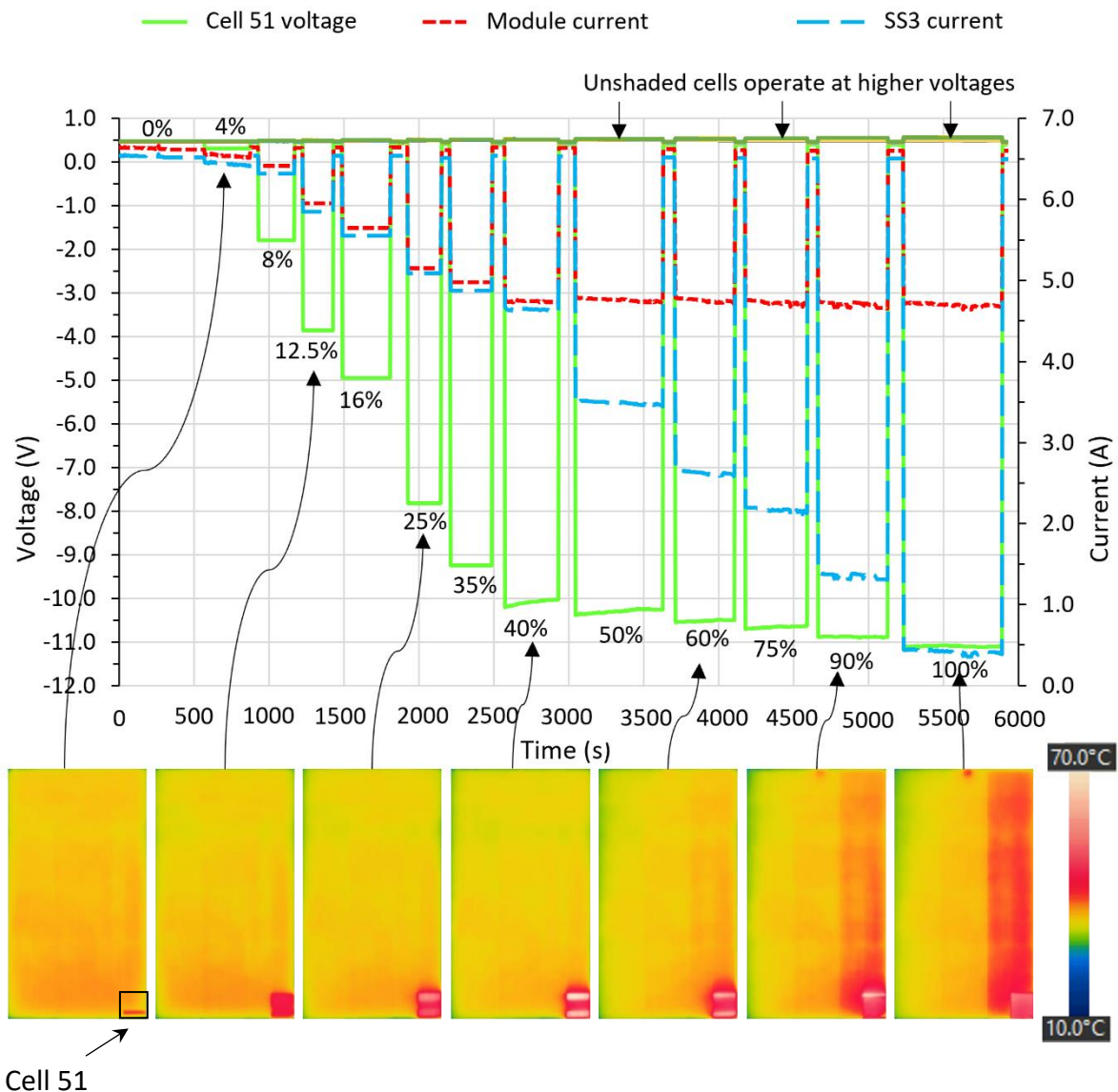
Cell 51

Figure 4.9: Module and substring, SS3, currents and cell voltage measurements together with TIR images taken when cell 51 was under different shading levels, of cardboard covering a portion of the cell. The voltages of the unshaded cells are indistinguishable from each other and show a small increase when cell 51 is shaded.

Progressively smaller changes in module current and voltage of cell 51 occur from a shading level of 50% and above, while the current generated by substring, SS3 continues to drop significantly. The operational temperature of the shaded cell increased with the shaded area between 8- to 40% reaching a peak between 40 and 50%. The cell's temperature decreased for increased shading levels 50 to 100% when the bypass diode of the substring containing cell 51 appears to be activated. The bypass diode diverts the module current around the

shaded substring, SS3, as evidenced by an increase in the junction box temperature containing the bypass diodes and a small increase in the temperature of the whole substring SS3.

The effect of shading on voltages of the unshaded cells is shown in Figure 4.10. The shading applied to cell 51 forced the unshaded cells to operate at higher voltages than when cell 51 was unshaded, as indicated in the figure. The rise in voltage of all unshaded cells depends on the shaded area and is seen in Figure 4.10 for shading levels 4 to 40%. At a shading of 50% and above, the voltages of cells in the shaded substring split from the unshaded substring revealing activation of the bypass diode paralleled to the shaded substring, SS3. Shading of 50 to 100% results in the voltages of cells (e.g cell 60) in the shaded substring SS3, continuing to rise while the voltages of cells (e.g cells 1 and 40) in the unshaded substrings, SS1 and SS2 remain unchanged. The change in the operational voltage of unshaded cells is due to the shift in the operational point (current and voltage) of the module when different shading levels are applied on cell 51.
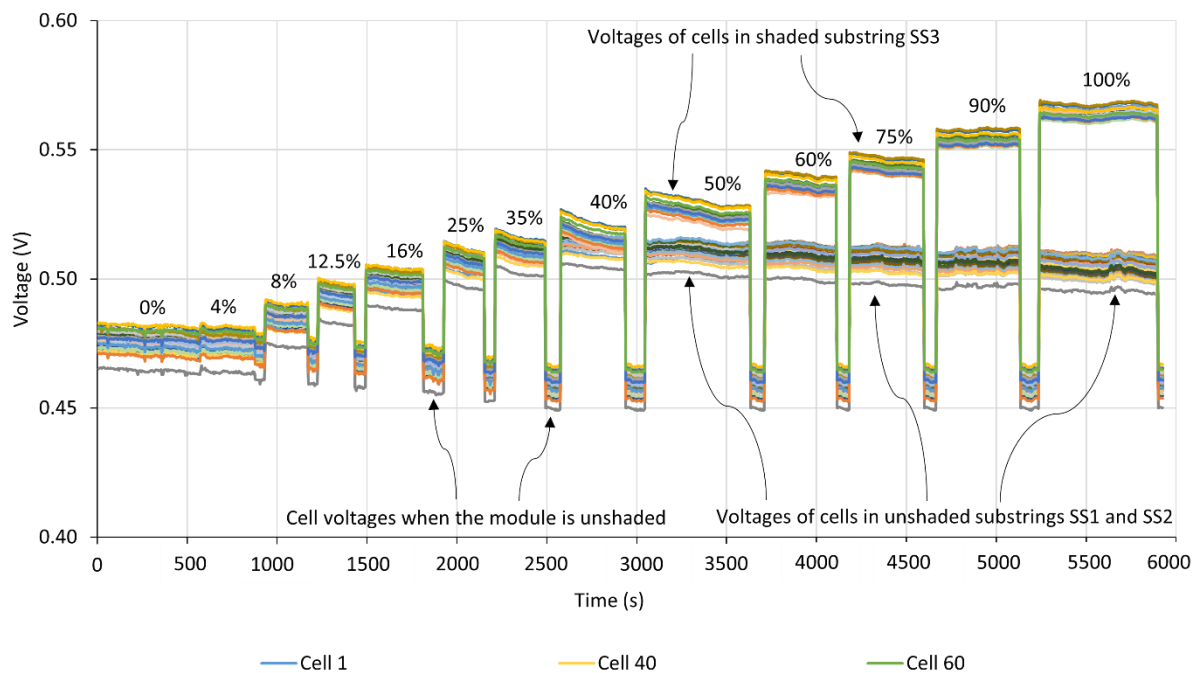
Figure 4.10: Effect of shading on operational voltages of unshaded cells.

Shading of a cell causes a reduced current generation, as illustrated in Figure 4.9, such that the operational voltages of the remaining unshaded cells in the substring are shifted towards V_{OC}. The effect of partial shading of cell 51 on the representative I-V curves of the module is

68

shown in Figure 4.11 with the well-known bumps appearing due to the activation of one bypass diode paralleled to substring SS3. As expected, the depth of the bumps is related to the level of shading of cell 51 and the reduced amount of current generated by the substring. Deep bumps reflect heavy mismatch and shallow bumps indicate light mismatch [18]. Figure 4.11 shows the trends of the operational points (current and voltage) of the module, substring SS3 (not including the bypass diode current), and cell 51 when shading levels of 0 to 100% were applied and while the module was connected to a constant external resistive load. The operational points of the module (circles), substring SS3 (diamonds) and cell 51 (triangles) shift with the shading level and follow linear trends for shading levels of 0 to 40% up to the onset of bypass diode activation. The maximum power points (squares) of the I-V curve characteristics are also shown on the respective I-V curves.
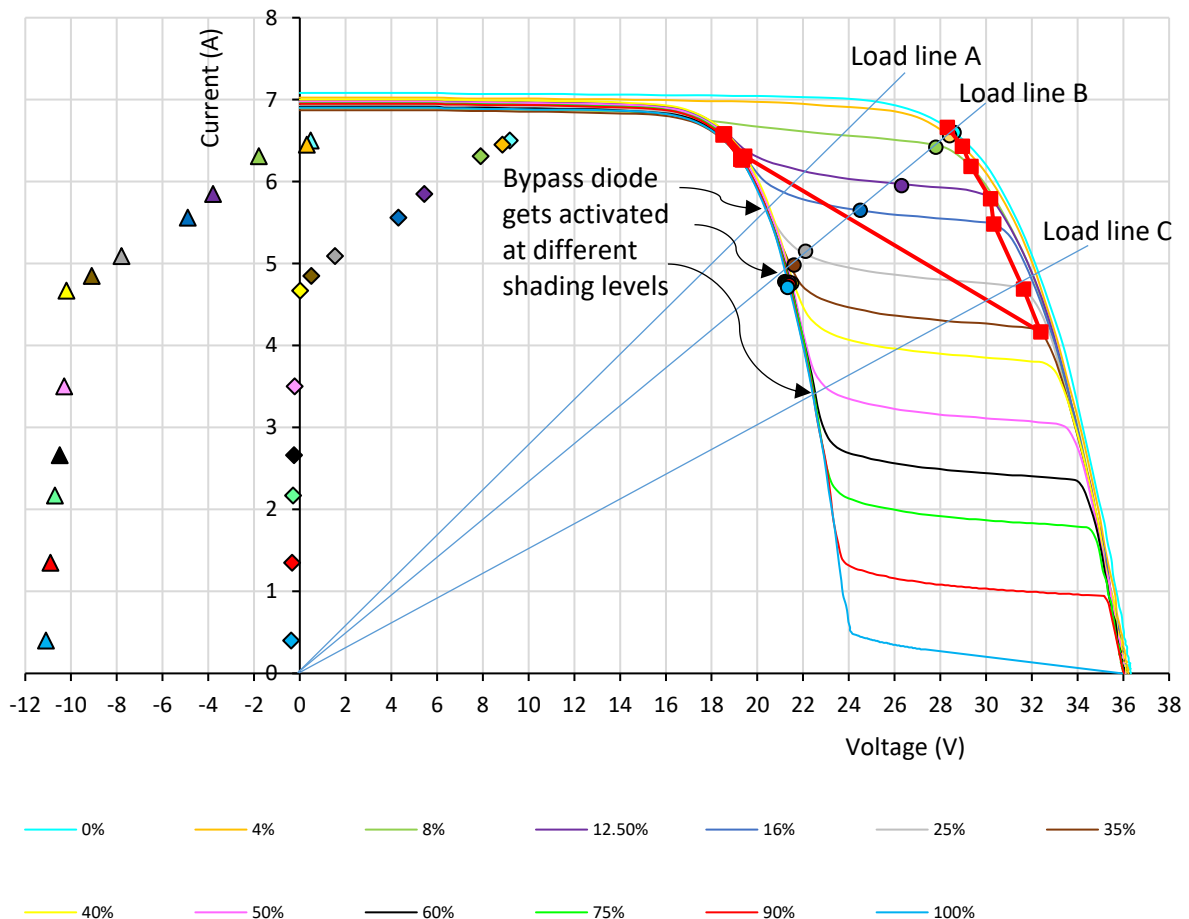
Figure 4.11: Representative I-V curve characteristics of the module when cell 51 was under different shading levels. The operational points of the module (circles), substring SS3 (diamonds), and cell 51 (triangles) are indicated for different shading levels, 0 to 100%.

From 50 to 100% the operational points (circles) of the module remain relatively unchanged, as SS3's bypass diode becomes activated, diverting the module's current around the substring to reduce the reverse bias heating effects on cell 51. The activation of the bypass diode, therefore, causes the operational current and voltage of the substring SS3 (diamonds) and cell 51 (triangles) to drop drastically as shown in Figure 4.11.

The required voltage range for the bypass diodes to activate and begin to bypass the module current around an affected substring can be observed as "bumps" or a sharp rise in current on the family of I-V curves shown in Figure 4.11. The operational current and voltage of the module, substring and cells are therefore influenced by the shading level and the current-voltage profile of the load. In this case, a simple linear resistive load was chosen to simplify the analysis. The onset and full activation of a bypass diode for a particular resistive load will occur over a small range of voltages and corresponding shading levels. As an illustration, consider load lines A, B and C in Figure 4.11. For load line A, small shading level of 25% can cause the onset of full activation of the bypass diode while for load line B and C the bypass diode has not been activated at the same 25% shading level (grey I-V curve). For load line C, the onset of activation only occurs at a 60% shading level. It is important to note that for load lines A, B and C, the bypass diode never becomes fully activated at any shading level. The load lines A, B and C also do not represent the more complex I-V characteristics of MPP trackers. The load points for a MPP tracker are shown by the red line for shading levels of 0 to 100% and do not follow a predictable linear pattern as is the case with a constant resistive load.

The operational points of a PV source translate to the power it generates or dissipates [68][69]. Figure 4.12 shows the relationship between the power and shading level when the module is connected to a constant resistive load as indicated by load line B in Figure 4.11. The power generated (positive) or dissipated (negative) by the module, substring SS3 and shaded cell 51 for each shading level is indicated together with the respective operational temperature of the shaded cell 51.

The power generated by the module and substring SS3 decrease from about 190 W and 60 W to 100 W and 0 W respectively for shading levels of 0 to 40% and remains unchanged for shading levels 50 to 100%. The shaded cell 51 appears to be generating a small amount of power between 0-4% shading levels but switches to dissipating power between 4-8% shading when the cell becomes reverse biased. The temperature of the shaded cell is strongly related to the power generated or dissipated (due to resistive heating) by the shaded cell. The most significant temperature increase occurs when the shading increased from 4 to 40% when the cell dissipates power but starts to decrease when the bypass diode of SS3 became activated for shading levels of 50 to 100%. Substring SS3 generates continuously less current with an increase in shading level as shown in Figure 4.9, even when the bypass diode is activated, therefore the shaded cell will in turn dissipate less energy after activation of the bypass diode.

bypass diode.
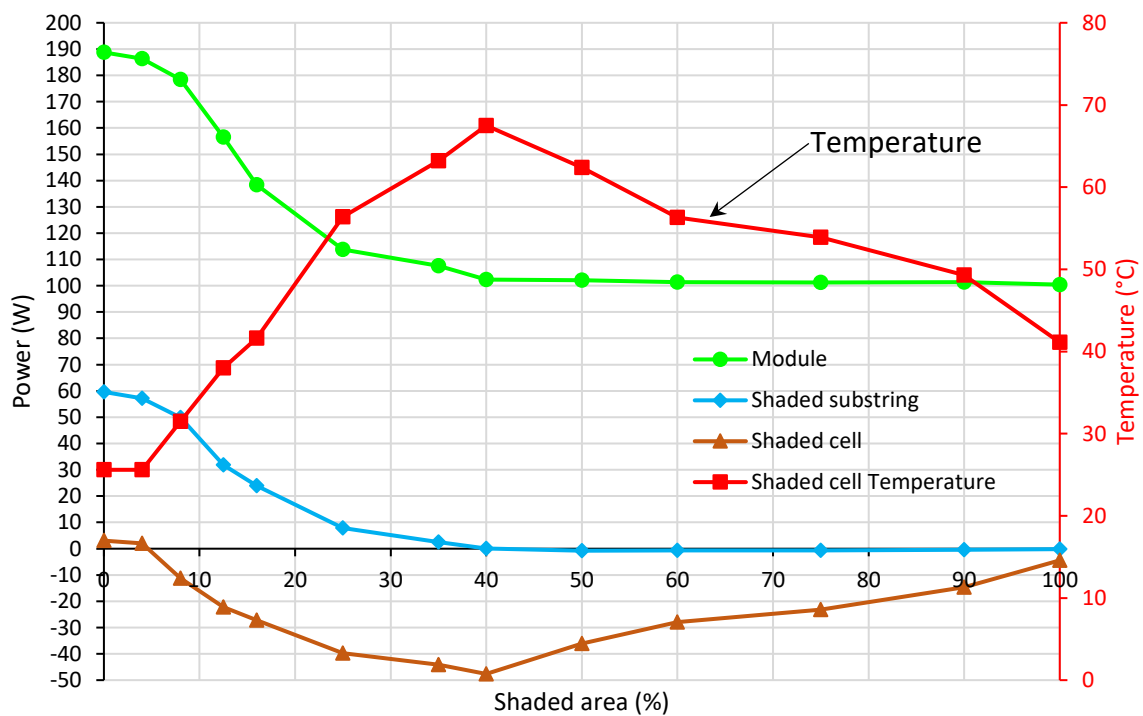
Figure 4.12: Power and operational temperature trends under different shading levels of cell 51.

The point when the bypass diode is fully activated is crucial for optimum power generation as well as avoiding excessive heating on the shaded cell which can result in cell discolouration, back sheet damage, module glass cracks and risk of fire in worse scenarios. Figure 4.13 shows

power scenarios at different cell shading levels when the external load resistance is constant (Load lines A, B and C) or at maximum power (MPP). The point where the bypass diode of the substring containing the shaded cell is fully activated is also the point when the module power starts to flatten. The MPP line shows the maximum power that can be generated by the module at each shading level. The activation point of the bypass diode for the MPP load is at 40% shading, which is equal to the activation shading of load line B. The resistance for load line B was chosen to be close to the maximum power point. The forward bias voltage, which is around 0.35 V for Schottky bypass diodes, as mentioned in Section 2.6.3, is not affected by the change in the load conditions. However, the change in load conditions influences the operational point of the module and cells such that the shading level point at which the forward bias voltage is created to activate the bypass diode is different.
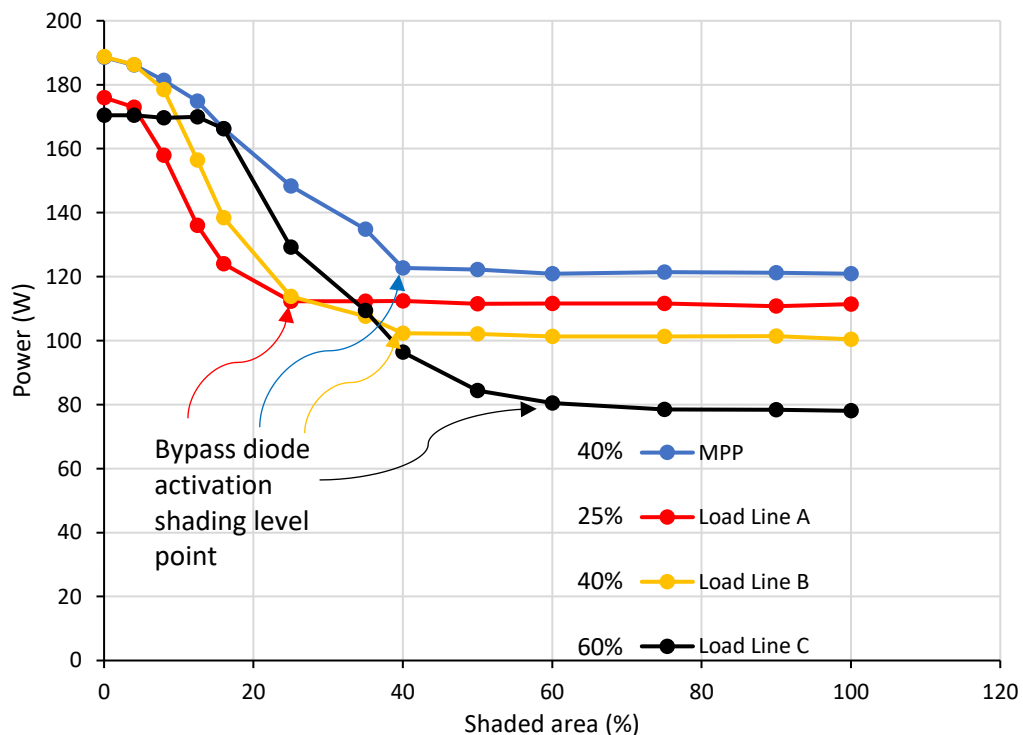
Figure 4.13: Trends of power generated by the module at different load lines.

When a module operates with a smaller constant external resistance, as in the case with load line A in Figure 4.11, the forward bias voltage to activate its bypass diodes occurs at smaller shading levels (25%). Although there is an associated power loss, the activation of the bypass diode reduces the risk of overheated cells. The module power output stabilises at 110 W at the onset of the bypass diode activation. At a higher constant resistance load as in the case with load line B (Figure 4.11), the forward bias voltage required to activate the bypass diodes

72

occurs at higher shading levels (40%), associated with the onset in power loss, stabilising at a lower module power of 100 W. When the external resistive load is higher as shown with load line C in Figure 4.11, the forward bias voltage for activation of bypass diodes occurs at even higher shading levels (60%), stabilising at a lower module power of 80 W. This scenario could lead to accelerated module degradation due to continued overheating on the shaded cell. As expected, when a MPP module load is used, the power output is maximised throughout all shading levels and the bypass diode is fully activated at a cell shading level of 40%.

Similar results as shown in Figure 4.9 were obtained when the experiment was repeated on different days with the module under similar operational conditions and when shading was applied on different cells. When an equal shade, e.g shading level of 8%, was applied to the cell in different orientations such as along the fingers, along the busbars and diagonally, there was no significant change in the operational voltage of the shaded cell and the currents of SS3 and the module. The cell voltage and current of the module and SS3 were almost the same as seen in Figure 4.9, that is -1.8 V, 6.3 A and 6.4 A respectively, regardless of shade orientation. However, changes in the operational conditions such as irradiance and load conditions influenced the operation of the individual cells, substrings and the module, as well as the shading level point causing the forward bias voltage and activation of the bypass diode. Under low irradiance of 400 – 500 W.m^{-2} the currents generated by the module and SS3 were lower at each shading level than at high irradiance, 700 – 1000 W.m^{-2}. The low current generation in SS3 resulted in the operational temperature of the shaded cell being lower at shading levels 8- to 100% than under high irradiance due to minimal current mismatch between the shaded and unshaded cells in substring SS3. Similar trends in currents, voltages and operational temperature, as seen in Figure 4.9, were followed under low irradiance. The ambient temperature was around 20 °C on colder days and around 30 °C on hotter days and there was no significant change in the observations.

This study of the effects of partial soiling on PV modules is important since soiling of field mounted modules is unavoidable, as mentioned earlier. The study provides in-depth information on the operation of the modules, substrings and cells and can improve the interpretation and understanding of thermal images of PV modules operating under varying shading conditions. Other studies [17][18][21][121][122], analysed I-V measurements of PV strings and modules under different operational conditions, mainly shading conditions, and

also in the publications [51][117][123], the I-V measurements were correlated to TIR images to analyse the effects of thermal signatures on the performance of the strings and modules.

4.3 Influence of varying the load, irradiance and output power on abnormal thermal signatures

4.3.1 Effects of changing irradiance and output power on abnormal thermal signatures of operational monocrystalline silicon PV modules

The influence of changing irradiance and output power on the behaviour of abnormal thermal signatures of a 1.6 kW monocrystalline silicon array is discussed in this section. The results in this section were obtained after carrying out an experiment that is described in Section 3.2. The array contains nine monocrystalline PV modules of type SW-175 mono (Module B) and the visual image in Figure 3.1 shows the arrangement of the modules. The specifications of Module B are indicated in Table 3.1 in Section 3.1.

Figure 4.14 shows TIR images of the 1.6 kW array that were recorded when irradiance dropped in the order (a) 1000 $W.m^{-2}$, (b) 800 $W.m^{-2}$ and (c) 650 $W.m^{-2}$, when the array was generating power of approximately 1100 W, 900 W and 600 W, respectively. Figure 4.14(a) shows the non-uniform temperature distribution in the plane of array that was caused by several abnormally hot cells in string 3, module 2, substring 3 (ST3-M2-SS3). The bad cells were underperforming and created a current mismatch with good operating cells, forcing the bad cells to operate at elevated temperatures compared to the good cells. The bad cells in the substring ST3-M2-SS3 and also ageing of the modules, as they have been operating in the field for years, resulted in the array not performing to the nominal power when under irradiance of 1000 $W.m^{-2}$.

a

Irradiance = 1000 W.m^{-2},
Output power = 1100 W

ST3-M2-SS3

b

Irradiance = 800 W.m^{-2},
Output power = 900 W

c

Irradiance = 650 W.m^{-2},
Output power = 600 W
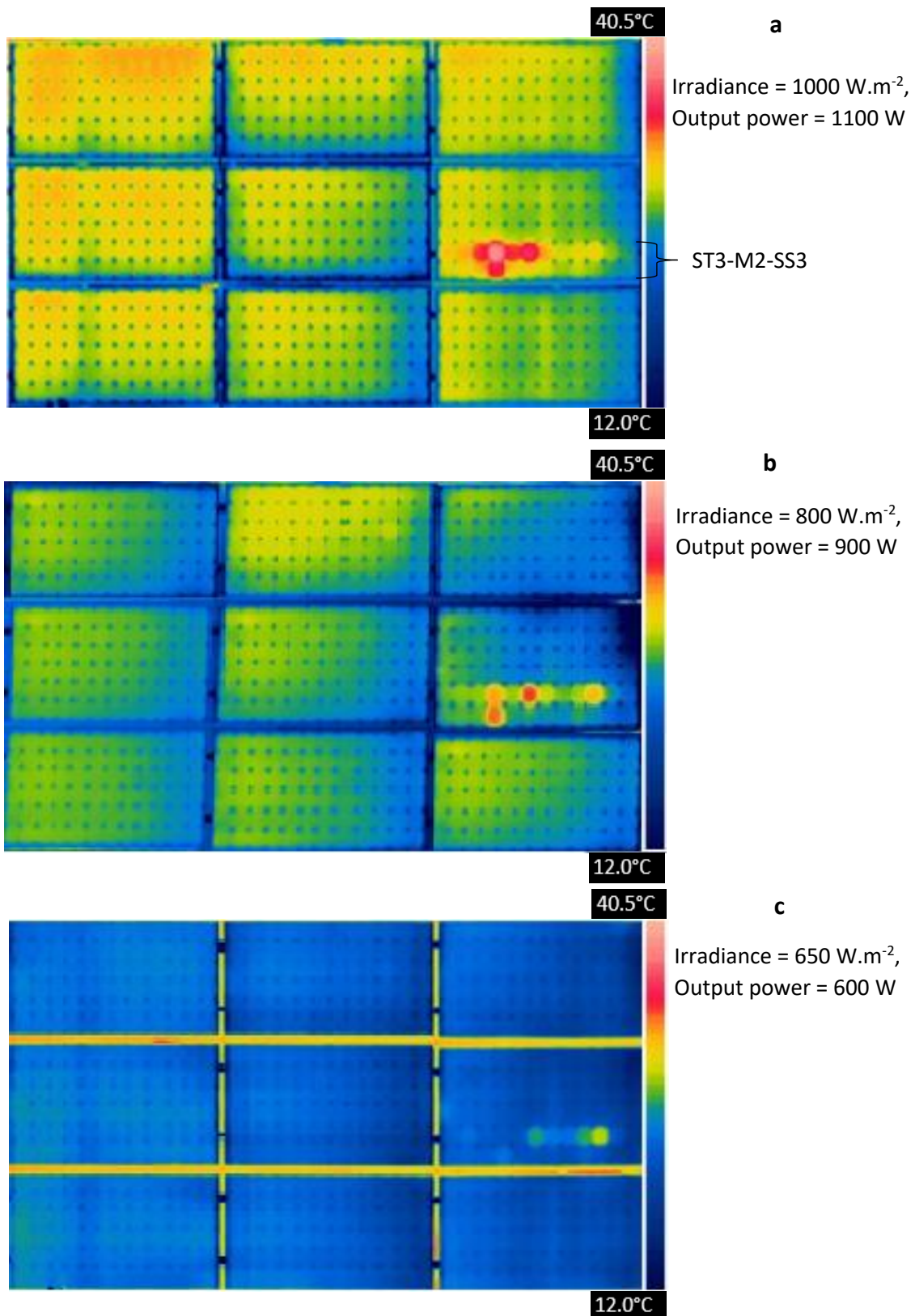
Figure 4.14: TIR images of the 1.6 kW array captured under different irradiance and output power, (a) Irradiance of 1000 W.m^{-2} and output power of 1100 W, (b) Irradiance of 800 W.m^{-2} and output power of 900 W and (c) Irradiance of 650 W.m^{-2} and output power of 600 W.

When the operational conditions changed from high irradiance (1000 W.m^{-2}) and output power (1100 W) to lower irradiance (800 W.m^{-2} and 650 W.m^{-2}) and output power (900 W and 600 W), the number of the abnormally hot cells in the underperforming substring ST3-M2-SS3 is reduced. The TIR images in Figure 4.14(a), (b) and (c) are presented on the same temperature scale and it can be seen, from the TIR images, that the operational temperature of bad cells in substring ST3-M2-SS3 drops with a decrease in irradiance and output power. The temperature of all the modules in the array also drops with a decrease in irradiance and output power. At lower irradiance, the lower current that is produced by the solar cells, resulted in a lower current mismatch with an associated reduction in the number of abnormal hot cells. The lower current mismatch resulted in the bad cells dissipating less electrical energy as heat and operating at lower temperatures.

Figure 4.15 shows the TIR image of the array when it was switched off and received high irradiance of 1000 W.m^{-2}.
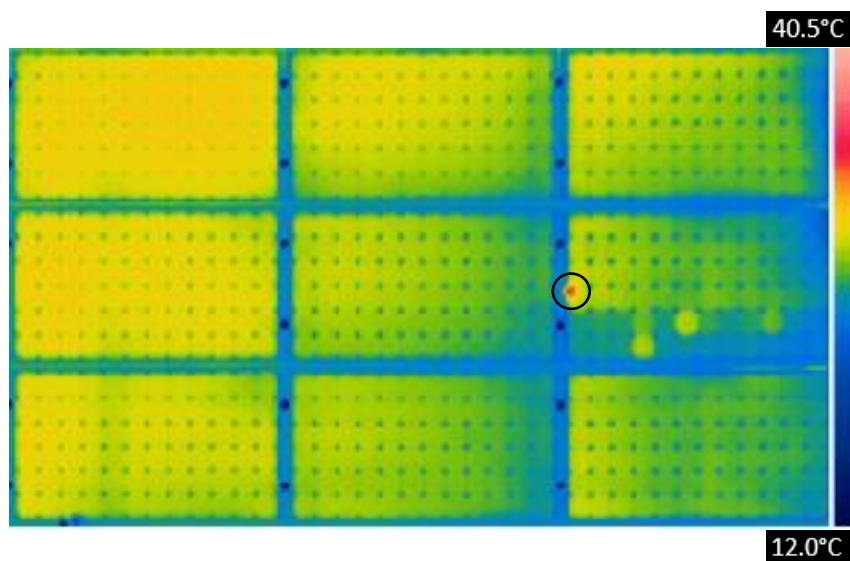
Figure 4.15: Thermal image of the 1.6 kW array when it was in open circuit conditions and receiving 1 sun.

Almost all cells in the modules of the array appeared equally warm since the cells are heated by sunlight absorption and do not generate electrical energy. However, it is different in substring ST3-M2-SS3 as some abnormally warm cells and a hot junction box are seen in the TIR image. The hot junction box (circled in the TIR image in Figure 4.15) is due to an overheating bypass diode that conducts the current generated by the substring ST3-M2-SS3 when the array operates under no load. The bypass diode is faulty, acting as a resistor, and

forcing the respective substring to produce current by completing the substring's series cell circuit, thus creating a looped current path, even when the array/string was disconnected from the load and in open circuit. The bypass diode does not appear to be abnormally hot on TIR images in Figure 4.14 while operating normally, since it is acting as a current resistor limiting the amount of current to pass through it. The faulty bypass diode acting as a resistor will force the substring containing the bad cells to contribute some of the current it produced to the module. If the bypass diode operated normally with an increasing mismatch, the substring would tend to become more open-circuited, with a reduction in substring current, as described in Figure 4.9.

This scenario of the damaged bypass diode acting as a resistor is also discussed by S. W. Ko et. al, when the researchers showed that a faulty bypass diode can be at an extremely high temperature when the module is delivering power to load, and when the module is generating energy the temperature of the bypass diode drops [124]. To advance the understanding of TIR images and the operation of bypass diodes (normal and faulty) under different operational conditions, further studies will be carried out with the currents of the module, substrings and bypass diodes being monitored and recorded.

Figure 4.16 shows the I-V measurements of the strings and selected modules of the array while Figure 4.18 shows the EL image of the array. The I-V characteristics in Figure 4.16 and the EL image, Figure 4.18, show that the substring ST3-M2-SS3 was not operating normally.
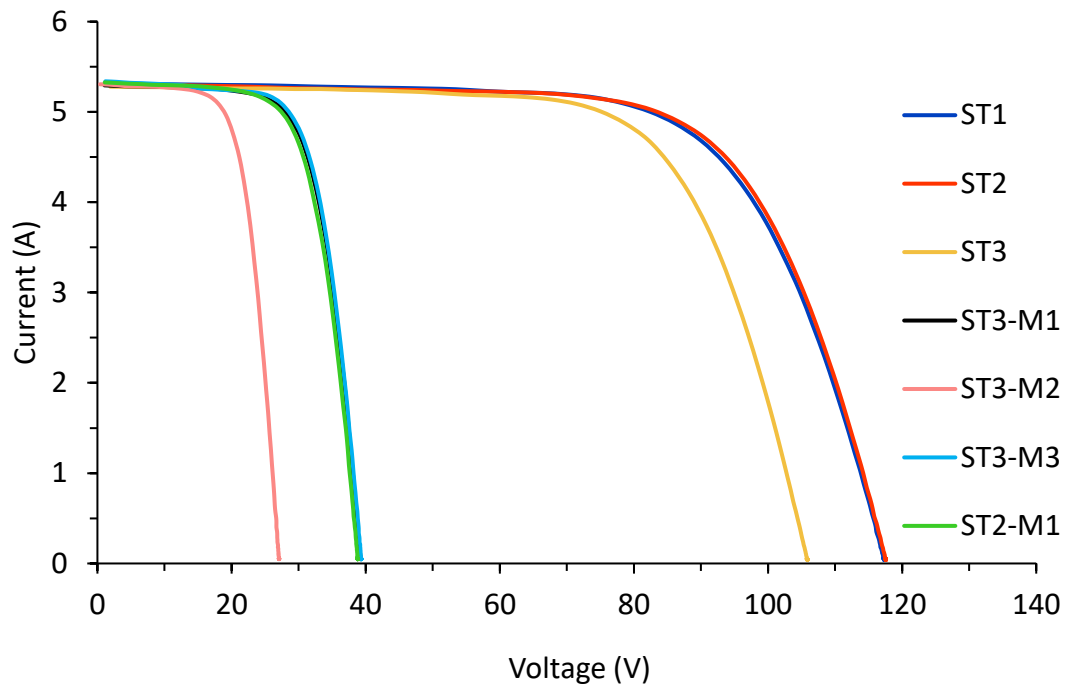
Figure 4.16: I-V curve characteristics of the strings and modules in the 1.6 kW array.

The I-V parameters of good performing strings, ST1 and ST2, match each other but differ from the I-V parameters of ST3 which was underperforming because of the damaged bypass diode of substring ST3-M2-SS3. The I-V characteristics of the module ST3-M2 show that the module is underperforming when compared to modules ST2-M1 and ST3-M3 due to different $V_{OC}s$ and MPPs. The substring caused a drop in V_{OC} of approximately 12 V (~V_{OC} of one substring) between good and bad operating strings, and modules. The I-V parameters of the strings and modules in the 1.6 kW array were modelled in PVSim [64], to simulate the I-V characteristics of a good string, bad string, good module and bad module in the array, respectively. The simulations, References 1, 2, 3 and 4 shown in Figure 4.17 are similar to the I-V curves of ST1, ST3, ST3-M1 and ST3-M2 in Figure 4.16, respectively with insignificant voltage differences per each corresponding current value. Thus, the experimental results shown in Figure 4.16 follow the simulations obtained in PVSim.
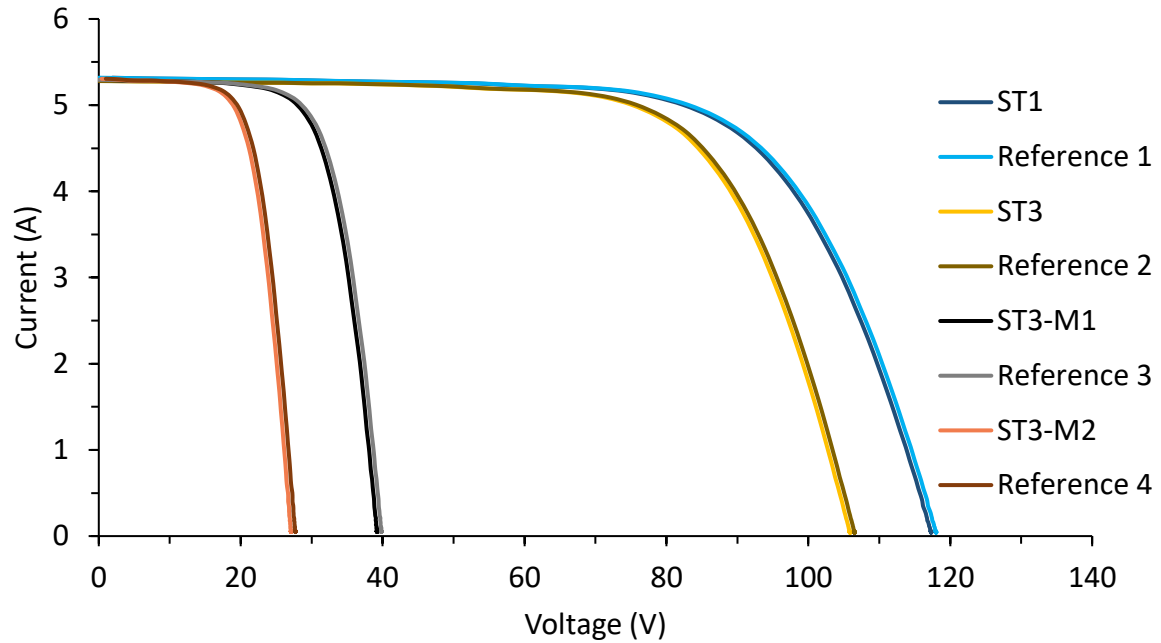
Figure 4.17: I-V curves of strings and modules in the 1.6 kW array compared to references that were simulated in PVSim.

Table 4.2 shows the I-V parameters of the strings and modules shown in Figure 4.16.

Table 4.2: Performance parameters of the strings and modules in the 1.6 kW array.

String / Module	I_{SC} (A)	V_{OC} (V)	I_{MP} (A)	V_{MP} (V)	P_{max} (W)
	±1.2%	±0.8%	±1.4%	±0.9%	±4.2%
ST2-M1	5.3	38.7	4.7	29.9	139.3
ST3-M2	5.3	27.1	5.2	22.0	114.4
ST2	5.3	117.6	4.9	86.6	424.3
ST3	5.3	105.9	4.7	82.1	385.9

The abnormalities in substring ST3-M2-SS3 shifted the MPP of string ST3 and module ST3-M2 and resulted in a power loss of 18% on module level which translates to 9% on a string level. The shift in MPP will require a high MPP tracking efficiency to quickly optimise power delivery to the load [24][125][126]. A bypass diode across an underperforming substring will be activated and cause a bump in I-V curve if the substrings are significantly mismatched [78], as highlighted in Section 2.6.1. However, no bump is seen on the I-V curves of the underperforming string ST3 and module ST3-M2 since the bypass diode across the substring

is faulty and operating as a resistor. The EL image of the array confirmed that the bypass diode is damaged as shown in Figure 4.18. The good cells luminesce when forward biased and the intensity of photoemission from the good cells is bright and almost uniform. However, bad cells have dark areas, EL features, as shown in the EL image in Figure 4.18.
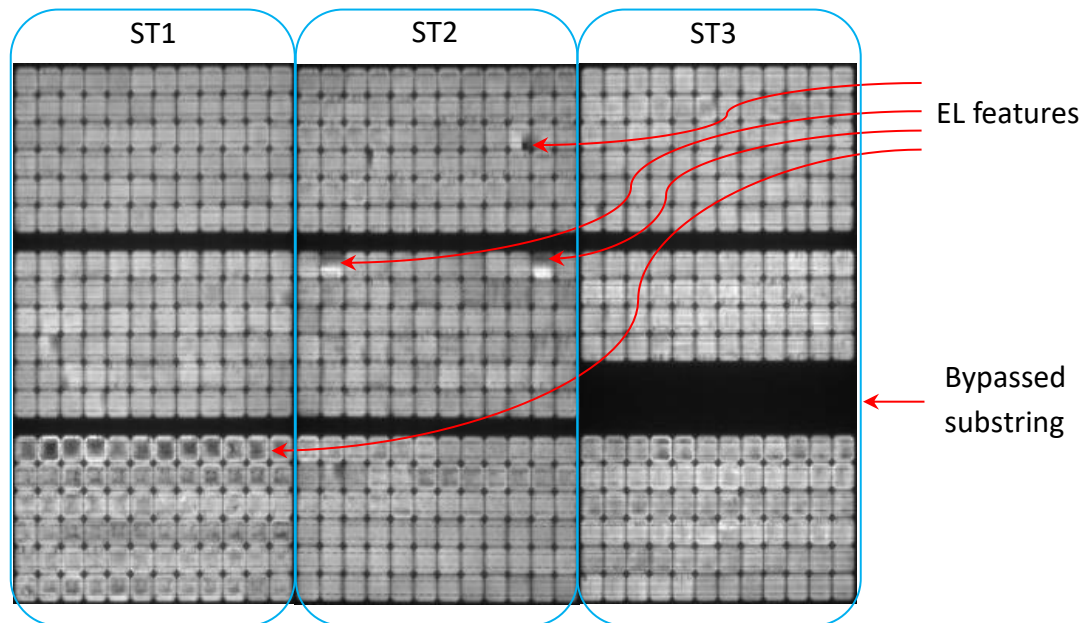
Figure 4.18: EL image of the 1.6 kW array showing a bypassed substring and other EL features.

The substring ST3-M2-SS3 appears complete dark since it was bypassed de when the substring was forward biased for EL imaging. If the bypass diode was not damaged, then the applied current would have forward biased the individual cells in the substring ST3-M2-SS3 and revealed the problematic cells. Figure 4.18 reveals other problematic cells showing EL features such as busbar disconnects. The anomalies on these cells do not cause a significant current mismatch for them to appear as hot spots on TIR images. I-V and EL inspection techniques identified the substring ST3-M2-SS3 to be problematic as a whole but not all the cells in the affected substring are poor performers, as revealed by the TIR imaging inspection method. TIR imaging located the individual cells which were underperforming under different operational conditions within the affected substring ST3-M2-SS3.

The bypass diode paralleled to the substring ST3-M2-SS3 was confirmed to be faulty by using a digital multimeter (DMM). EL images of the module ST3-M2 were taken with the bypass diode paralleled to substring ST3-M2-SS3 disconnected from the module. Figure 4.19 shows (a) high and (b) low EL images of the module without the bypass diode on substring ST3-M2-

SS3. The cells which appeared abnormally hot on TIR images in Figure 4.14 are indicated in Figure 4.19(a). The highlighted cells are not cracked and do not appear dark on the Low EL image in Figure 4.19(b). Therefore, these are poor quality cells that caused a current mismatch when connected to good cells in the same series string.
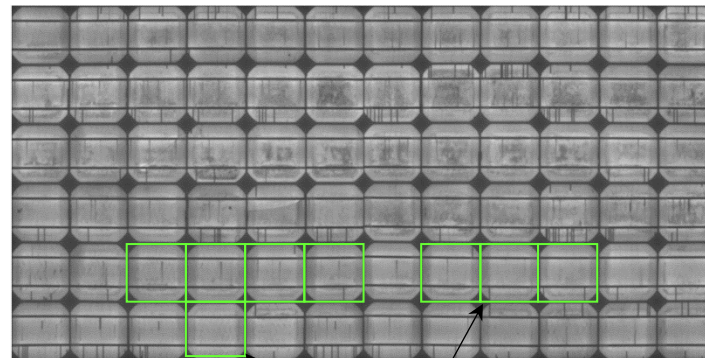
Cells that appeared abnormally hot on TIR images

a – High EL image
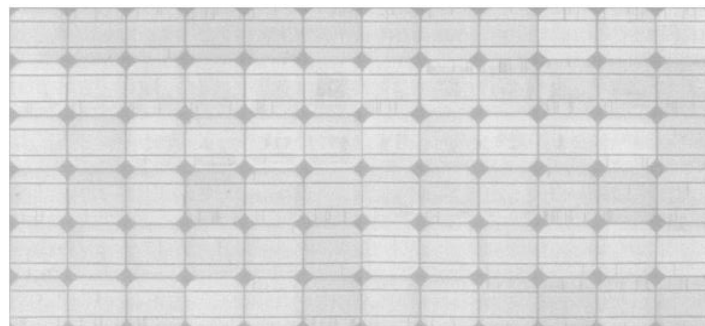
b – Low EL image

Figure 4.19: (a) High and (b) Low EL images of the monocrystalline silicon module taken with bypass diode on substring ST3-M2-SS3 disconnected.

4.3.2 Dynamics of thermal signatures on operational polycrystalline silicon PV module under varying irradiance

Figure 4.20 reveals the behaviour of hot cells when a polycrystalline silicon PV module (SW 240 poly) was operating under changing irradiance for a day, following the experimental description in the last part of Section 3.5. The manufacturer's specifications of the module (SW 240 poly, Module D) are shown in Section 3.1, Table 3.1. Figure 4.20 shows TIR images (a), (c), and (e) that were captured when the module was unshaded and operating under irradiance of 500 W.m^{-2}, 1100 W.m^{-2} and 550 W.m^{-2}, respectively. TIR images (b), (d), and (f)

were recorded under irradiance of 500 W.m^{-2}, 1100 W.m^{-2} and 550 W.m^{-2}, respectively, with one cell partially shaded, ~5%.
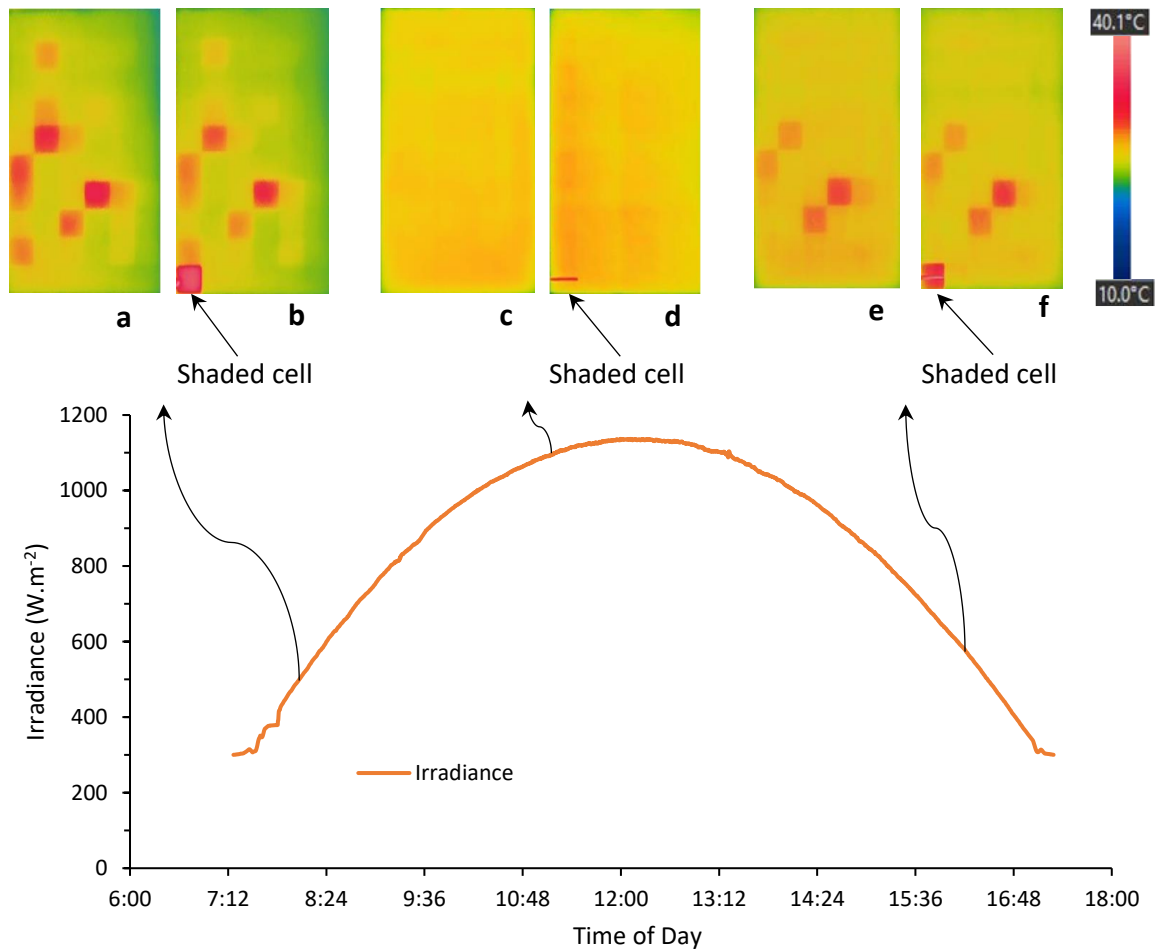
Figure 4.20: TIR images of the polycrystalline PV module captured under varying irradiance, with partial shading on one cell [TIR images (b), (d) and (f)] and with unshaded cells [TIR images (a), (c) and (e)]. The TIR images were recorded under irradiance of 500 W.m^{-2} [(a), (b)], 1100 W.m^{-2} [(c), (d)] and 550 W.m^{-2} [(e), (f)].

The TIR image (a) shows abnormally hot cells when the module is unshaded and operating under low irradiance of 500 W.m^{-2}. When partial shading is applied to one cell, TIR image (b), the whole-cell appears abnormally hot as the shaded cell operates in reverse bias (negative voltage). Similar effects are shown on TIR images (e) and (f) when the irradiance incident on the module is about 550 W.m^{-2}. However, when the irradiance is of the order 1000 W.m^{-2}, there is no significant mismatch to cause abnormal hot cells. All the cells appear to operate normally with uniform temperature as seen on TIR images (c) and (d). TIR image (d) shows a hot strip due to the shading material, paper: cardboard. The shading material appears hot

since its thermal emissivity is higher than that of the module glass [113][100]. Although the shaded cell is reverse biased and abnormally hot on TIR images (b) and (f), the small shading applied to the cell could not cause activation of the bypass diode, hence the abnormally hot cells are still visible on TIR images as there is still a significant current mismatch between bad and good cells. This is different to the scenarios shown in Figures 4.1 and 4.5, in Section 4.2.1, when partial soiling was applied to a cell. Additionally, the current mismatch is not only influenced by the shaded cell area, but also by the operational conditions such as irradiance and load conditions as highlighted in Sections 4.3.1 and 4.3.4, respectively. The change in the operational current and voltage of the module due to varying irradiance influences mismatch and results in the dynamics of the abnormal thermal signatures or hot cells.

Figure 4.21 shows the I-V curve characteristics of the module that were recorded when the module was receiving high and low irradiance of 1000 $W.m^{-2}$ and 500 $W.m^{-2}$, respectively. The effect of a change in irradiance on the operational points of the module, which resulted in the dynamics of the thermal signatures, is illustrated in Figure 4.21. The drop in irradiance, from higher irradiance (1000 $W.m^{-2}$) to lower irradiance (500 $W.m^{-2}$), caused a reduction in the generated current, as expected, and results in a shift of the maximum power point, MPP1 to MPP2. The load line represents constant load conditions and shows that the module operates at MPP1 under higher irradiance and when the irradiance is lower (500 $W.m^{-2}$), the module delivers less current and its operational voltage shifts towards 0 V along the I-V curve, as shown by the operational points in Figure 4.21. When the operational point is closer to 0 V the module generates a high current such that cell mismatch can easily occur, unlike when the module's operational point is closer to V_{OC}, when current generation is low and hence minimal or insignificant cell mismatch occurs. Sections 4.3.3 and 4.3.4 discuss the scenario and the TIR images in Figure 4.22 and 4.25 reflect this scenario causing the dynamics of abnormal thermal signatures. This causes the bad cells (or poor-quality cells) to appear abnormally hot on the TIR image when the module operates under low irradiance, in the mornings, evenings and under cloud cover, but appears normal under high irradiance. It is generally recommended to carry out TIR imaging on-field mounted modules when the irradiance is above 600 $W.m^{-2}$, when the cells operate at maximum performance. Under such conditions, any abnormally hot cells which appear on TIR images will indicate severely mismatched cells which can impact on performance and longevity of the affected module.
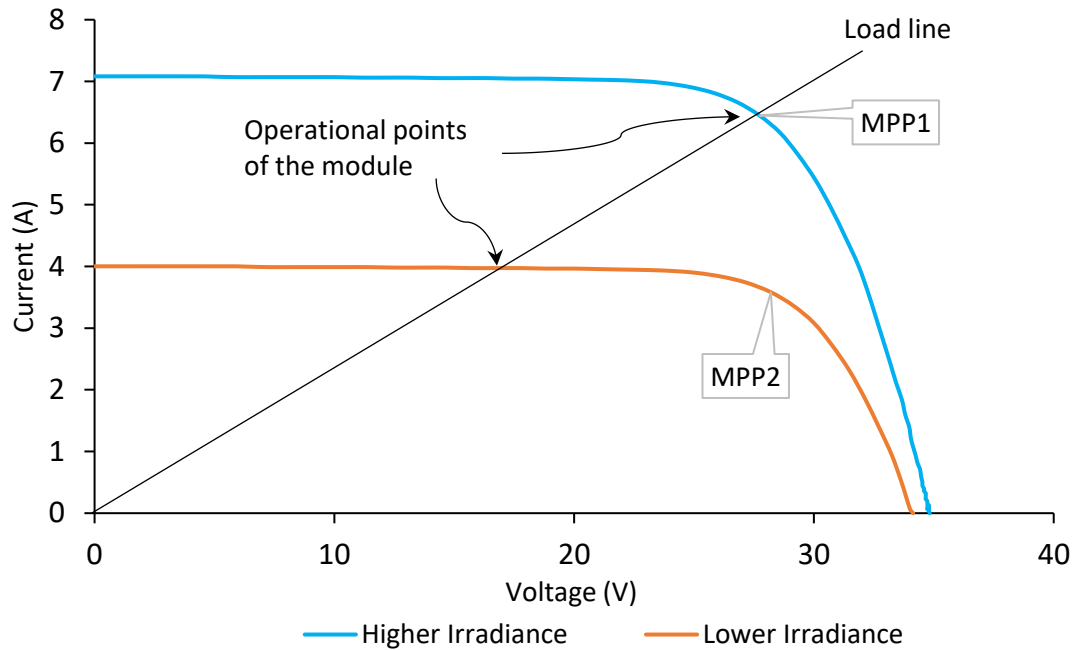
Figure 4.21: I-V curves of a crystalline PV module operating under constant load conditions and different irradiance levels.

Mismatched cells can operate at elevated temperatures when the current of good operating cells is passed through the underperforming cells resulting in localised resistive heating when mismatched cells dissipate electrical energy. When the module's operational voltage is closer to V_{OC}, it generates a low current (considering the I-V curve) and delivers less power than expected, but the cells will operate with a low chance of being mismatched than when the operational voltage is below V_{MP}. This avoids mismatch effects which can cause abnormal heating on mismatched cells. Continued abnormal heating on PV cells can result in damage to the back sheet, cell cracks, risk of fire and quick module degradation. The behaviour of PV cells under different operational conditions, discussed in this paper, can improve the operation and maintenance of PV systems.

4.3.3 Dynamics of abnormal thermal signatures on operational monocrystalline silicon PV module under varying load

The results presented in this section were obtained after carrying out an experiment described in Section 3.4. The effects of varying load on the abnormal thermal signatures of a monocrystalline silicon PV module are discussed in this section. The module specifications (AP-6105 mono, Module B) are shown in Table 3.1, Section 3.1.

Figure 4.22 shows TIR images of the monocrystalline silicon PV module that were recorded when the module was operating under constant high irradiance (1000 W.m^{-2}) and changing load conditions. The TIR images, A-F, shown in the figure were recorded when the module was short-circuited (load = 0.0 Ω), connected to loads of 4.0, 8.0, 10.0 and 12.0 Ω and when the module was open-circuited, respectively. When the module was under load conditions of 4.0, 8.0, 10.0 and 12.0 Ω it generated a current of approximately 85%, 70%, 50% and 40% of the I$_{SC}$, respectively. The I-V curves of the module and two substrings, SS 1 and SS 2, are also shown in the figure.

The TIR images in Figure 4.22 show abnormally hot cells which decrease in number from TIR images A to E. It can be seen that as the load/resistance increases, 0.0 to 12.0 Ω, some hot cells disappear until all cells in the module appear to operate normally at uniform temperature when the load reached 12.0 Ω on TIR image E. The temperature difference, ΔT, between the abnormally hottest cell, with a peak temperature of 74.6 °C at I$_{SC}$, and the reference cell, operating at 40.7 °C at I$_{SC}$, decreases with an increase in load. The effects follow the decrease in the amount of current generated but are contrary to the increase in voltage supplied by the module and are indicated by the operating point or position of each TIR image along the I-V curve of the module. This is summarised in Table 4.3.
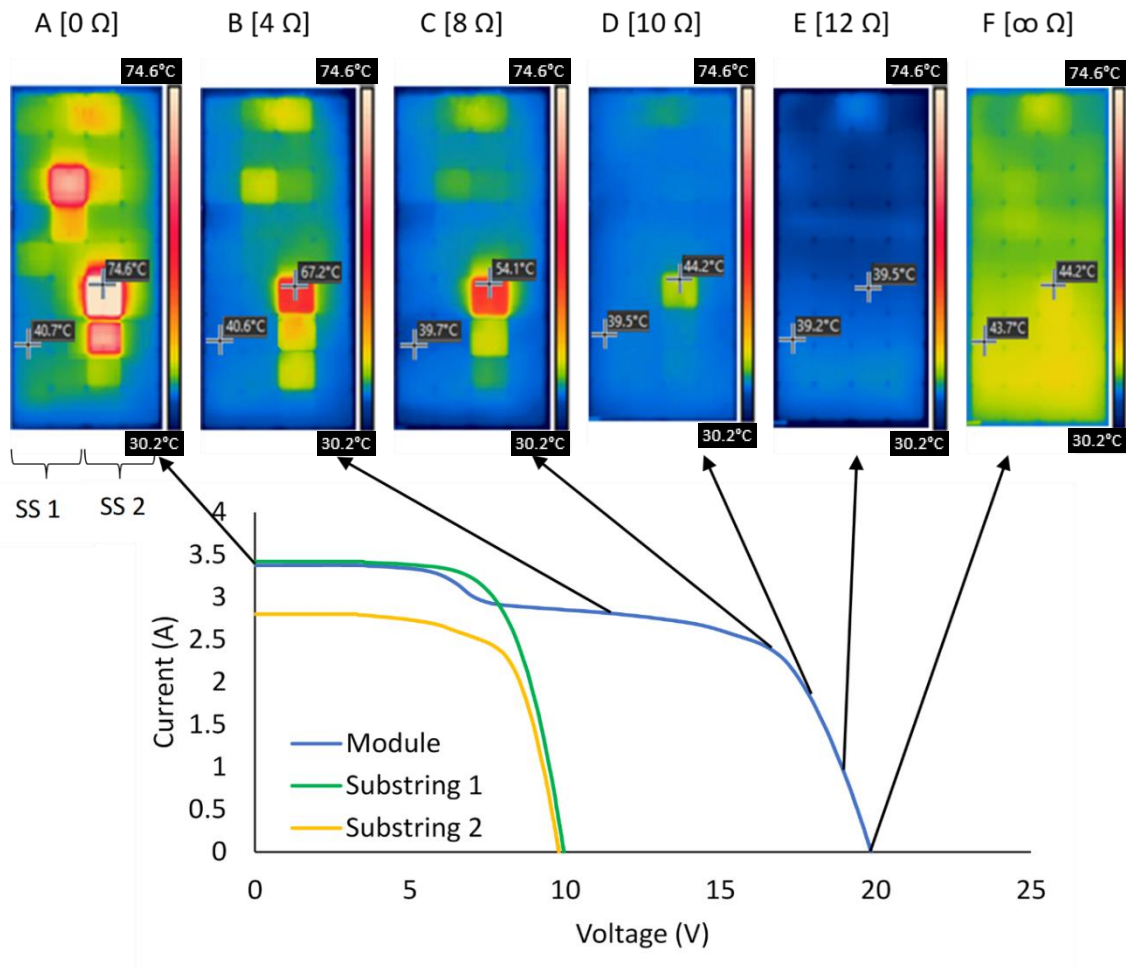
Figure 4.22: Thermal infrared images of the monocrystalline module captured under varying loads and the current-voltage plots of the module and substrings.

Figure 4.23 shows the I-V curves, with similar trends as shown in Figure 4.22, which were generated in PVSim after modelling the operation of the monocrystalline module and the substrings.
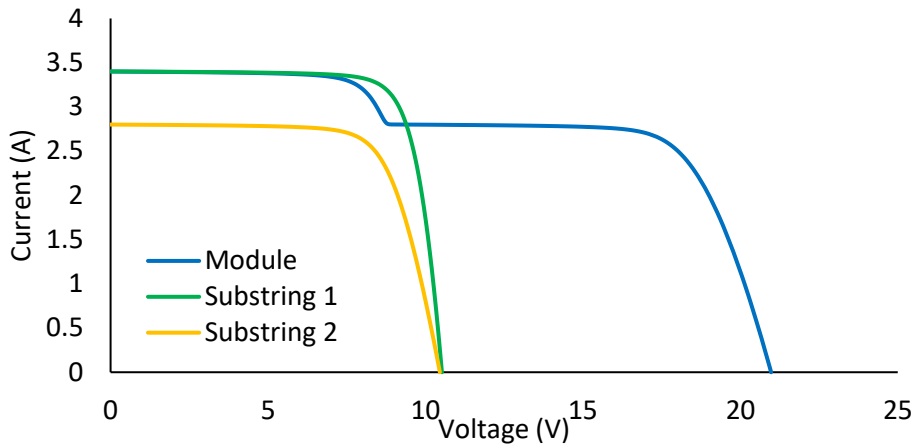
Figure 4.23: I-V curves of the module and substrings, modelled in PVSim, simulating the operation of the monocrystalline module.

Table 4.3: Values of voltage, current and ΔT observed when resistance was varied.

TIR image	Resistance (Ω)	Voltage (V)	Current (A)	ΔT (°C)
A	0.0	0.00	3.4	33.9
B	4.0	10.8	2.9	26.6
C	8.0	16.7	2.4	14.4
D	10.0	17.9	1.8	4.7
E	12.0	18.5	1.4	0.3
F	∞	20.1	0.0	0.5

TIR = Thermal infrared, ΔT = temperature difference

The I-V characteristics of substring SS 2, show that the substring is underperforming when compared to substring SS 1, since substring SS 2 produced less current than SS 1 for voltages 0-10 V due to more underperforming cells contained in substring SS 2 than in substring SS 1 and these are then observed as being abnormally hot. The current mismatch between substring SS 1 and substring SS 2 is more significant for voltages less than 8 V and the open circuit voltages of substring SS 1 and substring SS 2 are slightly different since substring SS 2 contains more defective cells than substring SS 1, as discussed below. The current mismatch between the substrings caused a step in the I-V curve of the module, thus indicating an active bypass diode across substring SS 2 that was forced into a forward

bias to lessen the effect of mismatch, and hence the heating effect of poorer performing cells in substring SS 2. TIR image C in Figure 4.22 corresponds to the MPP of the module and when shifting towards I_{SC} along the I-V plot of the module, more abnormally hot cells appear in TIR images A and B which were captured when the module was generating 3.4 A and 2.9 A, respectively. When the module's operational point was adjusted to a lower voltage and larger current of 3.4 A, many underperforming cells dissipated more heat causing a higher operational temperature due to a significant/large current mismatch between bad and good cells. Contrary to this, the current mismatch is minimal when shifting towards V_{OC} from the MPP along the I-V curve of the module with fewer underperforming cells as shown on TIR images D and E. These cells were also not as abnormally hot as when imaged close to I_{SC}. When the cells are generating equal currents, the bad and good cells appear to operate at uniform temperature as shown on TIR image E when all the cells were producing 1.4 A, operating at about 39 °C. TIR image F in Figure 4.22 was taken when the module was open-circuited and it shows almost all the cells appearing to be warm, at around 44 °C, since more incident radiation was absorbed and no electrical energy was delivered.

Figure 4.24 shows the visual and TIR images together with the EL image of the module. It is clear that the underperforming cells were damaged, as revealed by the EL image of the module, and the visual image shows no optical impediment on the affected cells.
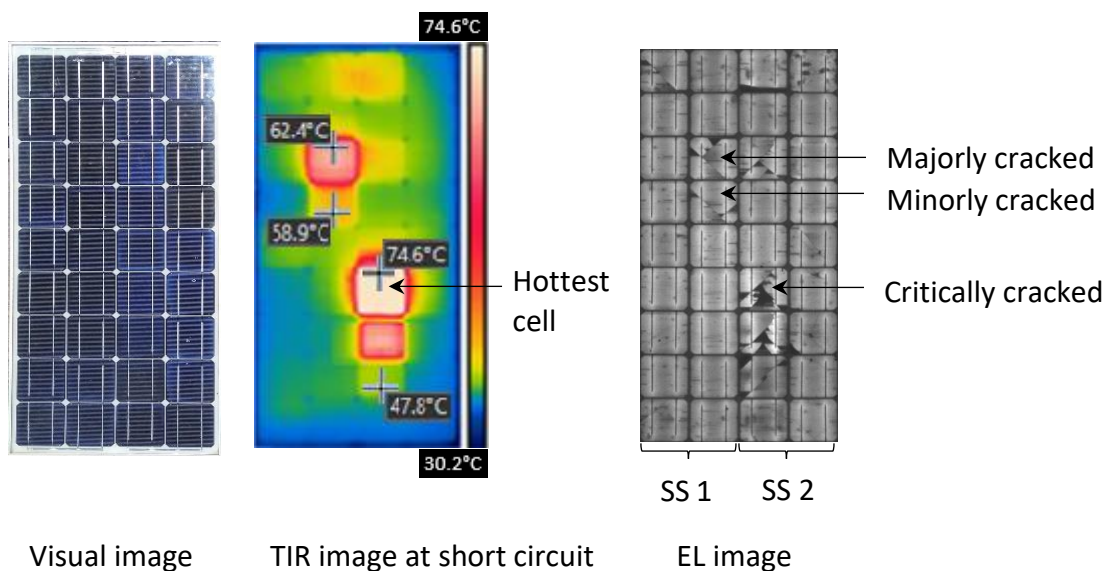
Figure 4.24: Visual, thermal infrared and electroluminescence images of the monocrystalline photovoltaic module. TIR = Thermal Infrared, EL = Electroluminescence, SS = substring

The abnormally hot cells in the TIR image, in Figure 4.24, correspond to the damaged cells which are judged by the following criteria, critical (> 20% cell area disconnected), major (10 ≤ 20% cell area disconnected) and minor (< 10% cell area disconnected). The critically cracked cell corresponds to the hottest cell that operated at 74.6 °C, at I_{SC}. The operating temperature of the defective cells abnormally increases with the cell area affected and is due to an increase in current mismatch caused by reverse biasing and resistive heating when more cell fingers are disconnected from the busbars. This is reflected by the selected cells, cells of interest, with critical, major and minor damages having operational temperatures of 74.6, 62.4 and 58.9 °C, respectively, at I_{SC}. The critically damaged cell still shows its abnormal thermal signature on TIR image D in Figure 4.22, even at minimal current mismatch when the module was generating 1.8 A, thus also revealing the severity of cell part disconnections which impact on generation and flow of current. Uncritically cracked cells having major and minor damages were abnormally hot when the module was generating a large current of 3.4 A (close to I_{SC}) and was forced to operate as good cells, due to minimal current mismatch, when the module was producing 1.8 A and appeared as normal cells under TIR imaging.

Cracks can cause a current mismatch but if the cell fingers or busbars are not interrupted then the cell will perform normally [16][127], otherwise, the cracked cells will be forced to abnormally heat up if a significant current mismatch is created. If the module is in the field, the cracks can develop due to harsh environmental conditions and the continual thermal cycling of the hot cells will force the module to degrade quickly. Therefore, a clear picture of the intrinsic operations of PV cells when generating electrical power in the field is crucial to making informed decisions during the maintenance of the PV modules.

4.3.4 Dynamics of thermal signatures on operational polycrystalline silicon PV module under varying load

The influence of changing load conditions on electrical and thermal measurements of the polycrystalline silicon PV module (SW 240 poly) is discussed in this section. The results were obtained after following an experimental procedure in Section 3.5, when the operational voltage of the module was changed by varying the load resistor. The module's specifications (SW 240 poly, Module D) are shown in Table 3.1, Section 3.1. The dynamics of abnormal thermal signatures as seen in Figure 4.22 in Section 4.3.3 were similarly observed when the module (SW 240 poly, Module D) was TIR imaged at different operational load conditions.

The TIR images were recorded concurrently with module current and voltage measurements of 60 individual cells. Figure 4.25 shows the module current and cell voltages as well as the thermal characteristics of the polycrystalline module that were recorded when the module's operational voltage was varied from close to V_{OC} to zero volts by changing the resistive load. When the module operated between voltages that are close to V_{OC} (33.5 V) and V_{MP} (27 V) each module cell operated at almost equal voltages and all the cells operate at nearly uniform temperatures as shown in TIR images (a) and (b) in Figure 4.25. As the module's operational voltage is further reduced to 24 V, 18 V and 0 V, the module's current increases marginally to the short circuit current (I_{SC}) of 7.8 A. Since the same current passes through each cell in a substring, some mismatched cells are forced to operate at lower voltages or in reverse bias. In doing so, some cells change from producing (positive voltage) to dissipating (negative voltage) power. The reverse-biased cells dissipate power and appear abnormally hot as shown on TIR images (c), (d) and (e). Figure 4.25 shows the cell voltages being almost equal (matched) between V_{OC} and V_{MP} to being very unequal (mismatched) as the module voltage drops to zero (I_{SC}). At the same time, the number of the hot cells increases on TIR images (c) to (e) and corresponds to the number of the reverse-biased cells with negative operational (reverse bias) voltages shown in Figure 4.25. The TIR images (c) to (e) also show an increase in the operating temperature of the mismatched cells, thus indicating that severe mismatch is occurring when the module operates close to short circuit conditions. A change in load conditions from big resistive loads of > 10 Ω to small resistive loads of < 5 Ω, caused the operational current and voltage points of the module and individual cells to change, resulting in severe mismatch which influenced the dynamics of the abnormal thermal signatures. The EL images of the module are shown in Figure 4.8 and reveal minorly cracked cells 1, 20, 47 and 52 without disconnected cell parts, thus the EL features are insignificant to cause the abnormal thermal signatures.
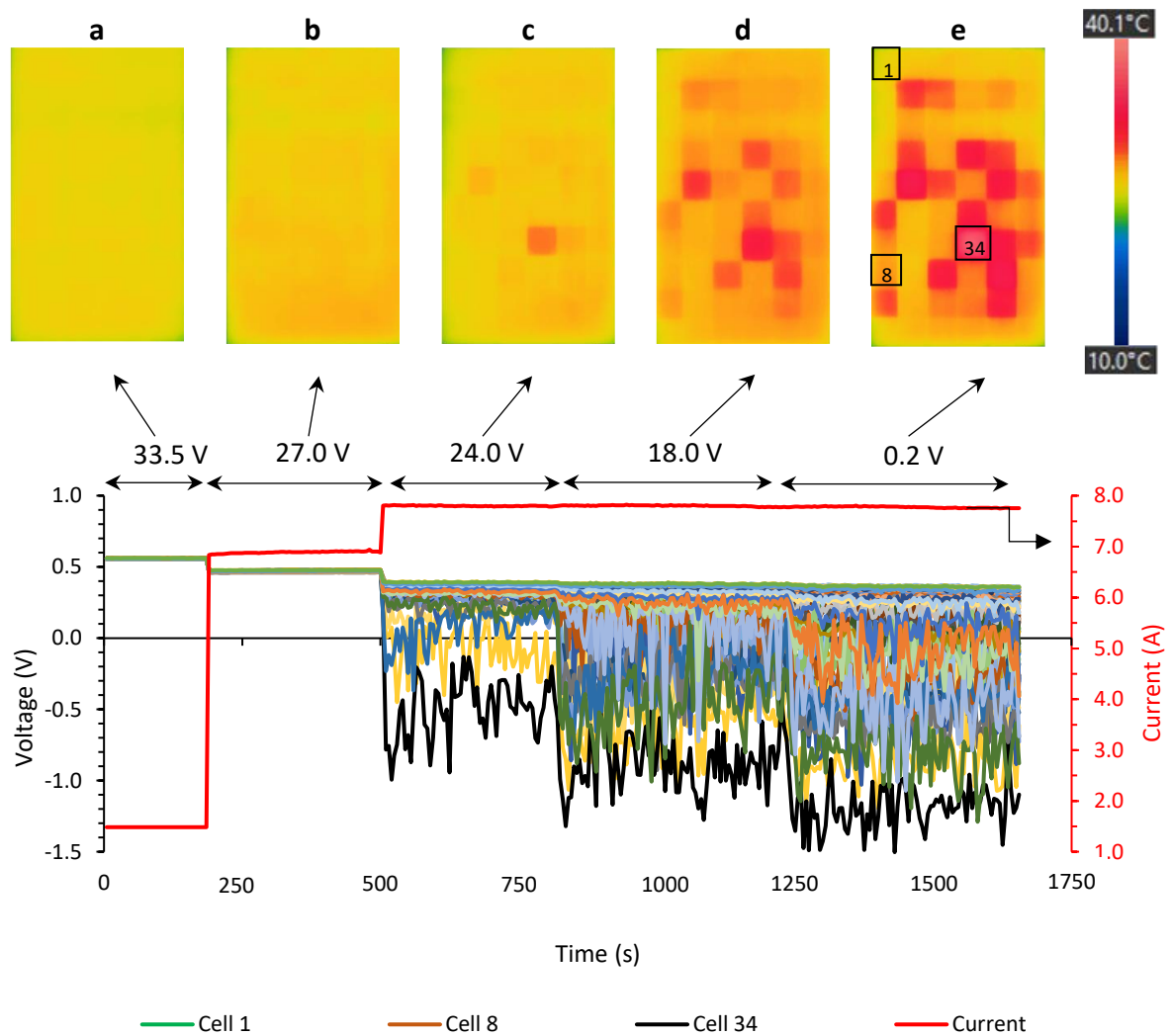
Figure 4.25: Module current, cell voltages and thermal characteristics of a polycrystalline PV module recorded under different operational voltages.

Figure 4.26 shows the thermal images of the polycrystalline PV module that were recorded at different operational current and voltage points, with and without partial shading on cell 30. The TIR images are linked to the I-V curve of the module which was taken under no shading conditions. The operational voltages were changed by varying the load resistor to observe the effect of changing the module's operational points on the abnormal thermal signatures when cell 30 was unshaded and when the cell was under a shading level of 4 %. Figure 4.26(a) shows several abnormal hot cells, in a patchwork pattern, on the TIR image taken when the module was unshaded and operating close to I_{SC}, 0.2 V, 7.1 A. When a shading level of 4% was applied on cell 30, the shaded cell become abnormally hot while the rest of the cells in the substring containing cell 30 appeared normal on the TIR image (g). The number of the hot cells reduce when the module's operational voltage increased to ~ V_{OC}, along the I-V curve, as shown on

TIR images (b), (c), (d), (e) and (f) when the module is unshaded and their corresponding TIR images (h), (i), (j), (k) and (l) when cell 30 is partially shaded. The reduction in the number of hot cells is due to minimal current mismatch when the module's operational voltage is > V_{MP} and closer to $V_{OC,}$ as explained earlier. The operational temperature of cell 30 decreased with an increase in the module's operational voltage due to a reduction in current mismatch, as explained in Section 4.2. When there is no current mismatch, the cells operate with uniform temperature as shown in TIR images (e), (f) and (l), thus no cell is reverse biased. TIR image (l) shows a hot strip on cell 30 due to the different emissivity of the module glass and the opaque shading material. Thus, as previously discussed, a current mismatch between good and bad cells can easily occur when the module's operational voltage is less than V_{MP} and closer to 0 V than when the voltage is greater than V_{MP} and closer to V_{OC}.
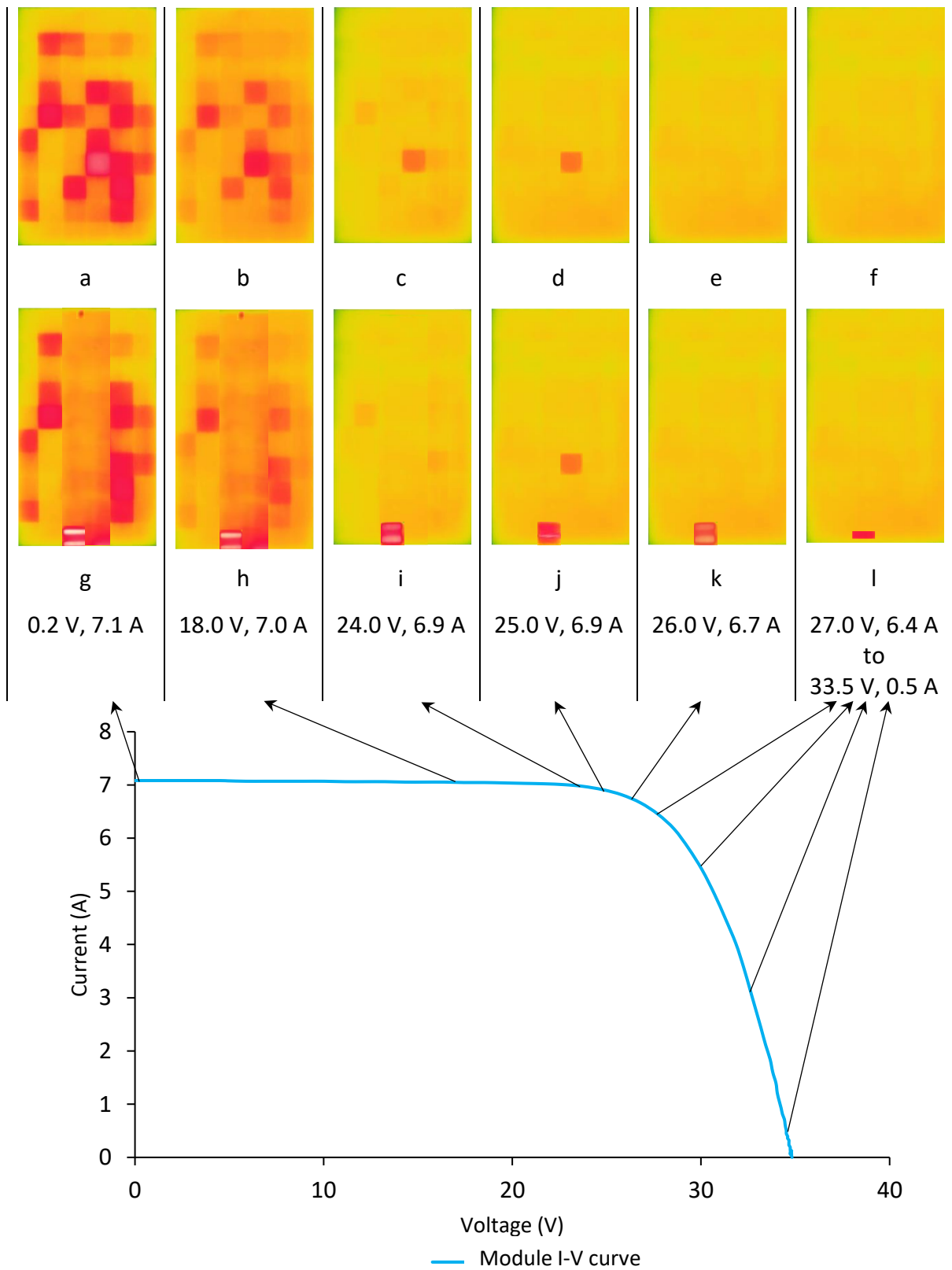
Figure 4.26: Thermal images of the crystalline PV module captured when cell 30 was unshaded (a-f) and shaded (g-l) at different operational current and voltage points of the module.

Figure 4.27 shows the behaviour of voltages of three representative cells (1, 8 and 34) when the cells operate with voltages lesser than V_{MP}. The cells are highlighted on TIR image (e) in the figure. The operational voltage of cell 1 is positive and almost constant as it produces and contributes power while operating at normal temperature. The voltage of cell 8 fluctuates around zero volts and changes randomly between positive and negative voltages. It randomly changes from producing to dissipating power and appears warm on TIR image (e) in Figure 4.25. The operational voltage of cell 34 fluctuates in the negative and appears abnormally hot on TIR image (e) in Figure 4.25. Cell 1 operates at normal temperature while cell 8 is slightly warmer and cell 34 is at abnormally elevated temperature.
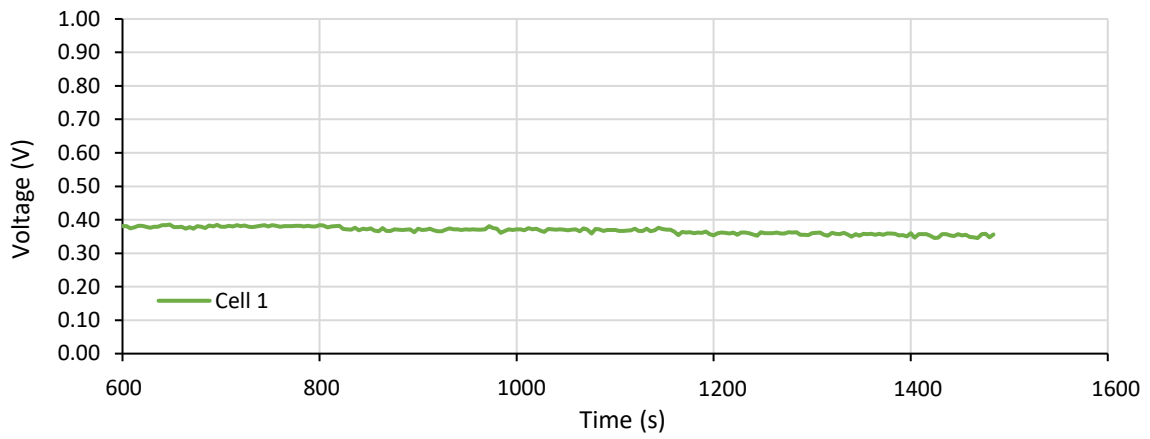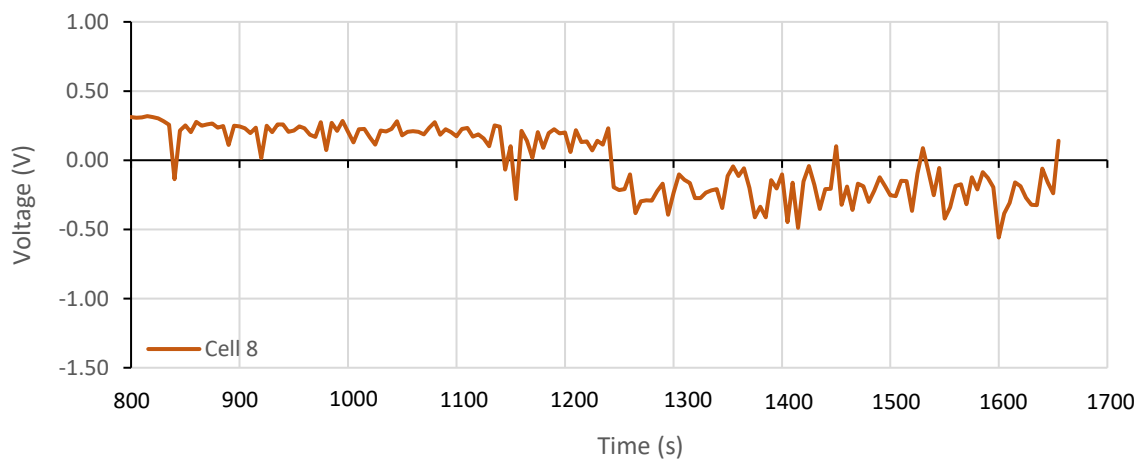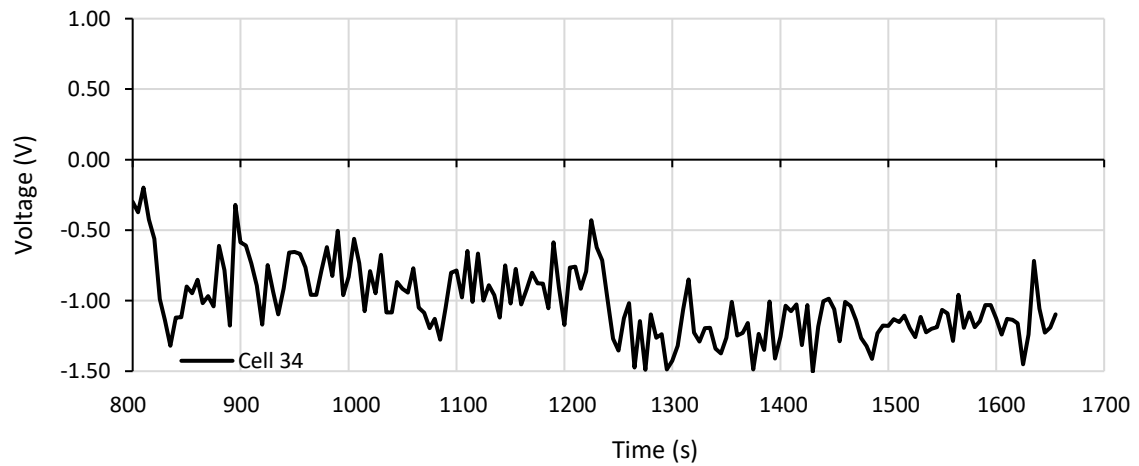
Figure 4.27: Three cells having different operational voltages: (a) positive voltage and generating power, (b) random change between positive and negative as the cell produce and dissipate power (c) negative voltage and dissipating power.

The random and relatively large voltage fluctuations of the cell voltages can be linked to very small variations in the I-V characteristics of the individual cells caused by amongst other factors, small variations in irradiance. Figure 4.28 illustrates the change in cell operational points as the module current varies. The representative I-V curves of cells 1, 8 and 34 are I-V curves A, B and C, respectively, shown in Figure 4.28.

4.3.5 Effects of varying irradiance on operational current and voltage of cells

This section illustrates and discusses the behaviour of operational current and voltage points of the polycrystalline silicon module (SW 240 poly, Module D) under constant load conditions and changing irradiance. The trends of voltages of cells 1, 8 and 34 shown in Figure 4.27 are explained.

The module current and I-V characteristics of the cells change non-uniformly with varying irradiance. The relative change of the module current to the I-V curves of individual cells is small. When the module current change, due to a change in irradiance, the operational points of cells A, B and C shift as indicated in Figure 4.28. The shift in the operational point of cell A results in a marginal change in the operational voltage of the cell. However, the operational voltages of cells B and C change significantly with changes in their operational points. The operational voltage of cell B changes between positive and negative with the change in operational point. The operational voltage of cell C shifts significantly and stays negative when the operational point shifts.
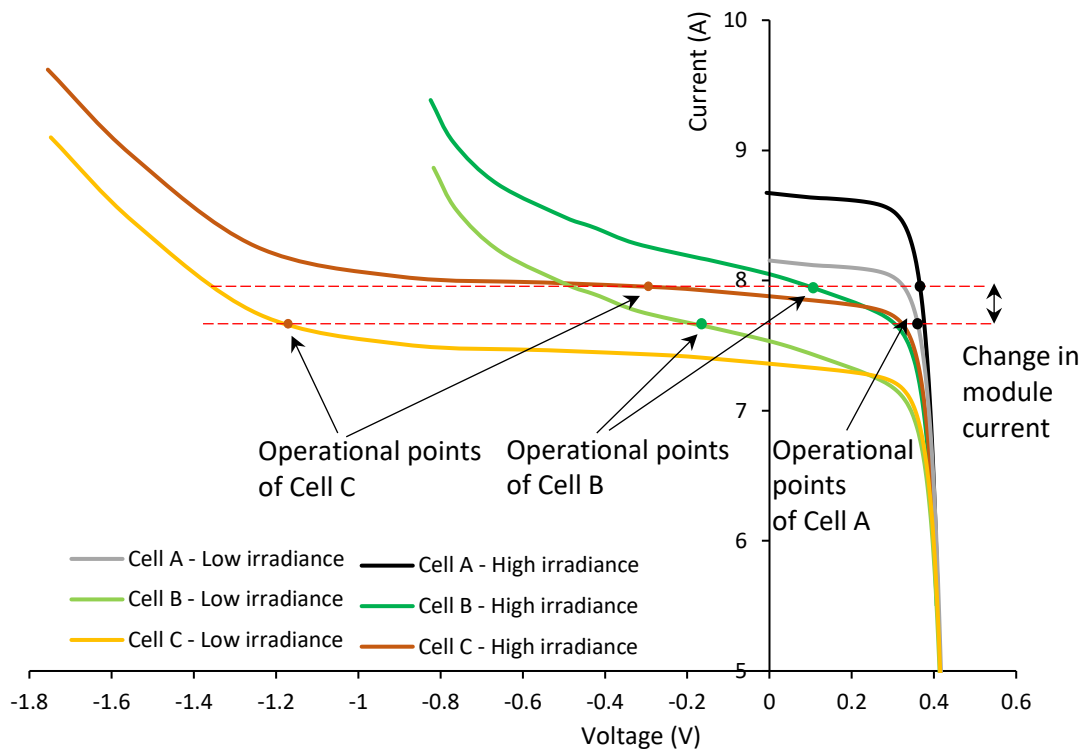
Figure 4.28: I-V curves of three mismatched cells A, B and C indicating a shift in operational voltages when module current changes.

Figure 4.29 illustrates the shift in operational voltage of a PV module due to a change in the resistive load (load lines A and B) and irradiance. When the resistive load is reduced, the operational voltage shifts towards I_{SC} and the module operates on the horizontal section of the I-V curve, load line A. Under this load condition, fluctuations in irradiance will manifest in larger voltage fluctuations, V_{A1} to V_{A2}, compared to, V_{B1} to V_{B2}, when the load is large and the module operates on the vertical section of the I-V curve, load line B.
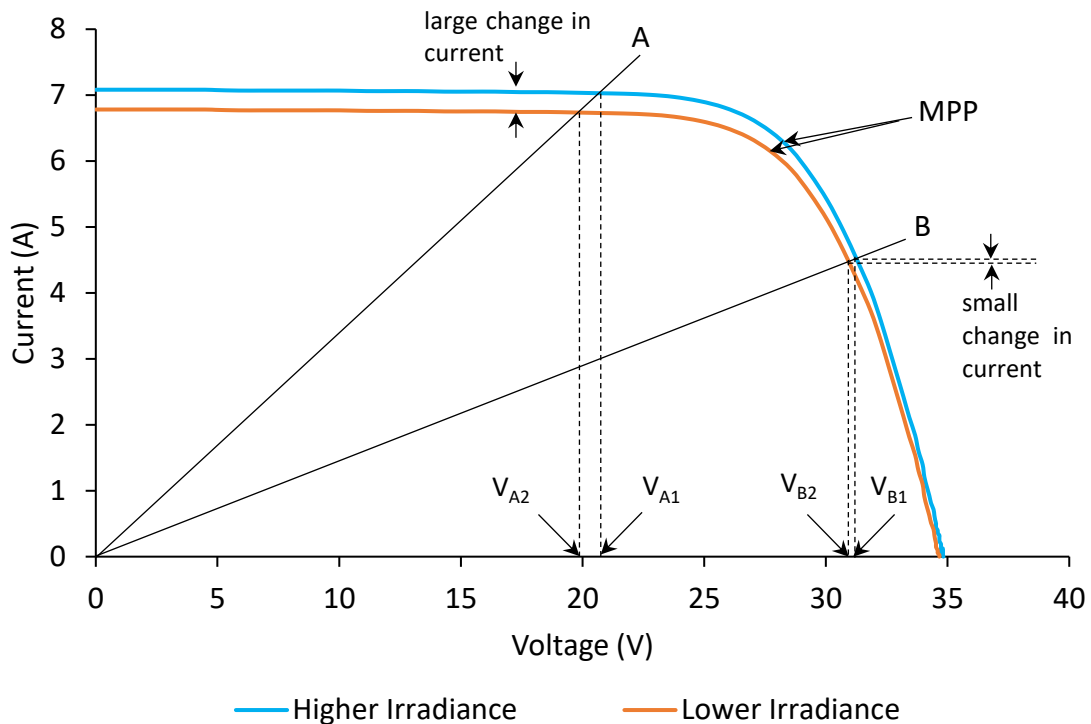
Figure 4.29: I-V curves of a PV module under changing load conditions (load lines A and B) and varying irradiance. The effect of change in irradiance on the operational voltages when the module operates on load lines A and B is indicated.

Cell mismatch is usually caused by defective cells or external cell anomalies such as partial shading [16][18][127], however, the cell mismatch causing the random fluctuations in cell voltages could be due to non-homogeneity in the cell material. Non-homogeneous cell material can be caused by intrinsic manufacturing deformities and impurities which can result in the affected cells having different I-V parameters even when subjected to the same operational conditions.

Other studies focus on the classification of TIR images [16][41][128][129] for a better understanding of the abnormal thermal signatures to gather information which can be useful in quantification of power loss associated with the abnormal thermal signatures. The quantification of the power loss due to mismatched cells has been under study as back as 1995 [130], and is still ongoing [131][132] for improved maintenance and longevity of PV modules. However, as highlighted earlier, the interpretation of the TIR images is still not a straightforward thing. Therefore, this study adds valuable insights into the operation of crystalline silicon PV modules, and substrings down to the cell level for advancing the understanding of the dynamics of current and voltage operational points and abnormal

thermal signatures and can improve the operation and maintenance systems of the PV modules. The results of this study show that changing the operational conditions influence the current-voltage operating point of modules, substrings and individual cells, such that cells that underperform show their abnormal thermal signature, on TIR images, under certain operational conditions. The bad cells easily show their abnormal thermal signatures when the operational voltage is $< V_{MP}$ and closer to I_{SC}, that is when a significant current mismatch is created between good and bad cells, unlike when the operational voltage is $> V_{MP}$, when there is minimal current mismatch. The conditions under which TIR images are taken have to be noted for better decisions on the TIR measurements. In addition to the standard guidelines for TIR imaging of PV modules such as calm environmental conditions, clear sky with irradiance level of more than $600 \, W.m^{-2}$, emissivity and angle of capture listed in Section 2.6.6.1, it is beneficial to capture the TIR images when the operational voltage is $< V_{MP}$ and when the modules deliver current close to I_{SC} so that even minor cell abnormalities will show their abnormal thermal signature and be identified on TIR images.

4.4 Summary

The effects of different operational conditions on I-V and thermal characteristics of crystalline PV modules were presented and discussed. The abnormal thermal signatures are classified according to cell anomalies in Section 4.1, while Sections 4.2, 4.3, and 4.4 discuss the dynamics of the thermal signatures in crystalline PV modules under different operational conditions. The partial shading of cells influences the current mismatch in substring cells as it causes the affected substring to produce less current than a normal operating substring in the module when the whole cell operates at an elevated temperature due to reverse biasing and abnormal resistive heating. The bad cells contained in the affected/shaded substring will not show the abnormal thermal signature and are seen as good cells on TIR images due to minimal current mismatch. The dynamics of thermal signatures seen on TIR images of crystalline PV modules operating under partial shading, including soiling, can be misinterpreted and mislead PV plant operators about the real cause of underperforming modules. The operational conditions of modules influence the reverse bias voltage of an underperforming cell which in turn affects the activation of the bypass diode, which is crucial in the operation of crystalline modules. The operational conditions which result in the small/light cell shading activating a bypass diode will cause significant power loss (about one-third of a module's power) as the

bypass diode minimises the heating effects on the shaded cell. If the conditions result in large/heavy cell shading to activate the bypass diode, then the continued localised overheating on the shaded cell can further damage the module and causes a risk of fire.

Varying irradiance, output power and load conditions can also influence the electrical and thermal characteristics of the crystalline silicon PV cells. The operational conditions which cause the module's operating point to be on the horizontal section of the I-V curve (closer to I_{SC}) will result in the bad cells being heavily mismatched and appearing abnormally hot on TIR images. When the operational point is on the vertical section of the I-V curve (closer to V_{OC}), there will be a minimal mismatch and the module can operate and appear normally, with uniform temperature distribution, on TIR images. TIR images that are taken on clean modules delivering current close to I_{SC} will show the abnormal thermal signatures caused by minor cell anomalies due to significant current mismatch created, unlike when the module is delivering lower current. This can be implemented when carrying out TIR imaging so that all cells with abnormalities can be identified on TIR images.

Chapter 5

Conclusions

This study investigated the dynamics of abnormal thermal signatures and electrical characteristics of crystalline silicon photovoltaic (PV) cells and modules under different operational conditions. The investigation includes an analysis of the effects of varying shading, irradiance and output power at different load conditions, as may be experienced in the field, on the thermal and electrical characteristics of the cells and modules. PV cells can underperform and appear abnormally hot on TIR images due to (i) inherent mismatch due to manufacturing faults of the cells and (ii) external cell mismatch due to environmental conditions. The in-field operational conditions of the modules, such as a change in load conditions, varying irradiance and partial soiling and shading, can cause a current mismatch between series-connected cells and modules, thus influencing the operating current and voltage of the individual cells and modules. The variation in operating voltage and current may result in the dynamic behaviour of abnormal thermal signatures where their distribution and appearance change. Thermal Infrared imaging (TIR) is widely applied, especially in large PV plants, as a metric for identifying mismatched cells. However, the accurate judgement and interpretation of TIR images is still a major challenge. The main focus of this study was, to understand the behaviour of mismatched cells under different operational conditions and their influence on the thermal and electrical characteristics. The expectation is that this study will add value to operation and maintenance practitioners to correctly interpret TIR results to accurately identify potential problems in the crystalline Si PV plants under their control.

TIR images of crystalline (mono and poly) silicon PV modules that were studied were recorded together with current and voltage measurements of cells and modules at a latitude tilt angle at the Outdoor Research Facility (ORF) at Nelson Mandela University, Port Elizabeth in South Africa while generating power under different cell shading levels, load conditions, irradiance levels and output power. All the relevant meteorological data, such as irradiance was monitored by the weather station at the ORF. Visual inspections, current-voltage (I-V) curve characteristics and Electroluminescence (EL) imaging were also carried out on the

PV modules to check for any inherent performance and cell irregularities causing the abnormal thermal signatures that were observed.

It was observed that when a polycrystalline PV module (YL250P-29b poly) was shaded partially by (<10%) soiling of one good cell in each substring, the bad cells that were cracked, PID affected or of poor quality does not appear as abnormally hot cells on TIR images. These bad cells could therefore easily be missed since they operated and appeared as normal cells on the TIR images while the partially shaded cells heated up and operated at elevated temperatures. On this module, and also on a monocrystalline PV module (AP-6105 mono), it was also observed that a cracked cell with a large electrically isolated cell area, will cause a significant current mismatch and operate at a higher temperature than a cell with a small, isolated cell area.

The dynamics of the abnormal thermal signatures were also observed on a module string when TIR images of a 1.6 kW array, containing nine series and parallel connected monocrystalline silicon PV modules (SW-175 mono), were recorded when one good cell in one of the modules was partially soiled. Again, it was shown that the TIR images of a partially soiled module can be misleading during PV module inspections in the field since certain non-shading related cell anomalies did not appear. Therefore, TIR imaging should be carried out on unsoiled and unshaded PV modules to avoid misleading decisions.

Partial cell shading of between 4% to 100%, affected the normal operation of a polycrystalline silicon PV module (SW 240 poly) with three cell substrings, by influencing the current generation and operating voltages of the cells in the module. The operational voltages of the individual cells showed an inherent mismatch with an approximately 4% difference in the highest and lowest cell voltages when the cells were operating under similar, normal conditions. A shading level of 4% on one cell resulted in the shaded cell operating at a reduced positive voltage. Increasing the shading levels from 8% up to 100% caused the cell to operate at negative (reverse) voltages while the whole cell appeared abnormally hot on the TIR images. The cell's operational temperature increased for shading levels from 8% to 40% and decreased for shading levels from 50% to 100% when the bypass diode of the substring containing the shaded cell gets activated, allowing the module's current to bypass the substring. The shading level which causes the activation of the bypass diode is crucial for understanding the operation of the crystalline PV module since, its onset results in about one-

third of the module's power being lost but at the same time, also reducing the overheating of the shaded cell by minimising the current through the shaded cell. The bypass diode requires a certain forward bias voltage to be activated. The external load determines the current and voltage operating point of a module which in turn affects the bias voltage across the bypass diode. The external load thus also determines the onset of the bypass diode activation and thus also the level of protection against overheating of mismatched cells.

The distribution and appearance of hot areas (including hot cells and junction boxes) in TIR images are affected by the change in the individual cells and module's current and voltage operating point.

When the operational voltage is < V_{MP} and closer to 0 V (or I_{SC}), along the I-V curve, there is a greater likelihood for the voltage of the underperforming and mismatched cells and substrings to get reduced and even become reverse biased and appear as hot cells on TIR images. When the operational voltage is > V_{MP} and closer to V_{OC}, the current mismatch from underperforming cells and substrings is minimal and the voltage of the cells and substrings remains similar. Therefore, it is beneficial for PV modules that may have underperforming cells or substrings to operate at voltages that are higher than V_{MP} where minimal current mismatch occurs. When the modules operate at < V_{MP}, abnormal thermal signatures will always appear on modules containing underperforming cells and substrings. Abnormal hot areas can impact power generation and also quickly degrade the encapsulation materials or junction boxes in modules.

In addition to the typical guidelines for carrying out TIR imaging inspections, taking TIR images on crystalline silicon PV modules operating closer to short circuit conditions is beneficial as underperforming cells and substrings can certainly be identified. In this study, the operational current and voltage points of the modules and cells were varied by changing the resistance of a load. The operational point of module strings in PV plants is determined by the maximum power point trackers of the invertors. As a recommendation to aid the identification of underperforming modules, substrings and cells in TIR imaging inverters can be designed to incorporate a trigger which can be activated, to force the operational voltage of the modules to be < V_{MP}, while TIR imaging is carried out.

The study investigated the relative changes in the operational electrical and thermal characteristics of crystalline modules and shows additional insights into the dynamic nature of abnormal thermal signatures. This study also contributes to the improvement of the identification of underperforming cells and substrings through TIR imaging and I-V curve measurements as well as the correct interpretation of the results of the measurements.

Summary of recommendations

This study advances the understanding of the dynamics of the operational points on the current-voltage curve and the resulting thermal signatures. This will improve the interpretation TIR imaging of PV plant inspections using crystalline PV modules. In this study it is shown that the crystalline cells having anomalies can easily be identified on TIR images when the modules are clean and when the operational voltage is reduced (closer to Isc on the I-V curve), therefore inverters can be designed to incorporate a function which can reduce the operational voltage of the module string to highlight inherent anomalies on TIR images. When cells in PV modules are mismatched, the overheating of individual cells may be minimised by operating closer to V_{OC}. Inevitably, this will lead to a reduction in power but can reduce the detrimental effects of overheating.

References

[1]   REN21, Global Status Report, A Comprehensive Annual Overview of the State of Renewable Energy, Investment flows, [Online]. Available: https://www.ren21.net/gsr-2021/chapters/chapter_05/chapter_05/ (accessed 22 April 2022).

[2]   M. Moner-Girona, M. Solano-Peralta, M. Lazopoulou, E. K. Ackom, X. Vallve, and S. Szabó, "Electrification of Sub-Saharan Africa through PV/hybrid mini-grids: Reducing the gap between current business models and on-site experience," *Ren. and Sust. Ener. Rev*. 2018, doi: 10.1016/j.rser.2018.04.018.

[3]   IRENA (2019), Future of Solar Photovoltaic: Deployment, investment, technology, grid integration and socio-economic aspects (A Global Energy Transformation: paper), International Renewable Energy Agency, [Online]. Available: https://www.irena.org//media/Files/IRENA/Agency/Publication/2019/Oct/IRENA_Future_of_wind_2019.pdf. ISBN 978-92-9260-156-0, (accessed 26 September 2021).

[4]   ESMAP, "Global Photovoltaic Power Potential by Country," Washington, DC, 2020. doi: 10.1596/34102.

[5]   IRENA (2021), Installed capacity Trends, International Renewable Energy Agency, [Online]. Available: https://www.irena.org/solar, (accessed 26 September 2021)

[6]   IRENA (2021), The Renewable Energy Transition in Africa, International Renewable Energy Agency, [Online]. Available: https://www.irena.org/publications/2021/March/The-Renewable-Energy-Transition-in-Africa, (accessed 13 October 2021).

[7]   R. Gumbo, L. T. Katsvairo, and K. Asai, "State of Photovoltaic home systems in Zimbabwe," in *3rd World Conf. on Phot. Ener. Conv. Proc.*, Osaka, 11-18 May 2003, WCPEC-3 Organizing Committee, 2003, pp. 2640–2643.

[8]   S. Bawakyillenuo, "Deconstructing the dichotomies of solar photovoltaic (PV) dissemination trajectories in Ghana, Kenya and Zimbabwe from the 1960s to 2007," *Ener. Pol.*, vol. 49, pp. 410–421, 2012. DOI: 10.1016/j.enpol.2012.06.042.

[9]   J. Shilpi and P. K. Jain, "The rise The of Renewable Energy implementation using the heat demand-outdoor a long-term district heat demand forecast," *Ener. Proc.*, vol. 143, pp. 721–726, 2017. doi.org/10.1016/j.egypro.2017.12.752.

[10]   A. Eberhard and R. Naude, "The South African Renewable Energy Independent Power Producer Procurement Programme: A Review and Lessons Learned," *J. Ener. S. Africa*, vol. 27(4), pp. 1-14, 2016. doi.org/10.17159/2413-3051/2016/v27i4a1483.

[11]   The World Bank, Source: Global Solar Atlas 2.0. Solargis.com. (2019). [Online]. https://solargis.com/file?url=download/World/World_PVOUT_mid-size-map_lang-FR_160x95mm-300dpi_v20200529.preview.jpg&bucket=globalsolaratlas.info, (accessed 20 August 2021).

[12]   EnergyCapital&Power, "Top 10 Solar Power Plants in Africa," [Online]. Available: https://energycapitalpower.com/top-10-solar-power-plants-in-africa/," (accessed 18 May 2022).

[13]   My Broadband Trusted in Tech, "Biggest solar farm in South," [Online]. Available: Africahttps://mybroadband.co.za/news/energy/428714-biggest-solar-farm-in-south-africa.html, (accessed 18 May 2022).

[14]   C. Ferrara and D. Philipp, "Why do PV modules fail?," *Ener. Proc.*, vol. 15, pp. 379–387, 2012, doi: 10.1016/j.egypro.2012.02.046.

[15]   S. Bowden and C. Honsberg, "PVCDROM | PVEducation." [Online]. Available: http://pveducation.org/pvcdrom, (accessed 23 August 2021).

[16]   M. Köntges, S. Kurtz, C.E. Packard, U. Jahn, K. Berger, K. Kato, T. Friesen, H. Liu and M. Van Iseghem, (2014). Review of failures of photovoltaic modules, IEA-Photovoltaic Power Systems Programme, IEA-PVPS, 2014. https://iea pvps.org/wp content/uploads/2020/01/IEAPVPS_T13 01_2014_Review_of_Failures_of_Photovoltaic _Modules_Final.pdf.

[17]   A. Al Mansur, M. Ruhul Amin, and K. K. Islam, "Performance comparison of mismatch power loss minimization techniques in series-parallel PV array configurations," *Ener.*, vol. 12, no. 5, 2019, doi: 10.3390/en12050874.

[18] M. Vumbugwa, J. L. Crozier McCleland, E. E. van Dyk, F. J. Vorster, and T. J. Serameng, "Effects of current mismatch due to uneven soiling on the performance of multi-crystalline silicon module strings," *J. Ener. S. Africa*, vol. 31, no. 1, pp. 62–72, 2020, doi: 10.17159/2413-3051/2020/v31i1a7571.

[19] G. C. Lee, G. W. Shin, R. L. Jong, G.H. Kang, J.Y. Chul, M.H. Hwang, S. H. Chang, K. S. Whan, "Analysis of electrical and thermal characteristics of PV array under mismatching conditions caused by partial shading and short circuit failure of bypass diodes," *Ener.*, vol. 218, p. 119480, 2021, doi: 10.1016/j.energy.2020.119480.

[20] U. Jahn, M. Herz, M. Köntges, D. Parlevliet, M. Paggi, I. Tsanakas, J. S. Stein, K. A. Berger, S. Ranta, R. H. French, M. Richter and T. Tanahashi, (2018). Review on Infrared and Electroluminescence Imaging for PV Field Applications, IEA-Photovoltaic Power Systems Programme, IEA-PVPS. https://iea-pvps.org/wp-content/uploads/2020/01/Review_on_IR_and_EL_Imaging_for_PV_Field_Applications_by_Task_13.pdf.

[21] R. Ahmad, A. F. Murtaza, H. S. Ahmed, U. S. Tabrez and S. Olalekan, "An analytical approach to study partial shading effects on PV array supported by literature," *Renew. Sust.. Ener. Rev*, vol. 74, pp. 721–732, 2017, doi: 10.1016/j.rser.2017.02.078.

[22] S. Saravanan and N. B. Ramesh, "Maximum power point tracking algorithms for photovoltaic system – A review," *Ren. and Sust. Ener. Rev.*, vol. 57, pp. 192–204, 2016, doi: 10.1016/j.rser.2015.12.105.

[23] S. Sengar, "Maximum Power Point Tracking Algorithms for Photovoltaic System : A Review," *Res. India Publ.*, vol. 4, no. 2, pp. 147–154, 2014.

[24] Z. Zandi and A. H. Mazinan, "Maximum power point tracking of the solar power plants in shadow mode through artificial neural network," *Complex Intell. Syst.*, vol. 5, no. 3, pp. 315–330, 2019, doi: 10.1007/s40747-019-0096-1.

[25] K. Kurokawa, "Realistic values of various parameters for PV system design," *Ren. Ener.*, vol. 15, no. 1, pp. 157–164, 1998. doi: 10.1016/S0960-1481(98)00144-X.

[26]   J. Haney and A. Burstein, (2013) PV System Operations and Maintenance Fundamentals, solarabcs.org. [Online]. Available: http://www.solarabcs.org/about/publications/reports/operations-maintenance/pdfs/SolarABCs-35-2013.pdf.

[27]   N. Tyutyundzhiev, K.Lovchinov, F. M. Moreno, J. Leloux, and L. Narvarte, "Advanced PV modules inspection using multirotor UAV," in *31st EUPVSEC Proceedings*, 14-18 September, Hamburg, 2015.

[28]   M. Aghaei, P. B. Quater, F. Grimaccia, S. Leva, and M. Mussetta, "Unmanned Aerial Vehicles in Photovoltaic Systems Monitoring Applications," in *29th EUPVSEC Proceedings*, Amsterdam, 22-26 September, 2014.

[29]   M. A. Munoz, M. C. Alonso-García, N. Vela, and F. Chenlo, "Early degradation of silicon PV modules and guaranty conditions," *Sol. Ener.*, vol. 85, no. 9, pp. 2264–2274, 2011, doi: 10.1016/j.solener.2011.06.011.

[30]   C. Buerhop, T. Pickel, M. Dalsass, H. Scheuerpflug, C. Camus, and C. J. Brabec, "aIR-PV-check: A quality inspection of PV-power plants without operation interruption," in *43th IEEE Photovoltaic Specialist Conference Proceedings*, Portland, 5-10 June 2016, Piscataway, NJ, IEEE, 2016 pp. 1–5, doi: 10.1109/PVSC.2017.8366365.

[31]   A. Singla, K. Singh, and V. K. Yadav, "Environmental effects on performance of solar photovoltaic module," in *2016 Biennial International Conference on Power and Energy Systems: Towards Sustainnable Energy (PESTSE)*, Bengaluru, 21-23 January 2016, IEEE 2016, pp. 1–6, doi: 10.1109/PESTSE.2016.7516480.

[32]   J. A. Tsanakas, L. Ha, and C. Buerhop, "Faults and infrared thermographic diagnosis in operating c-Si photovoltaic modules: A review of research and future challenges," *Renew. Sust. Ener. Rev.*, vol. 62, pp. 695–709, 2016.

[33]   C. Dunderdale, W. Brettenny, C. Clohessy and E. E. van Dyk, "Photovoltaic Defect Classification through Thermal Infrared Imaging using a Machine Learning Approach," *Prog. in Phot.: Res. and Appl.*, 28(3), 177–188, 2020.

[34]   G. Makrides, B. Zinsser, M. Norton and G. E. Georghiou, Performance of Photovoltaics Under Actual Operating Conditions, Chapter 9, Third Generations Photovoltaics, 2011, doi: 10.5772/27386

[35]   D. Atsu, I. Seres, M. Aghaei and I. Farkas, "Analysis of long-term performance and reliability of PV modules under tropical climatic conditions in sub-Saharan," *Ren. Ener.*, vol. 162, pp. 285–295, 2020. doi: 10.1016/j.renene.2020.08.021.

[36]   M. Bošnjaković and M. Stojkov, "Experimental Testing of PV Module Performance," *Tehnič. Glasnik*, vol. 15, no. 1, pp. 127–132, 2021. doi: 10.31803/tg-20200718142815

[37]   A. Fezzani, I. Hadj-Mahammed, A. Kouzou, L. Zaghba, S. Drid, M. Khennane, R. Kennel, M. Abdelrahem and M. Energy, "Efficiency of Multi-Technology PV Modules under Real Outdoor Conditions—An Experimental Assessment in Ghardaïa, Algeria," *Sust.*, vol. 14, 1771, 2022. doi: 10.3390/su14031771.

[38]   U. Hoyer, A. Burkert, R. Auer and C. Buerhop-Lutz, "Analysis of PV modules by electroluminescence and IR thermography," in *24th EUPVSEC Proceedings*, Hamburg, 21-24 Septeember, 2009.

[39]   C. Vodermayer, M. Mayer, M. Mayer and T. Müller, "First results – Correlation between IR images and electrical behavior and energy yield of PV modules," in *23rd EUPVSEC Proceedings*, Valencia, 1-5 September, 2008.

[40]   M. Vumbugwa, J. L. Crozier, E. E. van Dyk, F. J. Vorster and T. J. Serameng, "CORRELATION OF THERMAL IMAGING AND CURRENT-VOLTAGE MEASUREMENTS ON PV MODULE STRINGS," in *5th SASEC Proceedings*, Durban, 25-27 June, 2018.

[41]   S. Gallardo-Saavedra, L. Hernández-Callejo and O. Duque, "Analysis and characterization of PV module defects by thermographic inspection," *Revi. Fac. de Ingeniería Univ. de Antioquia*, 2019, 10.17533/udea.redin.20190517.

[42]   J. Chen, B. Cheng, X. Zhang, T. Long, B. Chen, G. Wang and D. Zhang, "A TIR-Visible Automatic Registration and Geometric Correction Method for SDGSAT-1 Thermal Infrared Image Based on Modified RIFT," *Remote Sens.*, 14, 1393. https://doi.org/10.3390/ rs14061393.

[43]   M. Aghaei, A. Gandelli, F. Grimaccia, S. Leva, and R. E. Zich, "Irreal-time analyses for pv system monitoring by digital image processing techniques," in *2015 International Conference on Event-based Control, Communication, and Signal Processing (EBCCSP)*, Krakow, Poland, 17 - 19 Jun. 2015, pp. 1-6, doi: 10.17533/udea.redin.20190517.

[44] J. A. Tsanakas, L. D. Ha, and F. Al Shakarchi, "Advanced inspection of photovoltaic installations by aerial triangulation and terrestrial georeferencing of thermal/visual imagery," *Ren. Ener.,* 102, 2017, 224-233, 2022, doi: 10.1016/j.renene.2016.10.046.

[45] S. Dotenco, M. Dalsass, L. Winkler, T. Würzner, C. Brabec, A. Maier and F. Gallwitz, "Automatic detection and analysis of photovoltaic modules in aerial infrared imagery," in *2016 IEEE Winter Conference on Applications of Computer Vision (WACV)*, Lake Placid, NY, USA, Jun. 2016, pp. 1-9, doi:10.1109/WACV.2016.7477658.

[46] A. W. Kandeal, M. R. Elkadeem, A. K. Thakur, G. B. Abdelaziz, R. Sathyamurthy, A. E. Kabeel, N. Yang and S. W. SharshirJohn, "Infrared thermography-based condition monitoring of solar photovoltaic systems: A mini review of recent advances," *Sol. Ener.*, 223, 33–43, 2021, doi.org/10.1016/j.solener.2021.05.032.

[47] P. Sánchez-Friera, M. Piliougine, J. Peláez, J. Carretero, and M. Sidrach de Cardona, "Analysis of degradation mechanisms of crystalline silicon PV modules after 12 years of operation in Southern Europe," *Prog. Phot. Res. Appl.*, vol. 19, no. 6, pp. 658–666, 2011.

[48] E. Kaplani, "Detection of Degradation Effects in Field-Aged c-Si Solar Cells through IR Thermography and Digital Image Processing," *Int. J. Photoenergy*, vol. 2012, pp. 1–11, 2012.

[49] J. A. Tsanakas, M. Karoglou, E. T. Delegou, P. N. Botsaris, A. Bakolas, and A. Moropoulou, "Assessment of the performance and defect investigation of PV modules after accelerated ageing tests," in *ICREPQ'13 Proceedings*, Bilbao, 20-22 March 2013.

[50] J. A. Tsanakas, L. Ha, C. Buerhop, "Faults and infrared thermographic diagnosis in operating c-Si photovoltaic modules: A review of research and future challenges," *Ren. and Sust. Ener. Rev.*, 62 (2016) 695–709, doi.org/10.1016/j.rser.2016.04.079.

[51] C. Geun Lee, W. G. Shin, J. Rok Lim, G. Hwan Kang, Y. Chul Ju, H. Mi Hwang, H. Sik Chang and S. Whan Ko, "Analysis of electrical and thermal characteristics of PV array under mismatching conditions caused by partial shading and short circuit failure of bypass diodes," *Ener.*, 218 (2021) 11948, doi.org/10.1016/j.energy.2020.119480.

[52]   G. Boyle, *Renewable Energy: Power for a Sustainable Future*, 3rd ed. Oxford: Oxford University Press, 2012.

[53]   J. P. Colinge and C. A. Colinge, *Physics of Semiconductor Devices*. New York: Kluwer Academic Publishers, 2002.

[54]   P. Hersch and K. Zweibel, *Basic Photovoltaic Principles and Methods*. Cole Boulevard: Solar Energy Research Institute, 1982.

[55]   D. A. Neamen, *Semiconductor Physics and Devices: Basic Principles*, 4th ed., New York: McGraw-Hill, 2012.

[56]   S. M. Sze, *Semiconductor Devices: Physics and Technology*, 2nd ed., New York: JOHN WILEY & SONS, INC., 2002.

[57]   K. Jäger, O. Isabella, A. H. M. Smets, R. A. C. M. M. van Swaaij, and M. Zeman, *Solar energy: Fundamentals, Technology and Systems*, 1st ed., Delft, Netherlands: Delft University of Technology, 2014.

[58]   D. Rusirawan and I. Farkas, Identification of model parameters of the photovoltaic solar cells," *Ener. Proc.*, vol. 57, 2014, pp.39 – 46.

[59]   M. T. Boyd, S. A. Klein, D. T. Reindl and B. P. Dougherty,"Evaluation and Validation of Equivalent Circuit Photovoltaic Solar Cell Performance Models," *Jour. of Sol. Ener. Eng.*, vol. 133, 2011, 021005. doi: 10.1115/1.4003584.

[60]   R. Gupta and D. Giribabu, "Matlab Simulation of Advanced MPPT Algorithm for Solar photovoltaic System," *Innov. in Power and Adv. Computing Techn.*, 2019. doi:10.1109/i-PACT44901.2019.8960079.

[61]   M. Green, E. Dunlop, J. Hohl-Ebinger, M. Yoshita, N. Kopidakis, and X. Hao, "Solar cell efficiency tables (version 57)," *Prog. Photovoltaics Res. Appl. John Wiley Sons, Ltd*, vol. 29, pp. 3–15, 2021, doi: https://doi.org/10.1002/pip.3371.

[62]   REN21 (2021), Renewables 2020 Global Status Report, Paris: REN21 Secretariat. ISBN: 978-3-948393-00-7.

[63] J. Svarc, "Solar Panel Construction," *Clean Energy Reviews*, 2020. [Online]. Available: https://www.cleanenergyreviews.info/blog/solar-panel-components-construction (accessed Aug. 19, 2021).

[64] D. L. King, J. K. Dudley, and W. E. Boyson, "PVSIM©: A Simulation Program for Photovoltaic Cells, Modules, and Arrays," in *25th IEEE Photovoltaic Specialists Conference Proceedings*, Washington DC, 13-17 May 1996, IEEE, 2002, pp. 1295–1297.

[65] *Standard tables for reference solar spectral irradiances: direct normal and hemispherical on 37 degree tilted surface*, ASTMG173-03, 2005.

[66] *Photovoltaic devices - Procedures for temperature and irradiance corrections to measured I-V characteristics*, IEC 60891:2009, 2010.

[67] O. Breitenstein, J. Bauer, K. Bothe, W. Kwapil, D. Lausch, U. Rau, J. Schmidt, M. Schneemann, M. Schubert, W. C. Martin, W. Jan Martin, W. Wilhelm, "Understanding junction breakdown in multicrystalline solar cells," *J. Appl. Phys.*, vol. 109, no. 7, 2011, doi: 10.1063/1.3562200.

[68] F. J. Vorster and E. E. Van Dyk, "Current-voltage characteristics of high-concentration, photovoltaic arrays," *Prog. Photovoltaics Res. Appl.*, vol. 13, no. 1, pp. 55–66, 2005. doi: 10.1002/pip.563.

[69] J. I. A. Tsanakas and P. Botsaris, "On the Detection of Hot Spots in Operating Photovoltaic Arrays through Thermal Image Analysis and a Simulation Model," *Mater. Eval.*, vol. 71, pp. 457–465, 2013.

[70] S. Bowden and C. Honsberg, PVCDROM | Bypass Diodes | PVEducation, [Online]. Available: https://www.pveducation.org/pvcdrom/modules-and-arrays/bypass-diodes, (Accessed 09 April 2022).

[71] R. G. Vieira, F. M. U. de Araújo, M. Dhimish and M. I. S. Guerra, "A Comprehensive Review on Bypass Diode Application on Photovoltaic Modules," *Ener.*, 13(10), 2472, 2020, doi: 10.3390/en13102472.

[72] B. B. Pannebakker, A. C. de Waal and W. G. J. H. M. van Sark, "Photovoltaics in the shade: one bypass diode per solar cell revisited," *Prog. in Phot.*, 25(10), 836-849, 2017, doi: 10.1002/pip.2898.

[73] Solaredge, Technical Note Bypass Diode Effects in Shaded Conditions, [Online]. Available: https://www.solaredge.com/sites/default/files/se_technical_bypass_diode _effect_in_shading.pdf (accessed 09 April 2022).

[74] W. G. Shin, S. Whan Ko, H. Jun Song, Y. Chul Ju, H. Mi Hwang and G. Hwan Kang, "Origin of Bypass Diode Fault in c-Si Photovoltaic Modules: Leakage Current under High Surrounding Temperature," *Ener.*, 11(9), 2416, 2018, doi: 10.3390/en11092416.

[75] J. W. Bishop, "Computer simulation of the effects of electrical mismatches in photovoltaic cell interconnection circuits," *Sol. Cells*, vol. 25(1), pp. 73–89, 2020, doi: 10.1016/0379-6787(88)90059-2.

[76] A. Woyte, J. Nijs and R. Belmans, "Partial shadowing of photovoltaic arrays with different system configurations: literature review and field test results," *Sol. Ener.*, vol. 74, pp. 217–233, 2003, doi: 10.1016/S0038-092X(03)00155-5.

[77] K. Sinapis, C. Tzikas, G. Litjens, M. Van den Donker, W. Folkerts and W. Van Sark, "A comprehensive study on partial shading response of c-Si modules and yield modeling of string inverter and module level power electronics," *Sol. Ener.*, vol. 135, pp. 731–741, 2016, doi: 10.1016/j.solener.2016.06.050.

[78] Solmetric Corporation, "Solmetric PV Analyzer I-V curve tracer with SolSensor TM user's guide," 2018. http://www.solmetric.net/get/Solmetric PV Analyzer Users Guide_1500_en.pdf (accessed 17 September 2021).

[79] Y. Zhu and W. Xiao, "A comprehensive review of topologies for photovoltaic I–V curve tracer," *Sol. Ener.*, vol. 196, pp. 346–357, 2020, doi: 10.1016/j.solener.2019.12.020.

[80] Solmetric Corporation, "Guide To Interpreting I-V Curve Measurements of PV Arrays," 2011. http://resources.solmetric.com/get/Guide to Interpreting I-V Curves.pdf (accessed 17 September 2021).

[81] S. Silvestre, A. Boronat, and A. Chouder, "Study of bypass diodes configuration on PV modules," *Appl. Energy*, vol. 86, no. 9, pp. 1632–1640, 2009, doi: 10.1016/j.apenergy.2009.01.020.

[82] P. Bauwens and J. Doutreloign, "Reducing partial shading power loss with an integrated Smart Bypass," *Sol. Ener.*, vol. 103, no. 5, pp. 134–144, 2014, doi: http://hdl.handle.net/1854/LU-4430511.

[83] E. E. van Dyk and E. L. Meyer, "Analysis of the effect of parasitic resistances on the performance of photovoltaic modules," *Renew. Energy*, vol. 29, no. 3, pp. 333–344, 2004, doi: 10.1016/S0960-1481(03)00250-7.

[84] W. Herrmann, B. Farnung, G. Friesen, M. Köntges, B. Kubicek, O. Kunz, H. Liu, I. Tsanakas and J. Vedde, (2021), Performance, Operation and Reliability of Photovoltaic Systems: Qualification of Photovoltaic (PV) Power Plants using Mobile Test Equipment, IEA-PVPS 2021, https://iea-pvps.org/wp-content/uploads/2021/04/IEA-PVPS-T13-24_2021_Qualification-of-PV-Power-Plants_report.pdf.

[85] T. Fuyuki, H. Kondo, T. Yamazaki, Y. Takahashi, and Y. Uraoka, "Photographic surveying of minority carrier diffusion length in polycrystalline silicon solar cells by electroluminescence," Appl. Phys. Lett., vol. 86, no. 26, p. 262108, 2005.

[86] T. Potthoff, K. Bothe, U. Eitner, D. Hinken, and M. Köntges, "Detection of the voltage distribution in photovoltaic modules by electroluminescence imaging," Prog. Photovoltaics Res. Appl., vol. 18, no. 2, pp. 100–106, 2010.

[87] T. Fuyuki and A. Kitiyanan, "Photographic diagnosis of crystalline silicon solar cells utilizing electroluminescence," Appl. Phys. A, vol. 96, no. 1, pp. 189–196, 2009.

[88] T. Fuyuki, H. Kondo, Y. Kaji, A. Ogane, and Y. Takahashi, "Analytic findings in the electroluminescence characterization of crystalline silicon solar cells," J. Appl. Phys., vol. 101, no. 2, p. 23711, 2007.

[89]   J. L. Crozier, E. E. van Dyk, and F. J. Vorster, "Evaluating the Relationship Between Electroluminescence (EL) Imaging and the Power Output of Photovoltaic Modules," in *3rd South. African Sol. Energy Conf. Proc.*, Kruger National Park, 11-13 May 2015, SASEC, 2015, pp. 24–28.

[90]   C. Buerhop, S. Wirsching, A. Bemm, T. Pickel, P. Hohmann, M. Nieß, C. Vodermayer, A. Huber, B. Glück, J. Mergheim, C. Camus, J. Hauch and C. J. Brabec, "Evolution of cell cracks in PV-modules under field and laboratory conditions," *Prog. Photovoltaics Res. Appl.*, pp. 1–12, 2017, doi: 10.1002/pip.2975.

[91]   M. Köntges, I. Kunze, S. Kajari-Schröder, X. Breitenmoser, and B. Bjørneklett, "Quantifying the risk of power loss in PV modules due to micro cracks," *in 25th Eur. Photovolt. Sol. Energy Conf. Exhib.*, Valencia, 6-10 September 2010, München: WIP-Renewable Energies, 2010, pp. 6–10.

[92]   E. Kaplani, "PV Cell and Module Degradation, Detection and Diagnostics," *Renew. Energy Serv. Mank.*, vol. II, pp. 393–402, 2016, doi: 10.1007/978-3-319-18215-5.

[93]   I. M. Kwembur, J. L. Crozier Mccleland, E. E. van Dyk, and F. J. Vorster, "Detection of potential induced degradation in mono and multi-crystalline silicon photovoltaic modules," *Phys. B Condens. Matter*, vol. 581, p. 411938, 2020.

[94]   A. Smets, K. Jäger, O. Isabella, R. Swaaij van, and M. Zeman, *Solar Energy - The Physics and Engineering of Photovoltaic Conversion Technologies and Systems*, 1st ed. Cambridge: CAMBRIDGE UIT, 2016.

[95]   M. Vollmer and K.-P. Möllmann, *Infrared Thermal Imaging*, 2nd ed., vol. 1708. WILEY-VCH, 2018.

[96]   S. Taib, M. S. Jadin and S. Kabir, Thermal Imaging for Enhancing Inspection Reliability: Detection and Characterization, Infrared Thermography, Dr. Raghu V Prakash (Ed.), InTech, 2012. ISBN: 978-953-51-0242-7.

[97]   G. J. Zissis and W. Wolfe, *The Infrared Handbook*, Revised ed. General Dynamics, 1978.

[98]   R. Usamentiaga, P. Venegas, J. Guerediaga, L. Vega, J. Molleda, and F. G. Bulnes, "Infrared Thermography for Temperature Measurement and Non-Destructive Testing," *Sens. (Switzerland)*, vol. 14, no. 7, pp. 12305–12348, 2014, doi: 10.3390/s140712305.

[99]   FLIR Systems, "A GUIDE TO INSPECTING SOLAR FIELDS WITH THERMAL IMAGING DRONES," [Online]. Available: https://thermalcapture.com/wp-content/uploads/2019/08/pv-system-inspection-thermal-drones-07-15-19.pdf. (Accessed 15 April 2022).

[100] FLIR Systems, "Thermal Imaging Guidebook for building and renewable energy applications," 2011. [Online]. Available: http://www.flirmedia.com/MMC/THG/Brochures/T820325/T820325_EN.pdf. (Accessed: 15 April 2022).

[101] C. Buerhop, H. Scheuerpflug, and R. Weißmann, "The Role of Infrared Emissivity of Glass on IR-imaging of PV-Plants," in *26th Eur. Photovolt. Sol. Energy Conf. Exhib. Proc.*, Hamburg, 5-9 September 2011, München: WIP, 2011, pp. 3413–3416.

[102] S. Gallardo-Saavedra, L. Hernandez-Callejo, and O. Duque-Perez, "Technological review of the instrumentation used in aerial thermographic inspection of photovoltaic plants," *Renew. and Sust. Energy Rev.*, 93, pp. 566–579, 2018. DOI: 10.1016/j.rser.2018.05.027.

[103] Z. Zou, Y. Hu, B. Gao, W. L. Woo, and X. Zhao, "Temperature recovery from degenerated infrared image based on the principle for temperature measurement using infrared sensor," *J. Appl. Phys.,* vol. 115, no. 4, p. 43522, 2014.

[104] "IEC TS 62446-3 Ed.1: Photovoltaic (PV) systems - Requirements for testing, documentation and maintenance - Part 3: Photovoltaic modules and plants - Outdoor infrared thermography." 2017.

[105] A. Pandian, K. Bansal, D. J. Thiruvadigal, and S. Sakthivel, "Fire Hazards and Overheating Caused by Shading Faults on Photo Voltaic Solar Panel," *Fire Technol.*, vol. 52, no. 2, pp. 349–364, 2016. doi: 10.1007/s10694-015-0509-7.

[106] Agilent Technologies, "Agilent 34970A/34972A Data Acquisition Switch Unit User's Guide," 2012, [Online]. Available: https://testworld.com/wp-content/uploads/user-guide-keysight-agilent-34970a-34972a-daq.pdf.

[107] FLIR Systems, "User's manual FLIR T6xx series," 2013. [Online]. Available: https://www.instrumart.com/assets/FLIR-T620-T640-Manual.pdf.

[108] Photovoltaik Engineering, Peak Power Measuring Device and I-V-Curve Tracer for PV Modules and Generators, Operation and User Manual. [Online] https://www.pv-engineering.de/fileadmin/user_upload/download/Operation_Manual/Manual_PVPM _X.pdf, (accessed 24 April 2022).

[109] FLIR, "ResearchIR 4 User's Guide," 2015. [Online] https://assets.tequipment.net/assets/1/26/FLIR_ResearchIR_User_Manual.pdf. (Accessed 24 April 2022).

[110] S. I. Ibrahim, A. Radhi, K. Abass and A. Mahdi, "Effect of Air Mass Environmental Parameter on Photovoltaic Performance," *Int. J. of Trend in Res. and Dev.*, vol. 6(4), pp. 150-154, 2019.

[111] A. H. Shnishil , S. S. Chid , M. J. Yaseen and T. J. Alwan, "Influence of Air Mass on the Performance of Many Types of PV Modulus in Baghdad," *Elsevier Energy Procedia,* vol. 6, pp. 153-159, 2011. doi: 10.1016/j.egypro.2011.05.018.

[112] C. Schill, S. Brachmann and M. Koehl, "Impact of soiling on IV-curves and efficiency of PV-modules," *Sol. Ener.*, vol. 112, 2015, pp. 259-262. doi.org/10.1016/j.solener.2014.12.003.

[113] F. P. Lang, H. Wang, S. J. Zhang, J. B. Liu, and H. Yan, "Review on Variable Emissivity Materials and Devices Based on Smart Chromism," *Int. J. Thermophys.*, vol. 39, no. 1, pp. 1–20, 2018, doi: 10.1007/s10765-017-2329-0.

[114] J. Bai, Y. Cao, Y. Hao, Z. Zhang, S. Liu and F. Cao, "Characteristic output of PV systems under partial shading or mismatch conditions," *Sol. Ener.*, vol. 112, 2015, pp. 41-54, doi.org/10.1016/j.solener.2014.09.048.

[115] K. Niazi, H. A. Khan, and F. Amir, "Hot-spot reduction and shade loss minimization in crystalline-silicon solar panels," *Jour. of Ren. and Sust. Ener.*, vol. 10, 033506, 2018, doi.org/10.1063/1.5020203.

[116] O. E. Ikejiofor, Y. E. Asuamah, H. O. Njoku and S. O. Enibe, "Detection of Hotspots and Performance Deteriotations in PV Modules under Partial Shading Conditions Using Infrared Thermography," *Eng. Proc.*, vol. 2(71), 2020, doi:10.3390/ecsa-7-08201.

[117] M. A. Al Mamun, Md Hasanuzzaman and J. Selvaraj, "Experimental investigation of the effect of partial shading on photovoltaic performance, *Renew. Power Gener.*, vol. 11(7), 2017, pp. 912-921.

[118] A. A. Aminou Moussavou, A. Raji and M. Adonis, "IMPACT STUDY OF PARTIAL SHADING PHENOMENON ON SOLAR PV MODULE PERFORMANCE," in *2018 International Conference on the Industrial and Commercial Use of Energy (ICUE)*, Cape Town, 13-15 August 2018, pp. 1-7.

[119] M. A. Islam, M. Hasanuzzaman and N. A. Rahim, "A comparative investigation on in-situ and laboratory standard test of the potential induced degradation of crystalline silicon photovoltaic modules," *Renew. Energy*, 127 (2018) 102-113, doi: 10.1016/j.renene.2018.04.051.

[120] FLUKE, "Emissivity values of common materials," 2007. [Online]. Available: https://www.bergeng.com/mm5/downloads/fluke/Emissivity-Values-of-Common-Materials-Chart.pdf. (Accessed 12 October 2021).

[121] M. Widyartono and R. Rahmadian, "Partial Shading Effect on I-V Characteristic and Maximum Power of a Photovoltaic Array," in 3rd International Conference on Vocational Education and Electrical Engineering (ICVEE), Surabaya, Indonesia, 3-4 October 2020.

[122] J. C. Teo, R. H. G. Tan, V. H. Mok, V. K. Ramachandaramurthy and C. Tan, Impact of Partial Shading on the P-V Characteristics and the Maximum Power of a Photovoltaic String, *Ener.*, vol. 11(7), 2018, 1860; doi:10.3390/en11071860

[123] Å. F. Skomedal, B. L. Aarseth, H. Haug, J. Selj and E. S. Marstein, "How much power is lost in a hot-spot? A case study quantifying the effect of thermal anomalies in two utility scale PV power plants," *Sol. Ener.*, vol. 211, p. 1255-1262, 2020, doi.org/10.1016/j.solener.2020.10.065.

[124] S. W. Ko, Y. C. Ju, H. M. Hwang, J. H. So, Y. S. Jung, H. J. Song, H. Song, S. H. Kim and G. H. Kang, "Electric and thermal characteristics of photovoltaic modules under partial shading and with a damaged bypass diode," *Ener.*, vol. 128, 2017, pp. 232-243.

[125] M. Premkumar and R. Sowmya, "An effective maximum power point tracker for partially shaded solar photovoltaic systems," *Ener. Rep.*, vol. 5, 2019, pp. 1445-1462 doi: 10.1016/j.egyr.2019.10.006.

[126] H. Islam, S. Mekhilef, N. B. Mohamed Shah, T. K. Soon, M. Seyedmahmousian, B. Horan and A. Stojcevski, "Performance Evaluation of Maximum Power Point Tracking Approaches and Photovoltaic Systems," *Ener.*, vol. 11, 2018, pp. 365, doi:10.3390/en11020365.

[127] J. L. Crozier, E. E. Van Dyk, and F. J. Vorster, "Identification and characterisation of performance limiting defects and cell mismatch in photovoltaic modules," *J. Energy South. Africa*, vol. 26, no. 3, pp. 19–26, 2015.

[128] C. Dunderdale, W. Brettenny, C. Clohessy and E. E. van Dyk, "Photovoltaic Defect Classification through Thermal Infrared Imaging using a Machine Learning Approach," *Prog. in Photovoltaics: Res. and App.*, 28(3), 177–188, 2020.

[129] M. Dhimish, "Defining the best-fit machine learning classifier to early diagnose photovoltaic solar cells hot-spots, *Case Stud. in Therm. Eng.*, vol. 25, 2021, doi.org/10.1016/j.csite.2021.100980.

[130] D. Roche, H. Outhred and R. J. Kaye, " Analysis and Control of Mismatch Power Loss in Photovoltaic Arrays, *Prog. in Phot.: Res. and Appl.*, vol. 3, 1995, 115-127.

[131] J. Kim, M. Rabelo, S. P. Padi, H. Yousuf, E. C. Cho and J. Yi, "A Review of the Degradation of Photovoltaic Modules for Life Expectancy," *Ener.*, 14, 4278, 2021. https://doi.org/10.3390/en14144278.

[132] M. Dhimish and A. M. Tyrrell, "Power loss and hotspot analysis for photovoltaic modules affected by potential induced degradation," *Mater. Degradation*, vol. 6(11), 2022. doi.org/10.1038/s41529-022-00221-9.

Appendix A

Research outputs associated with this work

A.1 Journal publications

1.1   M. Vumbugwa, J. L. Crozier McCleland, E. E. van Dyk, and F. J. Vorster, "Effects of Dynamic Operational Conditions on Thermal Infrared Imaging of Monocrystalline Silicon Photovoltaic Modules," *Journal of Solar Energy Enginering.*, vol. 143, no. 2, pp. 1–6, 2021, doi: 10.1115/1.4048609.

1.2   M. Vumbugwa, J. L. C. McCleland, E. E. van Dyk, F. J. Vorster, and T. J. Serameng, "Effects of current mismatch due to uneven soiling on the performance of multi-crystalline silicon module strings," *Journal of Energy in Southern Africa*, vol. 31, no. 1, pp. 62–72, 2020, doi: 10.17159/2413-3051/2020/v31i1a7571.

1.3   M. Vumbugwa, F. J. Vorster J. L. Crozier McCleland and E. E. van Dyk, "Effects of changing partial cell shading on the electrical and thermal characteristics of crystalline silicon photovoltaic module," Solar Energy, vol. 240, pp. 147–156, 2022, doi.org/10.1016/j.solener.2022.05.031.

A.2 Conference Proceedings

2.1   M. Vumbugwa, J. L. Crozier McCleland, E. E. van Dyk, and F. J. Vorster, "Thermal Infrared imaging of monocrystalline silicon PV modules under dynamic operational conditions", 7th South African Solar Energy Conference (SASEC), 2021.

2.2   M. Vumbugwa, J. L. Crozier McCleland, E. E. van Dyk, and F. J. Vorster, "Thermal Infrared imaging of polycrystalline silicon PV modules under changing soiling conditions", 37th European Photovoltaic Solar Energy Conference and Exhibition (EU PVSEC), 2020.

2.3   M. Vumbugwa, J. L. Crozier McCleland, E. E. van Dyk, and F. J. Vorster, "Effects of varying load on Thermal Infrared imaging of p-Si PV modules", 11th Renewable Energy Postgraduate Student Symposium (REPS), 2020.

2.4   M. Vumbugwa, J. L. Crozier McCleland, E. E. van Dyk, and F. J. Vorster, "Correlation of Thermal imaging and current-voltage characteristics of defective PV module strings", 6th South African Solar Energy Conference (SASEC), 2019.

A.3   Conference Presentations

3.1   M. Vumbugwa, J. L. Crozier McCleland, E. E. van Dyk, and F. J. Vorster, "Thermal Infrared imaging of monocrystalline silicon PV modules under dynamic operational conditions", 7th South African Solar Energy Conference (SASEC), 2021.

3.2   M. Vumbugwa, J. L. Crozier McCleland, E. E. van Dyk, and F. J. Vorster, "Effects of partial soiling on Thermal Infrared imaging of crystalline PV modules", 65th South African Institute of Physics Conference (SAIP), 2021.

3.3   M. Vumbugwa, J. L. Crozier McCleland, E. E. van Dyk, and F. J. Vorster, "Thermal Infrared imaging of polycrystalline silicon PV modules under changing soiling conditions", 37th European Photovoltaic Solar Energy Conference and Exhibition (EU PVSEC), 2020.

3.4   M. Vumbugwa, J. L. Crozier McCleland, E. E. van Dyk, and F. J. Vorster, "Effects of varying load on Thermal Infrared imaging of p-Si PV modules" 11th Renewable Energy Postgraduate Student Symposium (REPS), 2020

3.5   M. Vumbugwa, J. L. Crozier McCleland, E. E. van Dyk, and F. J. Vorster, "Correlation of Thermal imaging and current-voltage characteristics of defective PV module strings", 6th South African Solar Energy Conference (SASEC), 2019.

3.6   M. Vumbugwa, J. L. Crozier McCleland, E. E. van Dyk, and F. J. Vorster, "Correlation of Thermal imaging and I-V characteristics of PV module strings", 64th South African Institute of Physics Conference (SAIP), 2019.

3.7   M. Vumbugwa, J. L. Crozier McCleland, E. E. van Dyk, and F. J. Vorster, "Effects of current mismatch due to uneven soiling on performance of multi-crystalline silicon module strings", 64th South African Institute of Physics Conference (SAIP), 2019.

A.4   Other work

4.1   Babak Ravanbach, Benedikt Hanke, Meike Kühnel, Karsten von Maydell (DLR Institute of Networked Energy Systems, Germany) E. Ernest van Dyk, Monphias Vumbugwa (Nelson Mandela University, South Africa) Golden Makaka, Mahali Elizabeth Lesala, Ngwarai Shambira (University of Fort Hare, South Africa) Kittessa Roro (CSIR, South Africa) "Development of a Smart Monitoring and Evaluation Framework for Hybrid Renewable Mini-grids", 15th International Conference on Ecological Vehicles and Renewable Energies (EVER), 2020

A.5   Awards

5.1   Best PhD Poster presentation in the Applied Physics Division at 65th South African Institute of Physics Conference (SAIP) 2021.